A DOCTORAL DISSERTATION
PREPARED IN THE INSTITUTE OF PHYSICS
OF THE JAGIELLONIAN UNIVERSITY,
SUBMITTED TO THE FACULTY OF PHYSICS,
ASTRONOMY AND APPLIED COMPUTER SCIENCE
OF THE JAGIELLONIAN UNIVERSITY

JAGIELLONIAN UNIVERSITY
IN KRAKOW

Determination of the analysing power for the $\vec{p}p \to pp\eta$ reaction using WASA-at-COSY detector system

Iryna Schätti-Ozerianska

THESIS ADVISOR:
PROF. DR. HAB. PAWEL MOSKAL
CO-ADVISOR:
DR. ING. MARCIN ZIELIŃSKI
Cracow, 2015

Every story has a beginning...
Every story has its hero
On a journey from innocence to experience

Inspector Morse

Abstract

The η meson production process can be studied via measurements of the analyzing power, A_y, which may be understood as a measure of the relative deviation between the differential cross section with and without polarized beam. Spin-dependent observables such as cross sections and analyzing powers have been determined only for a small number of excess energies and with very high statistical uncertainty. Therefore, measurements of the reaction $\vec{p}p \to pp\eta$ was performed at the WASA-at-COSY detector in a fixed-target experiment with beam momenta of 2026 MeV/c and 2188 MeV/c. These correspond to excess energies of 15 MeV and 72 MeV, respectively. The η meson was identified by the techniques of missing mass and invariant mass. The invariant mass technique was mainly used to reduce background events, while the missing mass technique provided an accurate value of the number of the η mesons as a function of the emission angle.

The angular distribution of the analyzing power was compared with existing theoretical models. Predictions of all existing models strongly disagree with the experimental results determined in the framework of this thesis.

A comparison of the obtained A_y angular distribution with a series of associated Legendre polynomials revealed negligible contribution of the Sd partial wave at Q =15 MeV. However, at Q=72 MeV, a significant interference of the Ps and Pp partial waves was observed.

Contents

Chapter 1

Introduction

Despite that the η meson was discovered already in 1961 by A. Pevsner et al. [1], after almost 55 years of research, the production mechanism of the η meson via nucleon-nucleon interaction is still an open question. Nowadays information is available for the total and differential cross sections for the η meson production in nucleon-nucleon collisions from experiments [2–14] and theoretical calculations [15–23]. Those studies suggest that the production of the η meson occurs predominantly through the excitation of one of the interacting nucleons to the resonance $S_{11}(1535)$, to which the η meson couples strongly [24]. However, the excitation mechanism of this resonant current is not fully understood. There are plenty of possible scenarios where π, η, ω and ρ mesons may contribute to the resonance creation.

The COSY-11 measurements of the $pp \to pp\eta$ reaction performed with a polarized proton beam for momenta 2010 MeV/c and 2085 MeV/c can be interpreted that the excitation of the nucleon to the S_{11} resonance is predominantly due to the exchange of a π meson between the colliding nucleons [25]. The determined analyzing power is consistent with zero for both energies, which leads to the conclusion that the η meson is produced predominantly in the $s-$wave at both excess energies. However, the large statistical and systematic errors do not exclude a contribution from the higher partial waves.

So far the interaction between the η meson and nucleons is also not well established. Depending on the analysis method the nucleon-η scattering length varies between 0.2 fm and 1 fm [26]. The current status of experimental research is that the proton-η interaction is much larger than in the case of proton-π^0 and proton-η' interactions [9, 10, 27, 28] but it is estimated with large uncertainties.

The knowledge of the η and η' meson interaction with nucleons is important

for the search of mesic nuclei which is currently being carried out in many laboratories, e.g. COSY [29–32], ELSA [33], GSI [34], JINR [35], JPARC [36], LPI [37], and MAMI [38] with increasing theoretical support [39–52].

Previous studies of the η meson production in collisions of nucleons revealed that even in the close-to-threshold region higher partial waves and other baryon resonances may contribute to the production mechanism [52]. Moreover, the indication of the contribution of higher partial waves near threshold comes also from the comparison of the invariant mass distribution from the production of ppη and ppη' systems [52, 53]. Therefore, for an unambiguous understanding of the production process relative magnitudes from the partial wave contributions must be well established [52]. This may be at least to some extent achieved by measuring the angular dependence of the analyzing power A_y. The determination of the A_y for the $\vec{p}p \to pp\eta$ reaction is the main aim of this thesis.

The experiment was performed with a fixed proton target using the polarized proton beam of the COSY accelerator and the WASA-at-COSY detector. The particular experiment that is discussed in this thesis was conducted for beam momenta of 2026 MeV/c and 2188 MeV/c, which correspond to excess energies of 15 MeV and 72 MeV, respectively [54]. The analysis of the experiment was divided into two parts. In the first part, the polarization for the elastically scattered protons was defined. In the second part, the decay products of the η meson were identified in the central part of the WASA detector, while protons were determined based on signals registered in the forward part of the detector. The number of η mesons as a function of the η meson emission angle for the reaction $\vec{p}p \to pp\eta \to pp\gamma\gamma$ and $\vec{p}p \to pp\eta \to pp3\pi^0$ was extracted from the missing mass distribution.

This thesis is divided into nine chapters. The second chapter presents the theoretical motivation for the calculation of the analyzing power for the η meson production. In Chapter 3 the explanation of the experimental setup of the WASA-at-COSY facility and the main tools used in the analysis was given. Next in Chapter 4, the vertex position determination, based on the elastic scattering of the protons was described. Chapter 5 includes determination of the polarization based on proton elastic scattering events. The determination of the $\vec{p}p \to pp\eta$ reaction is presented in Chapter 6. The main result for the analyzing power is shown in Chapter 7. In Chapter 8 follows the discussion and interpretation of the determined analyzing power for the η meson. The last chapter is dedicated to a summary and an outlook.

Chapter 2

Motivation

2.1 Dynamics of the $pp \to pp\eta$ reaction

Most theoretical models try to explain the production of the η meson within the framework of the one-boson-exchange formalism [16–19, 21, 23]. Some of the possible mechanisms which may lead to η meson production are presented in Fig. 2.1.

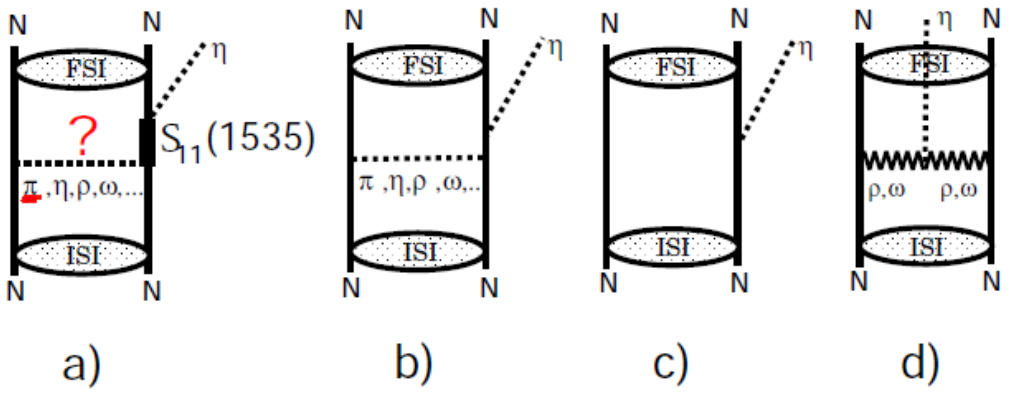

Figure 2.1: Possible scenarios of the η meson production in nucleon-nucleon collisions: (a) resonant current $S_{11}(1535)$, (b) nucleon currents, (c) direct production, (d) mesonic currents. The figure is adapted from [55].

One can see that the η meson is produced via exchange of one of the pseudoscalar or vector mesons, exciting the nucleon to the $S_{11}(1535)$ resonance (Fig. 2.1 (a)). When this resonance decays, it produces the nucleon-η pair. Other models [16] consider excitation of the $P_{11}(1440)$ and $D_{13}(1520)$ resonances that are excited via π, η, ρ, and ω mesons.

After the first measurements of the total cross section for the reaction $pp \to pp\eta$ in bubble chamber experiments [56–62], only recently appeared a precise data set on the total cross section of the η meson production in this reaction. The crucial observations were a large value of the absolute cross section (forty times larger than for the η' meson) and isotropic distributions of the angle of the η meson emission in the center-of-mass system of the reaction [63]. More constraints to the theoretical models [16–23] have been deduced from the dependence of the η meson production on the isospin of the colliding nucleons [64].

The experiments performed by the WASA/PROMICE and COSY-11 collaborations [64] revealed a strong isospin dependence. By comparing the first results on the analyzing power with the predictions based on different scenarios involving exchanges of various mesons with the so far determined unpolarised observables, the dominance of the π meson exchange in the production process is revealed [25]. This conclusion is in line with the predictions of Nakayama et al. [16].

To reach quantitative conclusions and to learn about contributions from various production processes and possible interference terms, more precise measurements of the spin observables are needed. In this thesis high statistic data on the $\vec{p}p \to pp\eta$ reaction with the polarized proton beam are presented. The result of the thesis can shed a light on the still unexplained origin of structures in the invariant mass distributions that have been observed independently by the TOF [65], COSY-11 [63], and WASA/CELSIUS [66] collaborations.

2.2 Interaction of the $pp\eta$ system

Another very interesting feature of the $\vec{p}p \to pp\eta$ reaction is the difficulties with reproducing pp invariant mass distributions. Calculations which include NN final state interaction (FSI) and $N\eta$ FSI do not match existing data. An example of a differential cross section distribution as a function of the pp invariant mass can be seen in Fig. 2.2. The shape of the distribution can be explained by considering higher partial waves Fig. 2.3. By taking into account a P-wave contribution, the pp invariant mass distribution can be reproduced [67]. To solve this discrepancy, the D_{13} resonance has been included in the calculations [68]. However, the data collected so far are insufficient for the unambiguous extraction of the S-wave or P-wave contributions.

For an unambiguous understanding of the production process relative magnitudes from the partial wave contributions must be well established. It maybe

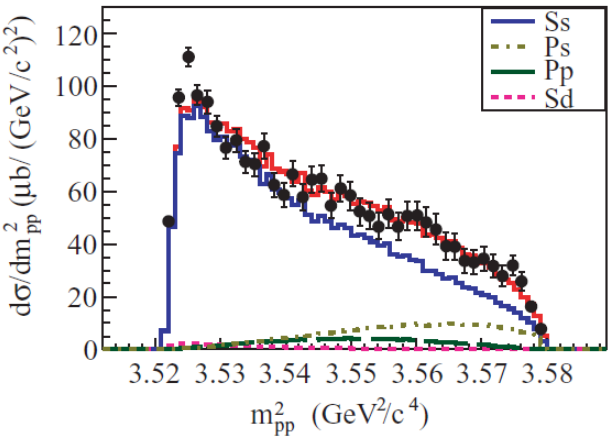

Figure 2.2: The $\vec{p}p \to pp\eta$ differential cross section in terms of the square of the pp invariant mass at $Q = 15.5$ MeV. Filled circles are COSY-11 experimental data. Contributions from individual partial waves are shown [66].

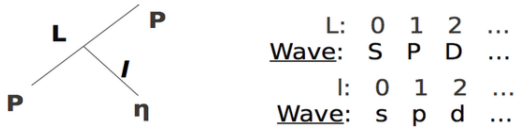

Figure 2.3: Relation of the partial waves in the $\vec{p}p \to pp\eta$ reaction. In the tree particle reaction with big letter, S, P ,D... denoting partial waves between two protons and small letters s, p, d... stands for the η-pp system.

partially achieved by measuring the analyzing power. This is because the polarization observables can probe the interference terms between various partial amplitudes, even if they are negligible in the spin-averaged distributions [54].

More importantly, in case of the $\vec{p}p \to pp\eta$ reaction, the interference terms between the transitions with odd and even values of the angular momentum of the final state baryons cancel in the cross sections [39, 69]. This is due to the invariance of all observables under the exchange of identical nucleons in the final state. The indistinguishability of the final state nucleons also means that there is no interference between s- and p-waves of the η meson in the differential cross sections [39]. However, s-p interference does not vanish in the proton analyzing power, and thus the precise measurements of A_y could provide the determination of the comparatively small p-wave contribution [39] that is unreachable from the spin-averaged observables.

${}^{2S^i+1}L^i_j \rightarrow$	${}^{2S^f+1}L^f_j, \ell$
${}^1S_0 \rightarrow$	${}^3P_0 s$
${}^3P_0 \rightarrow$	${}^1S_0 s$
${}^1D_2 \rightarrow$	${}^3P_2 s$
${}^3P_0 \rightarrow$	${}^3P_1 p$
${}^3P_1 \rightarrow$	${}^3P_0 p$
${}^3P_1 \rightarrow$	${}^3P_1 p$
${}^3P_2 \rightarrow$	${}^3P_1 p$

Table 2.1: Transitions for the $\vec{p}p \rightarrow pp\eta$ reaction with proton-proton angular momentum L = 0,1 and ℓ = 0,1 for the η meson production. The conventional spectroscopic notation is used where i and f state for initial and final state [70].

In the current work the contribution of the partial waves is investigated. We expect only low partial waves in close to the threshold region, such as Ss, Ps, Pp, Sd. Considering production of the protons with angular momentum L = 0 or 1 and for the η meson production ℓ = 0 and 1 then the $pp \rightarrow pp\eta$ reaction may proceed via possible transitions presented in the Tab. 2.1.

To distinguish contributions from the different partial waves we study analyzing power, since it becomes a non zero value if at least two different partial waves interfere. Analyzing power is proportional to:

$$A_y(\theta_\eta) \cdot \frac{d\sigma}{d\Omega}(\theta_\eta) \sim \Im\{A_{Ss} A^*_{Sd}\} \cdot sin\theta_\eta \cdot cos\theta_\eta + const. \Im\{A_{Ps} A^*_{Pp}\} \cdot sin\theta_\eta \quad (2.1)$$

where A_{Ss}, A_{Sd}, A_{Ps} and A_{Pp} denote amplitudes of Ss, Sd, Ps and Pp partial waves, respectively. Due to the Pauli principle even and odd partial waves (S, P, ..) of the protons in the final state cannot interfere with each other.

2.3 Definition of analyzing power A_y

Twelve parameters (the four-momenta of three particles) are necessary to describe the exit channel of a nuclear reaction with a given initial channel and a three-body final state. Only nine parameters are independent, while the other three parameters are fixed by the relativistic energy-momentum relation:

$$E_i^2 = m_i^2 + (\vec{p}_i)^2, i = 1, 2, 3; \quad (2.2)$$

where E_i, m_i, $\vec{p}_i$ denote the total energy, mass, and the momentum vector of the i-th particle, respectively. These variables depend on the initial state parameters on the basis of the four-momentum conservation (four additional equations). Therefore, in order to have a full description of the kinematics five independent variables suffice.

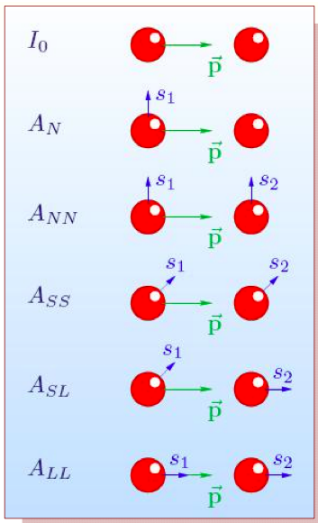

Figure 2.4: The coordinate system for the projections of A_y (Eq. 2.3). The picture is adapted from the presentation of Matthias Roeder.

In the following work, an orthogonal basis of the five-dimensional phase space is used. This space is spanned by the invariant masses of the proton-proton system m_{pp} and proton-η system $m_{p\eta}$, the polar θ_η and azimuthal φ_η angles of the η momentum in the center-of-mass (CM) frame, as well as the angle ψ that describes the rotation around the direction established by the momentum of the η meson [24]. This basis is denoted by $\xi = (m_{pp}, m_{p\eta}, \varphi_\eta, \theta_\eta, \psi)$ [55].

For a polarized target and beam, the general equation for A_y reads [71]:

$$\begin{aligned}\sigma(\xi, \tilde{P}, \tilde{Q}) = \sigma_0(\xi) \cdot (1 &+ A_N(\xi)[(P_y + Q_y)cos\varphi + Q_x sin\varphi] \\ &+ A_{SS}(\xi)[P_y Q_y sin^2\varphi + P_y Q_x cos\varphi sin\varphi] \\ &+ A_{NN}(\xi)[P_y Q_y cos^2\varphi - P_y Q_x cos\varphi sin\varphi] \\ &+ A_{SL}(\xi)[P_y Q_z sin\varphi],\end{aligned} \tag{2.3}$$

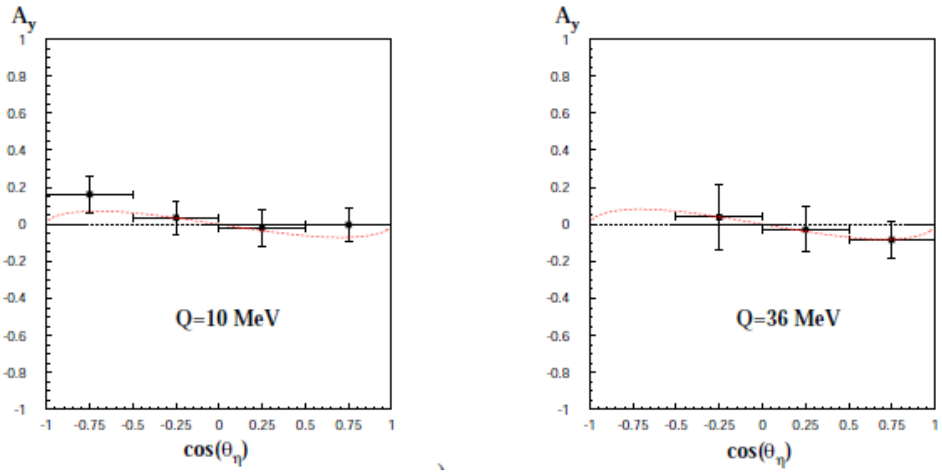

Figure 2.5: Analyzing powers determined by the COSY-11 collaboration for the reaction $pp \to pp\eta$ as functions of $\cos\theta_\eta$ for $Q = 10$ MeV (left panel) and $Q = 36$ MeV (right panel). The Figures are adapted from [25].

where N, S and L define the normal, side and longitudinal projections of A_y respectively [71], Q denotes the target polarization, P stands for the beam polarization. A full description of the polarized parameters for different cases is shown in Fig. 2.4. In case of the WASA-at-COSY experiment discussed in this thesis there was an unpolarized target and the beam polarization was aligned along y axis, so Eq. 2.3 simplifies to:

$$\sigma(\xi, \tilde{P}) = \sigma_0(\xi)(1 + A_N(\xi) \cdot P_y \cdot cos\varphi). \tag{2.4}$$

The key to all theoretical questions that were asked in the preceding chapters can be answered by calculating the analyzing powers $A_y(\xi)$. The vector analyzing power $A_y(\xi)$ may be understood as a measure of the relative deviation between the differential cross section with and without polarized beam (in the absence of target polarization), normalized to the beam polarization [55]:

$$A_y(\xi) = \frac{1}{P(\cos\varphi)} \cdot \frac{\sigma(\xi, P) - \sigma_0(\xi)}{\sigma_0(\xi)}. \tag{2.5}$$

2.4 Ay determined by DISTO and COSY-11 collaborations

Measurements of the analyzing power for the reaction $\vec{p}p \to pp\eta$ have been performed in the near threshold energy region at excess energies of Q = 10 MeV

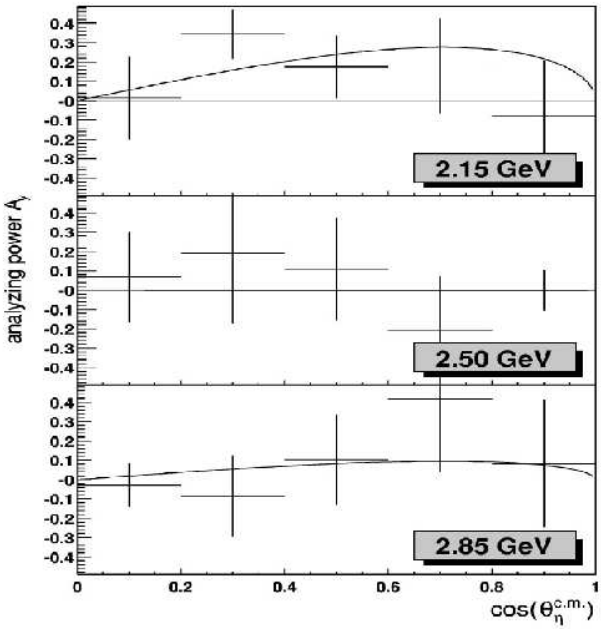

Figure 2.6: Analyzing powers determined by the DISTO collaboration for the reaction $\vec{p}p \to pp\eta$ as functions of $\cos\theta_\eta$ for $Q = 324$ MeV (upper panel), $Q = 412$ MeV (middle panel) and $Q = 554$ MeV (lower panel). The Figures are adapted from [72].

and 36 MeV at COSY by the COSY-11 collaboration (see Fig. 2.5), and at higher energies for $Q = 324$ MeV, $Q = 412$ MeV and $Q = 554$ MeV at SATURNE (see Fig. 2.6) by the DISTO collaboration. For all studied energies, the determined analyzing power is essentially consistent with zero. This implies that the η meson is produced predominantly in s-wave.

The results of previous experiments, as shown in figures 2.5 and 2.6, allowed for only a rough determination of the angular dependence with four and five bins with errors of A_y of about ± 0.1 and ± 0.2, respectively.

Chapter 3

Experimental equipment

3.1 COSY

The Cooler Synchrotron (COSY [73]) (see Fig. 3.1) is an ion accelerator operated at the Institute für Kernphysik (IKP) in Jülich, Germany. It provides polarized and unpolarized beams of protons and deuterons in the momentum range from 0.3 - 3.7 GeV/c. COSY is equipped with two different beam cooling systems: electron cooling for proton momenta up to 600 MeV/c, and stochastic cooling [74] for high momenta in the range from 1.5 - 3.4 MeV/c. These two cooling systems reduce the momentum spread of the beam and increase equilibrium emittance, allowing to store higher beam intensities. The total length of the COSY ring is 183.4 m, which contains in total 24 dipole magnets and two straight sections, each about 40 m in length.

3.2 WASA-at-COSY detector

The WASA-at-COSY detector [75] is one of the fixed-target hadron collision experiments at the COSY storage ring (Fig. 3.2). It is divided into two main parts: forward detector (FD) and central detector (CD). It has been designed to measure light mesons near the production threshold. The following sections provide an overview of each parts of the detector.

3.2.1 Pellet target system

The WASA-at-COSY experiment uses a unique design for the target, which is installed directly above the interaction region. A sketch of the device is shown in Fig. 3.3. First, hydrogen or deuterium gas is guided through a cold head

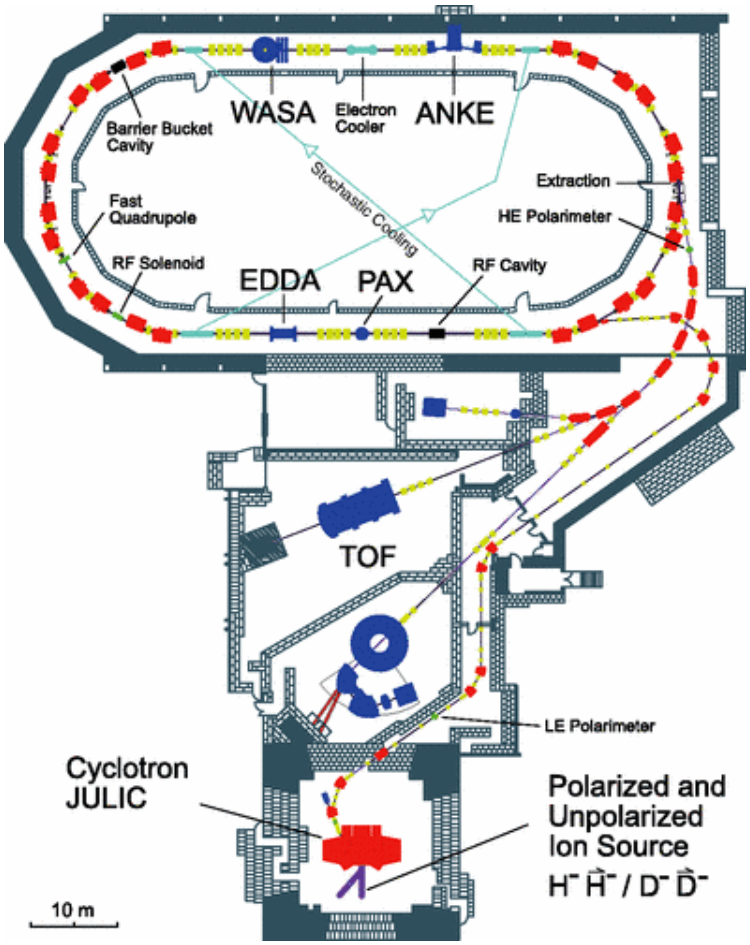

Figure 3.1: Cooler Synchrotron (COSY) storage ring.

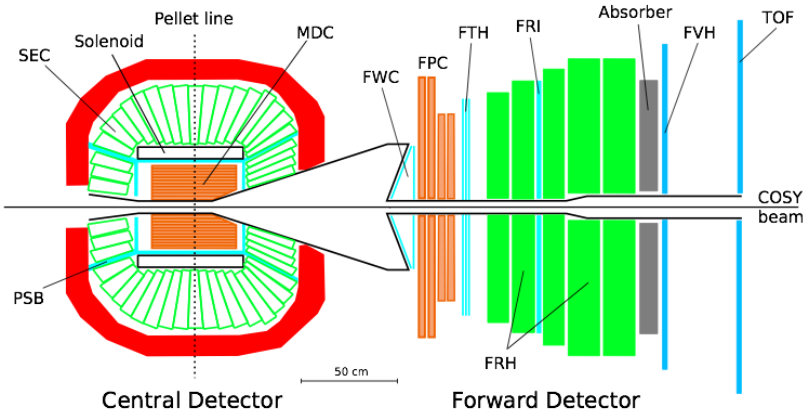

Figure 3.2: Cross sectional drawing of the WASA-at-COSY detector. The abriviations are explained in the text.

where the gas temperature is lowered sufficiently to liquefy it. Afterwards, the stream of liquid hydrogen is broken up by a vibrating nozzle into equidistant droplets with a diameter of 20-25 μm, called pellets which move down with the speed of about 80 m/s.

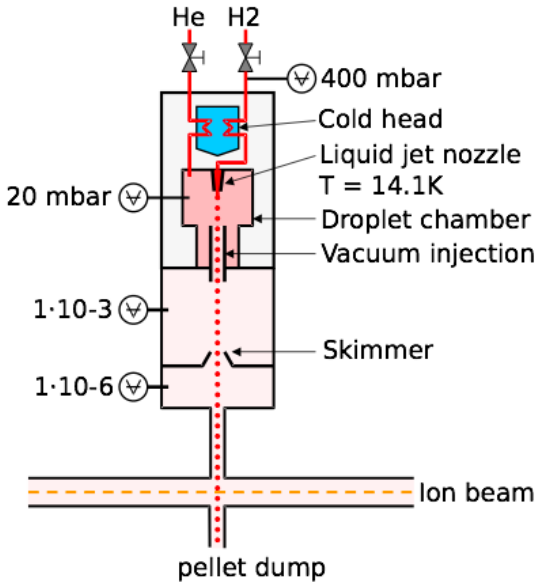

Figure 3.3: Schematic view of the pellet target system.

3.2.2 Forward Detector (FD)

The Forward Detector (FD) is placed downstream of the COSY beam from the interaction point where the scattered ions are predominantly found. This detector covers polar angles from 3° - 18° in laboratory system. Identification of the charged particles as protons, deuterons and ^3He nuclei is based on the measurement of the deposit energy in the several layers of scintillator material ($\Delta E - E$ method[1]).

3.2.3 The Forward Window Counter (FWC)

The first part encountered by particles hitting the FD is the Forward Window Counter (FWC) [76]. It is made of two layers, where each layer is again divided into 24 wedge-shaped elements. Each element contains plastic scintillator of

[1]Method based on the deposit energy of the chosen layer of the detector (FRH) plotted versus total energy deposited of the whole part of the detector (FRH).

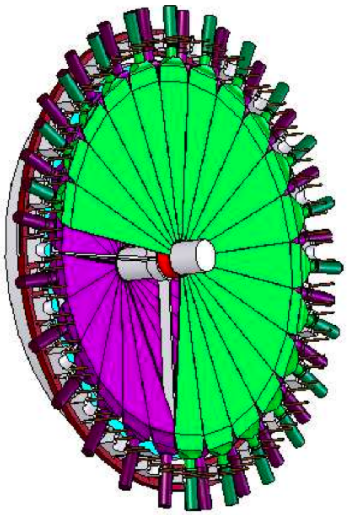

Figure 3.4: The Forward Window Counter.

3 mm thickness. The elements of the first layer are arranged in a conical shape, whereas the elements of the second layer are assembled in a vertical plane, as shown in Fig. 3.4. The elements of the second layer are rotated by half a module, with respect to the first layer.

The data from the FWC is used in the decisions taken by the trigger. Specifically, the coincidence of hits in different subdetectors at the same azimuthal angle is the basis of these decisions.

3.2.4 Forward Proportional Chamber (FPC)

The second part downstream is the forward proportional chamber (FPC). It provides accurate reconstruction of charged particle tracks and the determination of the scattering angle of the ions [77, 78]. It is constructed from 4 modules. Each module is made of four layers of 122 proportional drift tubes. The drift tubes have a diameter of 8 mm. The tubes are made from aluminized Mylar of 26 μm thickness. The stainless steel sense wire has a thickness of 20 μm. The drift tubes are filled with a gas mixture of argon and ethane (80% Ar / 20% C_2H_6).

The first two modules in the beam direction are rotated by $+45°$ and $-45°$ with respect to the x axis [79], respectively. The last two modules are aligned along the x and y axis, see Fig. 3.5.

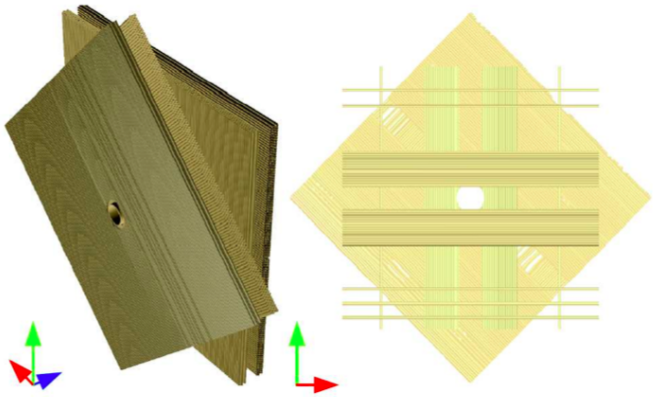

Figure 3.5: Left: the coordinate system in the corner of the picture shows the beam direction (z axis) as a blue arrow. Some tubes are removed to show the structure of the layers. Right: Forward Proportional Chamber (FPC) in two different projections.

3.2.5 The Forward Trigger Hodoscope (FTH)

The Forward Trigger Hodoscope (FTH) is placed as the third part of the forward detector. In coincidence with the FWC and it is used in the trigger logic, providing information about polar and azimuthal angles and hit multiplicity.

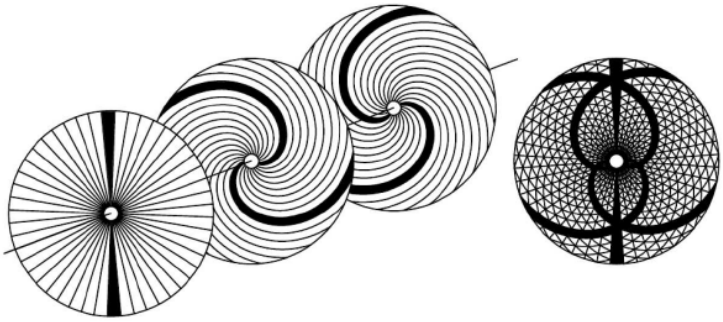

Figure 3.6: Left: FTH. Right: Pixels formed from the 3 layers of the FTH.

It consists of three layers of plastic scintillators, 48 radial sectors build up the first layer of the FTH, while the remaining two layers consist of 24 elements shaped like an Archimedean spiral. These two layers are oriented clockwise and counterclockwise, respectively. By overlapping all three layers, a 48x24x24 pixel map is constructed, as shown in Fig. 3.6.

3.2.6 Forward Range Hodoscope (FRH)

Five layers of thick wedge-shaped plastic scintillator elements build up the Forward Range Hodoscope (FRH [80]). Due to its good reconstruction performance for the energy resolution of stopped particles (3%), it plays an important role for the particle identification based on ΔE-E method.

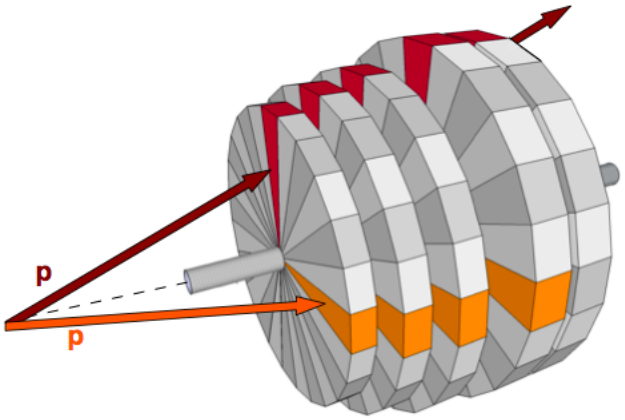

Figure 3.7: Layers of FRH. Figure adopted from [81].

In Tab. 3.1 the stopping powers are given for different particles that are reconstructed in the FRH. The thickness of the plastic scintillators varies between the layers. In the first three layers this is 11 cm, while in the last two layers the thickness is 15 cm.

Particle	E_{kin} to reach FRH1	E_{kin} to pass FRH5
π	25 MeV	200 MeV
p	60 MeV	370 MeV
d	80 MeV	485 MeV
$3He$	215 MeV	1325 MeV
$4He$	240 MeV	1475 MeV

Table 3.1: Minimum and maximum kinetic energy for various particles stopped in the FRH [82].

3.2.7 Forward Range Intermediate Hodoscope (FRI)

Between the second and third layer of the FRH the Forward Range Intermediate Hodoscope (FRI) is installed. It provides two-dimensional position

sensitivity to the FRH and helps separate background which comes from secondary interactions in the beam pipe and other material.

It is made of 32 plastic scintillator bars oriented along the beam and target directions as shown in Fig. 3.8.

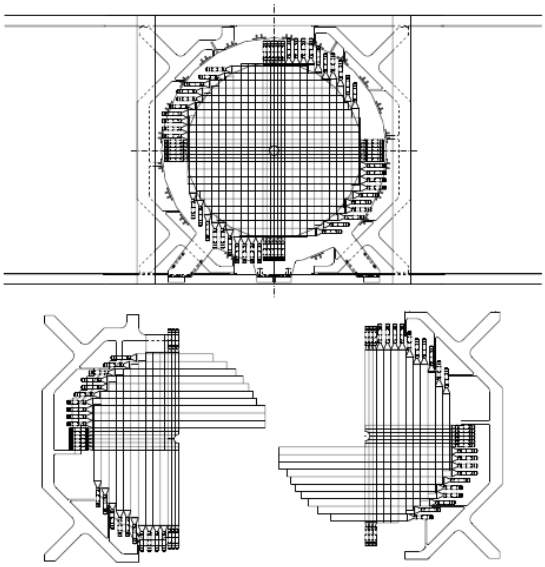

Figure 3.8: Forward Range Intermediate Hodoscope (FRI).

3.2.8 Forward Veto Hodoscope (FVH)

The sixth and last part of the FD is the Forward Veto Hodoscope (FVH [82]). Its purpose is to reconstruct highly energetic particles which pass through all previous layers of the FD, see Fig. 3.9 (left). The FVH consists of two layers of plastic scintilator bars read out by two photomultipliers at each end. First layers has 12 horizontally arranged bars while the second is arranged with the 21 vertical bars. Both layers of FVH can be also used for the Time-of-Flight measurement [83].

3.2.9 Central Detector (CD)

The central part of the WASA detector is used to detect products of η meson decays. The CD contains a Superconducting Solenoid (SCS), however, during the described experiment in order to increase the precision of the measurements with a polarized proton beam it was switched off. All parts of the CD cover a solid angle close to 4π rad and are described below.

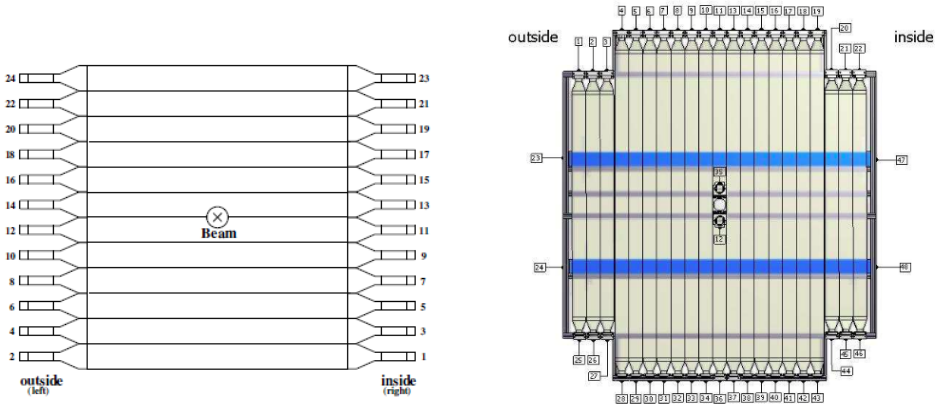

Figure 3.9: Left: First layer of Forward Veto Hodoscope (FVH1). Right: Second layer of Forward Veto Hodoscope (FVH2).

3.2.10 Mini Drift Chamber (MDC)

The innermost part of the CD, between the beam pipe and the solenoid, is taken up by the Mini Drift Chamber (MDC [82]). This drift chamber is able to measure the tracks of charged particles. It is made of 1738 drift tubes arranged in 17 layers. Each tube is made from 25 μm thin Mylar coated with aluminum on the inner side and a 20 μm sense wire of stainless steel. A gas mixture of argon and ethane (C_2H_6) fills the tubes in the proportions 80% argon and 20% ethane. The polar angles covered by the MDC ranges from 24° to 159°.

3.2.11 Plastic Scintillator Barrel (PS)

Surrounding the MDC and the solenoid, the Plastic Scintillator Barrel (PS [82]) is divided into three parts: a central cylindrical part (PSC) and a forward and backward cap (PSF and PSB) made of 8 mm thick plastic scintillators.

The cylindrical part (PSC) is split into rings of elements around the beam direction. Each ring contains 50 elements with different azimuthal angles. These elements overlap with each other by 6 mm. In the center of the PSC there is space for the pellet target cavity that cuts right through the whole detector.

The PSF and PSB complete the 4π geometry of the PS. Both PSF and PSB are made of 48 wedge-like elements aligned to the 48 ϕ sectors from the PSC.

3.2.12 Scintillating Electromagnetic Calorimeter (SEC)

The external part of the CD is taken up by the Scintillating Electromagnetic Calorimeter (SEC [84]). It covers 96% of the polar angle from 20° to 169° with an angular resolution of 5°. It can measure energies up to 800 MeV suited to the detection of photons, electrons and positrons. The energy threshold for photon detection is 2 MeV.

The SEC is constructed from 24 rings of 1012 CsI crystals doped with sodium. Each ring is divided into three parts according to the size of the crystal.

3.3 Production of the polarized proton beam

The COSY particle accelerator provides polarized protons and deuterons. The production of polarized protons is 20 times easier than polarized deuterons [85]. Consequently, proton polarization at COSY was achieved earlier, in 1996. By contrast, the production of polarized deuterons started later, in 2003. They are less sensitive to field errors.

In the present polarization experiments, running in 2010, the solenoid magnetic field of the detector was switched off. Otherwise, the spin of the polarized beam would start to rotate and in the end would vanish. This means that one needs more magnetic optics to control the polarization.

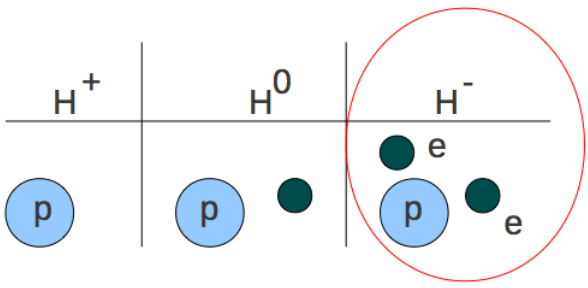

Figure 3.10: Chemical reaction in the polarized source.

The reaction that occurs in the source of the polarized proton beam is given by

$$H^0 + Cs^0 \rightarrow H^- + Cs^+ \tag{3.1}$$

The source chemical reaction are shown in Fig. 3.10. It provides polarized H^- ions in a direct charge-exchange process of colliding beams.

The following steps describe the production of a polarized proton beam, which can be seen in Fig. 3.11.

1. H^2 molecules are dissociated into atoms.
2. H atoms traverse the cooled nozzle and reach the sextupole magnets.
3. Atoms with electron spin state $m_J = -\frac{1}{2}$ are defocused and only atoms with $m_J = +\frac{1}{2}$ stay in the beam.
4. Used as a lens to focus hydrogen atoms to radio frequency transition units and lead to nuclear polarization.
5. H_0 collide with Cs (cesium) beam.
6. Nuclear polarization of the hydrogen by a strong longitudinal magnetic field.
7. Deflection of the polarized H^- anions by 90° in a magnetic field.
8. Select the required spin orientation of the H^- ions, and also separate the anions from the electrons and other background particles.
9. Acceleration of H^- anions in a cyclotron up to 45 MeV with further stripping of the electrons
10. Injection into the COSY main accelerator ring.

With this method of polarization a beam intensity of circa 10^{10} stored polarized protons with a degree of polarization over 65% was achieved during the experiments reported in this work. The degree of polarization was controlled by online measurements with the EDDA polarimeter [86].

3.3.1 Resonances at the COSY facility

The beam polarization can be perturbed by a horizontal magnetic field in the synchrotron and, if the frequency of the perturbation coincides with the spin precession frequency, the beam depolarizes. There are several orders of these depolarized resonances.

One of the first order resonance is the *imperfection (integer) resonance*:

$$v_s = \gamma G \tag{3.2}$$

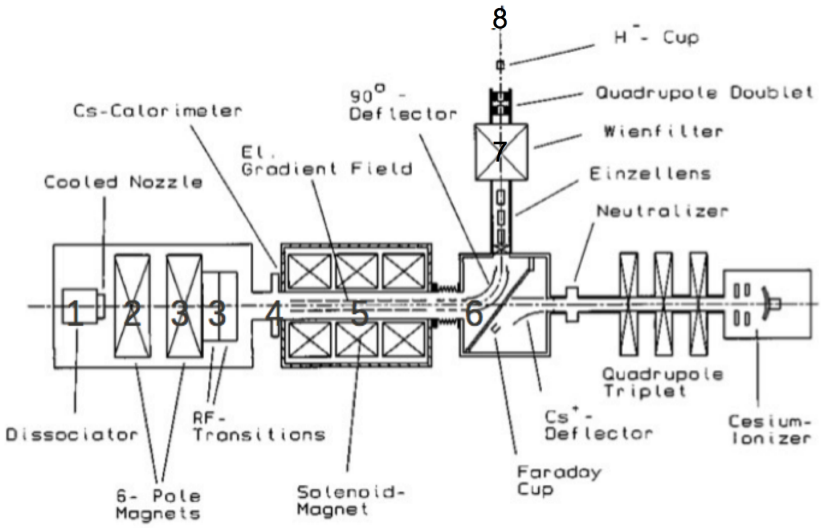

Figure 3.11: Schematic of the polarization source. The figure is adapted from [55].

where v_s [87, 88] is the spin tune[2], γ is the Lorentz factor of special relativity and $G = 1.7928$ is the gyromagnetic anomaly of the proton. If the spin tune is an integer, then every time the particle passes the field the spin vector is bent more and more away from the vertical axis until polarization is lost. This happens when magnets are slightly misaligned or if there are vertical orbit distortions. The particles then experience radial magnetic fields. Each time the particle passes the disturbing radial field the spin may point in a different direction with respect to the magnetic field if the spin tune is not an integer. The positions in momentum of the depolarizing resonances depend on the gyromagnetic anomaly G of the particle.

As can be seen in Fig. 3.12, for protons the first imperfection resonance kicks in at 464 MeV/c. If the spin tune is not an integer, these rotations are out of phase and the disturbing effect of the field averages out. As a result, imperfection resonances can be crossed without loss of polarization. At COSY there are 4 periods of imperfection resonances. The spin tunes 3.5 and 3.6 are used for the corrections.

The second kind of first-order spin resonances are called *intrinsic resonance*. It depends on the betatron amplitude and betatron tunes Q_x and Q_y,

[2]The number of spin revolutions per turn, called spin tune ν_s

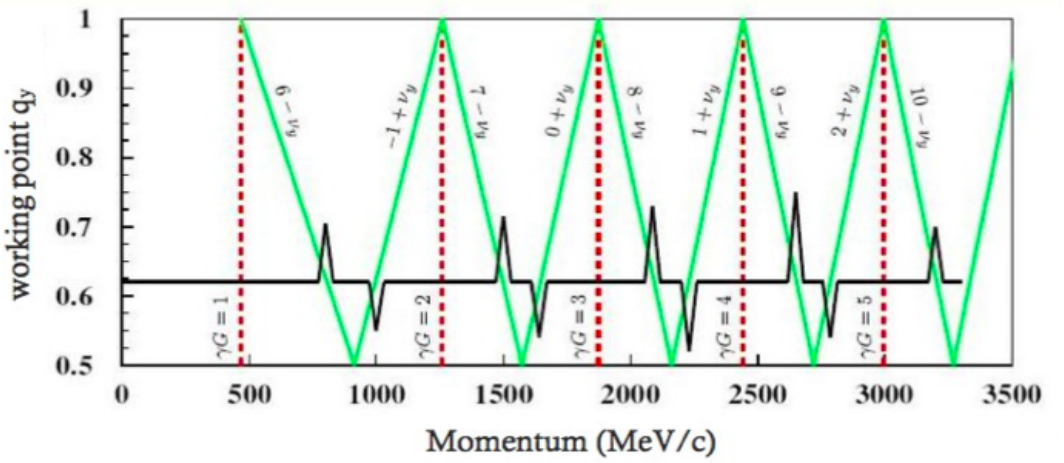

Figure 3.12: Depolarising resonances of the COSY accelerator ring as a function of the vertical fraction tune. Red line is an imperfection resonances. Green line is an intrinsic resonances. Black show a change in the working point during acceleration [89].

respectively. A horizontal spin resonance can only occur if $\gamma G \pm (Q_x/2)$ is integer.

Except for the case when there is coupling between the horizontal and vertical betatron oscillations, this resonance is not important at COSY with its vertically polarized beams. This is because the horizontal betatron oscillation is driven by vertical magnetic fields of the quadrupoles.

In addition to the horizontal betatron oscillation the particles also oscillate vertically with betatron tune Q_y [90]. This tune is induced by the radial magnetic fields of the vertically focusing quadrupoles. A resonance occurs if $\gamma G \pm (Q_y/2)$ is integer.

Among these resonances there are higher-order resonances as well. These resonances are excited by the synchrotron oscillation of the particles as induced by an rf-cavity for bunched beams. However, these cases play a minor role at COSY.

The position of the depolarizing resonances depend purely upon the revolution frequency of the machine and the kinematic factor

$$\gamma = \frac{E}{mc^2} \tag{3.3}$$

where E and m are the total energy and mass, respectively.

3.4 Data Acquisition System (DAQ)

The data acquisition system (DAQ) of the WASA-at-COSY detector is based on the third generation DAQ used by experiments at COSY (see Fig. 3.13), where FPGA-controlled read-out boards digitize and buffer the data. This system permits to conduct measurements at an average rate of accepted events of close to 10 kHz. The writing speed to the disk storage is approximately 80 MB/s. The trigger signal is generated after digitizing the data. When the trigger electronics generates a trigger signal, the synchronization system issues an event number with a time stamp, which is distributed to all Charge-to-Digital Converters (QDC) and Time-to-Digital Converter (TDC) boards. The data is then sent via high speed optical links to the computer farm and further to the event builder. Finally, the data is written to the disk storage.

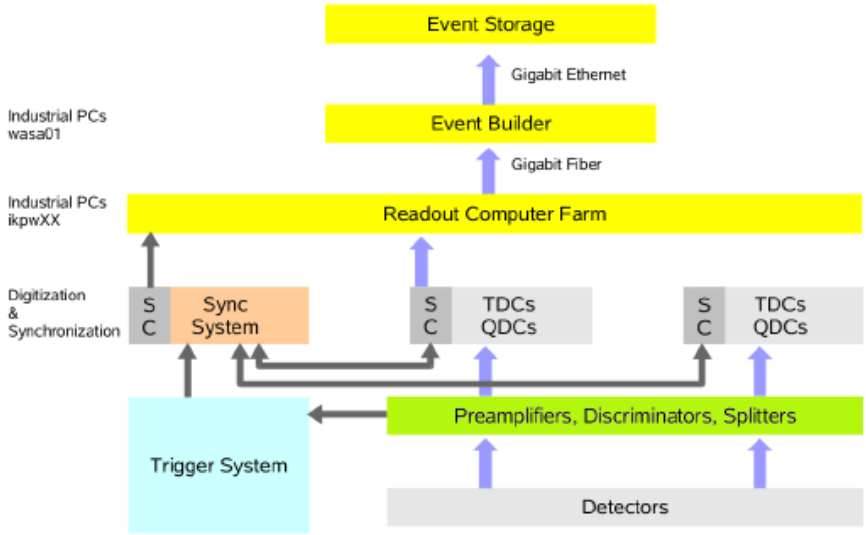

Figure 3.13: Data acquisition system (DAQ) for the WASA-at-COSY detector. The figure is adapted from [82]

3.5 Trigger system

The data selection performed by the trigger system allows to reduce the amount of background that is stored as an event. The decision whether or not to keep an event is based first on multiplicities, coincidences and track alignment from

the plastic scintillator detectors. Second, cluster multiplicities and energy sums provided by the SEC are taken into account. In the present experiment we are interested in two reactions: elastic scattering of protons and η meson production and decay into neutral channels.

For the $\vec{p}p \rightarrow pp$ reaction mainly two triggers were used. First, a single hit in the PSC was required with one or more hits in the PSF (PSB >= 1 V PSF >= 2). Second, one or more hits in the first forward range detector plane was required in coincidence with one or more hits in the PSC (FRD1 > 1 V CD >1). For the $\vec{p}p \rightarrow pp\eta$ reactions two or more sector matching tracks, i.e. hits in the FWC and FRH occurred in the same sector, were required in coincidence with 2 clusters (group of 16 crystals) in the SEC.

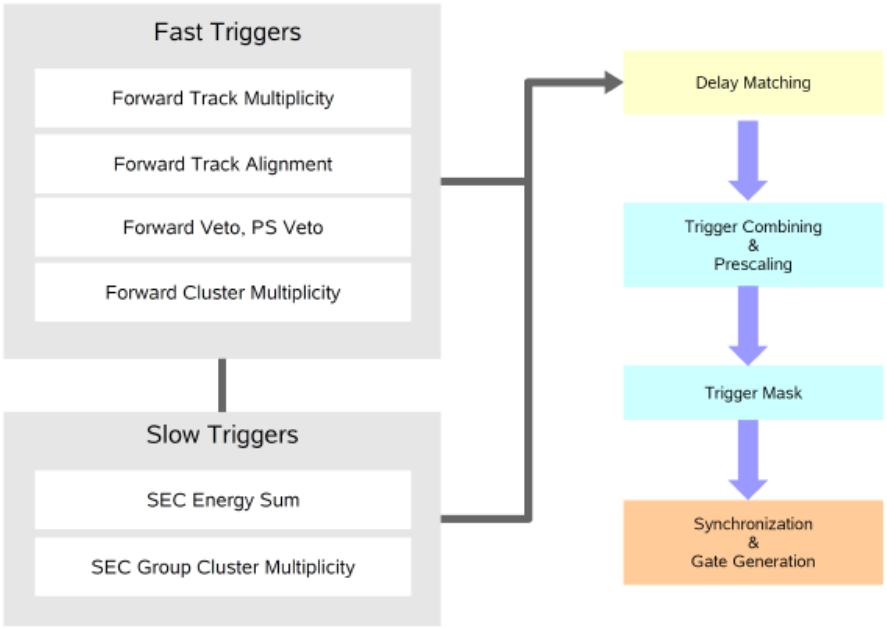

Figure 3.14: Trigger system for the WASA-at-COSY detector. The figure adopted from [82].

3.6 Analysis and simulation tools

The WASA-at-COSY software contains three independent tools.

Pluto++ is an event generator [91] which was created by the HADES group in order to study hadronic interaction from pion production. It is based on

the CERN analysis framework ROOT [92]. This package was used for the simulation of kinematic values of the final state particles.

The *WMC* package is responsible for the simulation of detector response and detector components. It is written in FORTRAN and based on the GEANT3 [93] libraries developed by CERN. Using material constants of the detector, geometry parameters, magnetic fields etc. It simulates events defined by input files. These input files provide information on the 4-vectors of the initial state particles.

The *RootSorter* [94] package provides a complete event reconstruction of the analysis. The simulation of the background and signal events is based on Monte Carlo, MC, methods.

Chapter 4

Determination of the vertex position

One of the main aims of the analysis was the determination of the polarization, based on the elastic scattering of protons. The most probable source of the systematic uncertainty in the determination of the polarization might be the error in the asymmetry of the number of events detected in the individual θ_{CM} ranges. This uncertainty may originate from a misalignment of the interaction point, which depends on the positions of the beam and the target.

The reconstruction of tracks of particles registered in the Mini Drift Chamber is free of any assumption of the position of the reaction vertex. In this respect, angular information obtained from the tracks of particles going through the Mini Drift Chamber is unbiased [95]. In turn, reconstruction of tracks of particles in the forward direction is based on the assumption that the interaction point coordinates are $(x_v, y_v, z_v) = (0,0,0)$ [95]. Therefore, information gained from the track of particles reconstructed in the MDC and FD may allow the reconstruction of the overlap between the beam and the target. In order to determine the interaction region we use two independent methods which are described below.

4.1 Extraction of the average vertex positions based on the coplanarity method

The first method which was applied for the vertex position determination is based on coplanarity. The coplanarity is defined as:

$$C = \frac{(\vec{p}_1 \times \vec{p}_2) \cdot \vec{p}_{beam}}{|\vec{p}_1 \times \vec{p}_2| \cdot |\vec{p}_{beam}|}, \tag{4.1}$$

where $\vec{p}_1$ and $\vec{p}_2$ correspond to the momentum vectors of scattered protons, and $\vec{p}_{beam}$ is the beam momentum vector.

A schematic view of how the coplanarity is constructed is shown in Fig. 4.1.

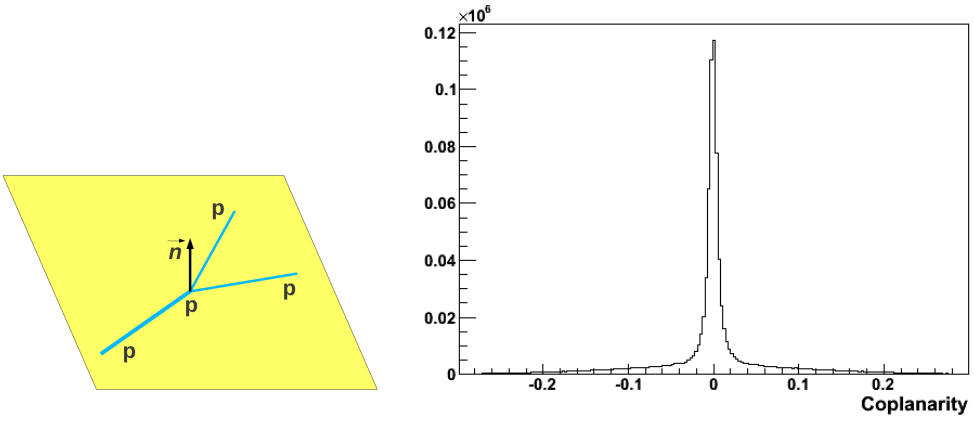

Figure 4.1: Coplanarity. Left: Visualization for the coplanarity plane. Right: example of the distribution of the coplanarity for one experimental run.

In order to find the interaction region, coplanarity distributions as a function of the φ angle was simulated with different vertex positions and compared with the experimental distributions using the χ^2 minimization [52]. The coplanarity dependence on the protons azimuthal angle shows sinusoidal behavior for a misallocated vertex or beam.However, the beam is assumed to be aligned right (further studies are shown in Chapter 5.3). Therefore, the target is misallocated. This is shown on the right side of Fig. 4.2. Simulated data shows that assuming the vertex position at (0,0,0), gives a flat distribution of the coplanarity $C(\varphi)$ (Fig. 4.2 left). However, moving the vertex position to the point $(x_v, y_v, z_v) = (0.5,0,0)$ cm results in a sinusoidal shape of $C(\varphi)$(Fig. 4.2 right). Experimental data are presented in the lower panel of this picture.

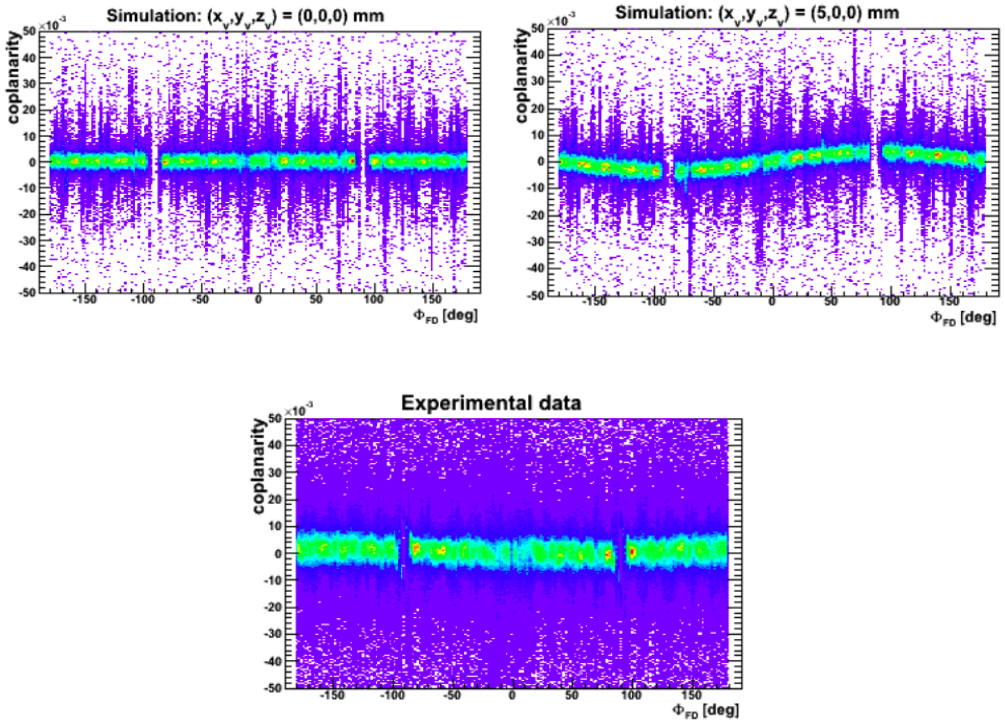

Figure 4.2: (Upper Panel) Example of simulated coplanarity distribution used to determine the vertex position: (left) with assumption of the vertex position at (0,0,0) mm, (right) with assumption of the vertex position at (5,0,0) mm. (Bottom Panel) An example of the experimental coplanarity distribution obtained for one run of data taken with the beam momentum 2026 MeV/c.

For each simulated $C(\varphi)$ spectrum a χ^2 value is calculated according to:

$$\chi^2 = \sum_i \frac{(M_i^{MC} - M_i^{exp})^2}{(\sigma_i^{exp})^2}, \tag{4.2}$$

where i indicates the chosen φ range, σ_i^{exp} is the uncertainty of M_i^{exp} and the M_i^{MC} and M_i^{exp} are the mean values of the coplanarities in a given φ range and σ_i^{exp} is the uncertainty of M_i^{exp} [52].

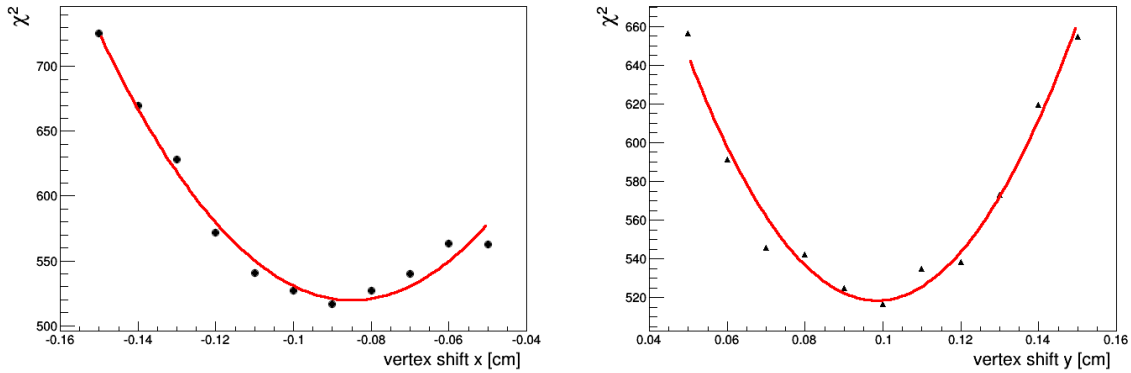

Figure 4.3: An exemplary χ^2 distribution for the vertex position determination: (left) for the x coordinate, (right) for the y coordinate.

The χ^2 value of the interaction point was determined for each run separately. Fig. 4.3 shows the results for a single experimental run. The dependence of $\chi^2(x)$ and $\chi^2(y)$ were fitted with a second degree polynomial and the minimum χ^2 was determined based on the result of the fit. The results for the vertex position calculated with this method for all data are presented in Fig. 4.4. Analysis were performed for both spin modes (spin up/down) and also for not polarized data. The results of the average value of the vertex coordinates can bee seen in Tab. 4.1.

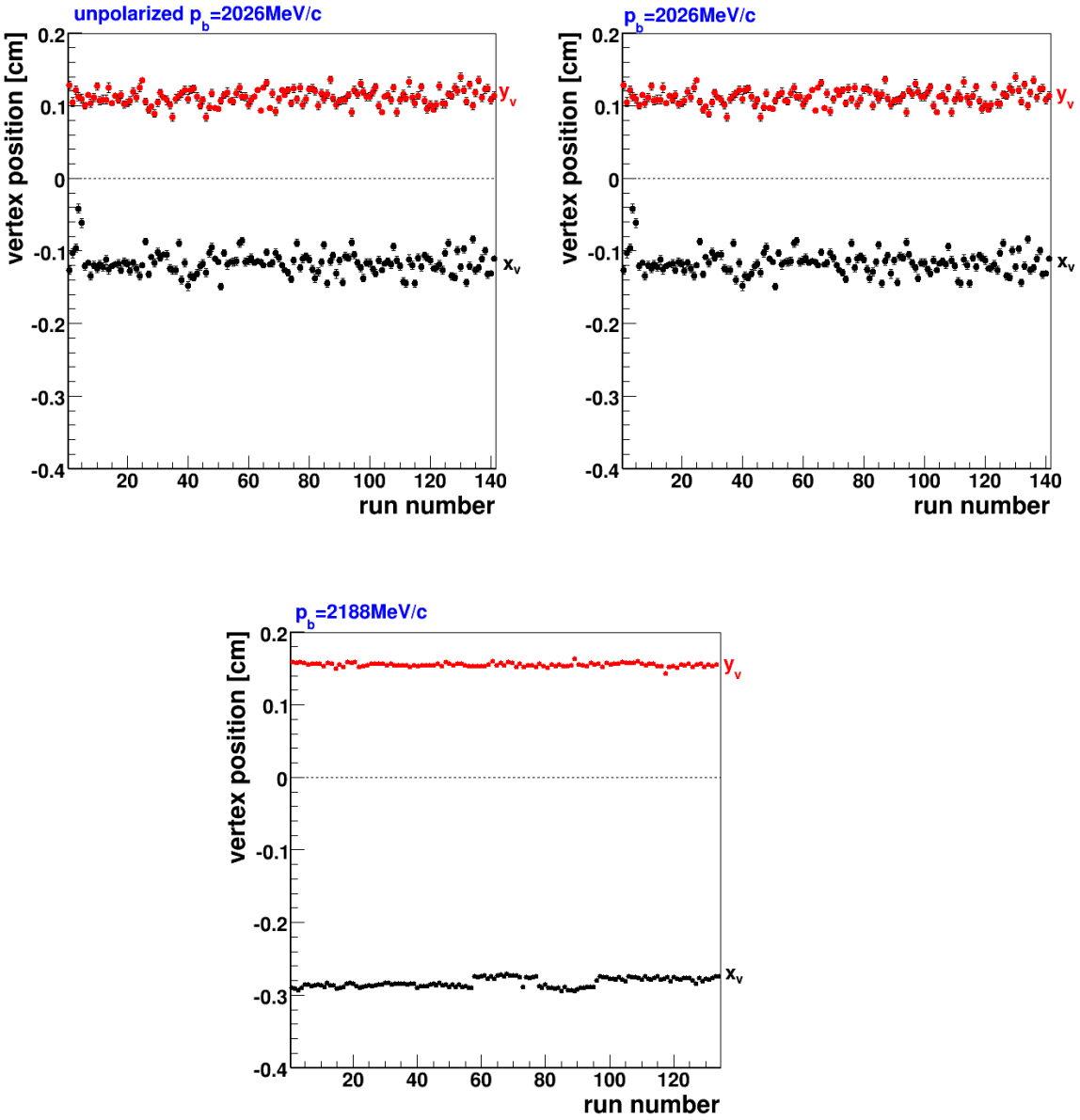

Figure 4.4: Distribution of the x (black points) and y (red points) coordinate of the vertex as a function of the run number. Values for the average (x_v,y_v) can be seen in Tab. 4.1.

4.2 Extraction of the vertex position using the distance method

In order to cross check the obtained results for the vertex position from the coplanarity method we have used a distance method described in [95]. In this

method we use the trajectories of the elastically scattered protons, which are projected into the xy plane (as shown in Fig. 4.5).

One proton p_2 is registered in the Mini Drift Chamber. It is reconstructed azimuthal angle ϕ_2 is therefore obtained independently of the position of the reaction vertex, always reflecting the 'true' value of the emission angle [95]. The other proton p_1 is scattered in the forward direction and intersects the first plane of the Forward Trigger Hodoscope (FTH) at a radius of:

$$R_1 = Z_{FTH} \tan(\theta_{p_1}) \tag{4.3}$$

where Z_{FTH} is the distance from the vertex to the Forward Trigger Hodoscope. The reconstruction of the path of the p_1 proton is based on the assumption that the interaction point coordinates are (x_v, y_v, z_v) = (0,0,0). Therefore, the reconstructed azimuthal angle ϕ_1 differs from the real one, ϕ_1'. This disagreement causes a deviation from the coplanarity of ϕ_2' - ϕ_1 [95]. The actual position of the vertex is described in the (x, y) plane by the new variables (d, ϕ_d), where d is the distance between the point (0, 0) and the intersection point of the dashed line and the solid line in Fig. 4.5. The dashed line includes the point (0,0) and is perpendicular to the projection of the proton trajectories. ϕ_d is the azimuthal angle between the dashed line and the x-axis. The variables d and ϕ_d are connected to the coordinates x_v and y_v of the reaction vertex by:

$$d(\phi_d) = x_v \cos(\phi_d) + y_v \sin(\phi_d). \tag{4.4}$$

Thus, x_v and y_v can be extracted by fitting the function above to the $d(\phi_d)$ distribution, as shown in the right-hand side of Fig. 4.5 for two vertex locations, at (x_v, y_v, z_v) = (0,0,0) mm (left plot) and at (x_v, y_v, z_v) = (5,0,0) mm (right plot) [95].

Both methods give results for the x_v and y_v coordinates that differ on average only by about 0.4 mm.

To determine the z coordinate of the vertex we use the angular dependencies between the two protons (see Fig. 4.6). The reaction vertex is placed on the z-axis at $z_v > 0$. The trajectory of proton p_2, reconstructed in the planes of the Mini Drift Chamber, is traced back to the actual reaction vertex, whereas the track of the forward going proton, p_1, is assumed to originate from the central point (0,0,0) [95]. Therefore, the scattering angle θ_1 of the forward going proton deviates from the real value θ_1'. The relation between the true and reconstructed values of the scattering angle of the forward going proton

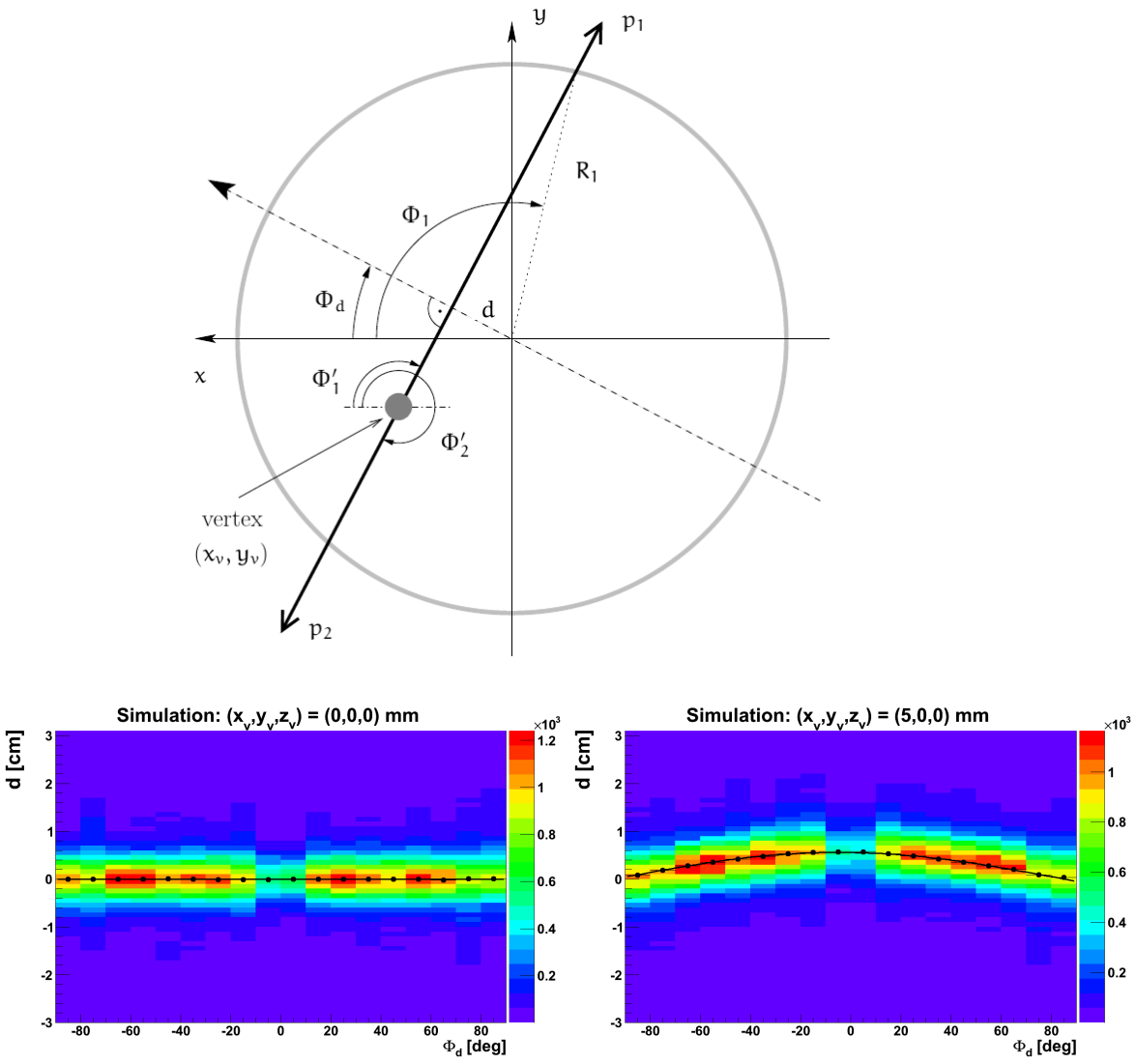

Figure 4.5: Upper panel: illustration the concept of the extraction of the x_v and y_v coordinates of the reaction vertex. Adopted from [96]. Lower panel: simulated distributions of $d(\phi_d)$ for the vertex position (x_v, y_v, z_v) = (0, 0, 0) mm (left plot) and (x_v, y_v, z_v) = (5,0,0) mm (right plot). The points show the positions of the mean of the distributions for the given ranges of ϕ_d. The line shows the result of fitting Eq. 4.4 to these points.

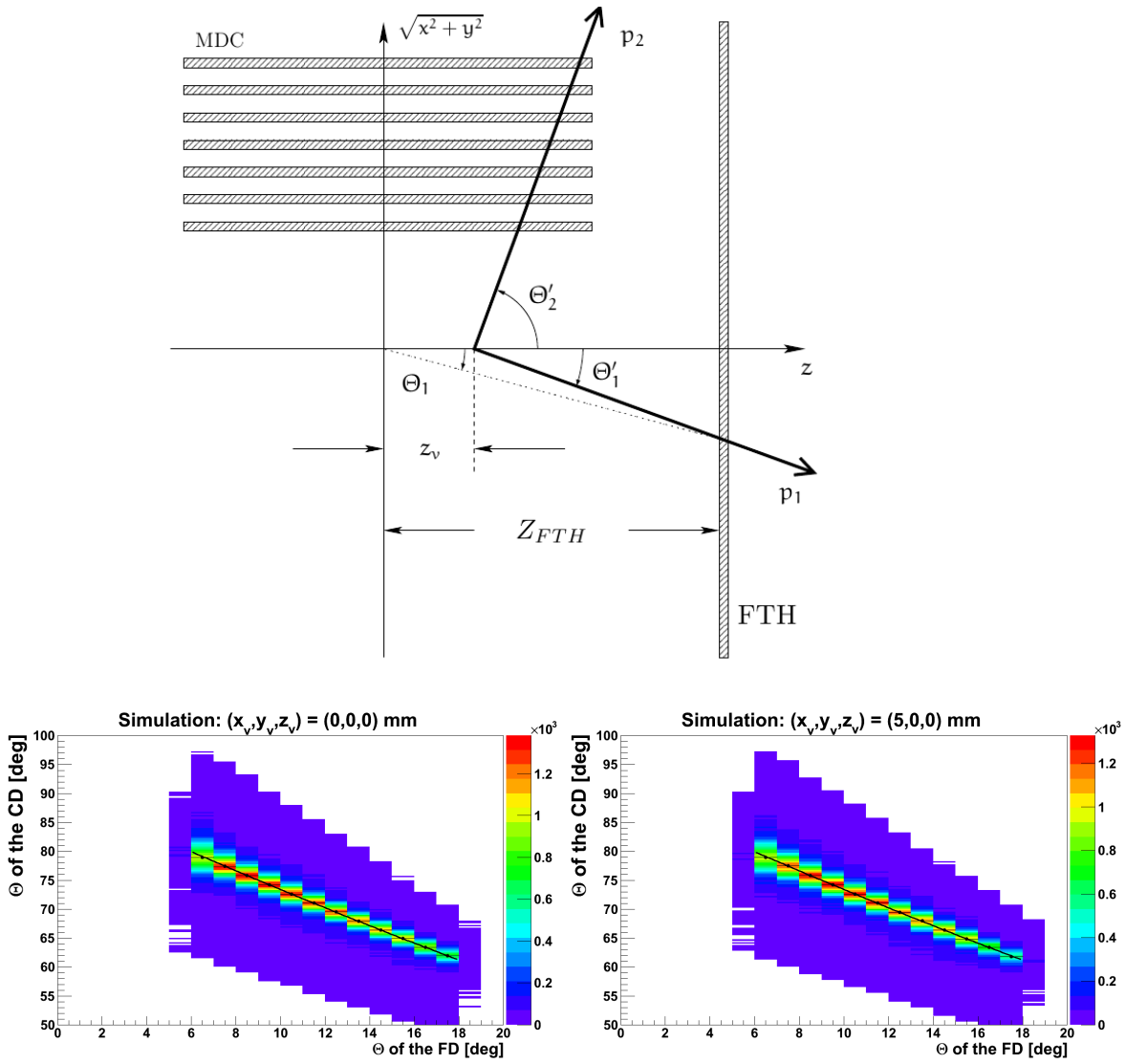

Figure 4.6: Upper panel: illustration the concept of the extraction of the z_v coordinate of the reaction vertex. Adopted from [96]. Lower panel: simulated distributions of θ_2'(θ_1) made for the vertex positions $(x_v, y_v, z_v) = (0, 0, 0)$ mm (left plot) and $(x_v, y_v, z_v) = (5, 0, 0)$ mm (right plot). The points show the positions of the mean of the θ_{CD} distribution for the given ranges of θ_{FD}. The line denotes the result of fitting Eq. 4.7 to these points.

can be written as:

$$\frac{1}{\tan(\theta_1')} = \frac{1}{\tan(\theta_1)}(1 - \frac{z_v}{Z_{FTH}}). \tag{4.5}$$

Additionally, one can utilize the kinematic relation between scattering angles:

$$\tan(\theta_1')\tan(\theta_2') = \frac{2m_p}{2m_p + T}, \tag{4.6}$$

where m_p stands for the proton mass and T is the kinetic energy of the proton beam. Solving equations 4.5 and 4.6 for $\tan(\theta_2')$ results in [95]:

$$\tan(\theta_2') = \frac{1 - \frac{z_v}{Z_{FTH}}}{\tan(\theta_1)(1 + \frac{T}{2m_p})}. \tag{4.7}$$

Therefore, the z_v coordinate can be extracted by fitting the distribution of $\theta_2'(\theta_1)$. This is shown in the right-hand side of Fig. 4.6 for two cases of vertex location, at (x_v, y_v, z_v) = (0, 0, 0) mm (left plot) and at (x_v, y_v, z_v) = (5, 0, 0) mm (right plot). A set of simulations have been run for different locations of the vertex, where only one of the vertex coordinates was changed at once, leaving the others at zero [95].

The accuracy of the method used to extract the vertex position [96] is shown in Fig. 4.7 for the x coordinate, Fig. 4.8 for the y coordinate and Fig. 4.9 for the z coordinate. In each of these figures, the reconstructed value of the coordinate (fit) is separately plotted against the offset in x, y and z (set). Therefore, points in pictures placed diagonally should be arranged along the line $fit(set) = set$, while other distributions should show $fit(set) = 0$. The fits of the polynomial of the first order to the points in pictures placed diagonally (solid, red lines) show that in all cases, the extracted values deviate slightly from the set values (up to 14% in the case of $y_{fit}(y_{set})$). This needs to be taken into account when extracting the vertex position in experimental data. Notice that if the change in a given coordinate is not bigger than about 0.5 cm, the extraction of the other coordinates is accurate.

The result of the distance method for determining the vertex position is presented in Fig. 4.10. After averaging (over runs), the two methods are compared in Tab. 4.1. The result established by the two methods differs by less than $\pm$ 0.5 mm.

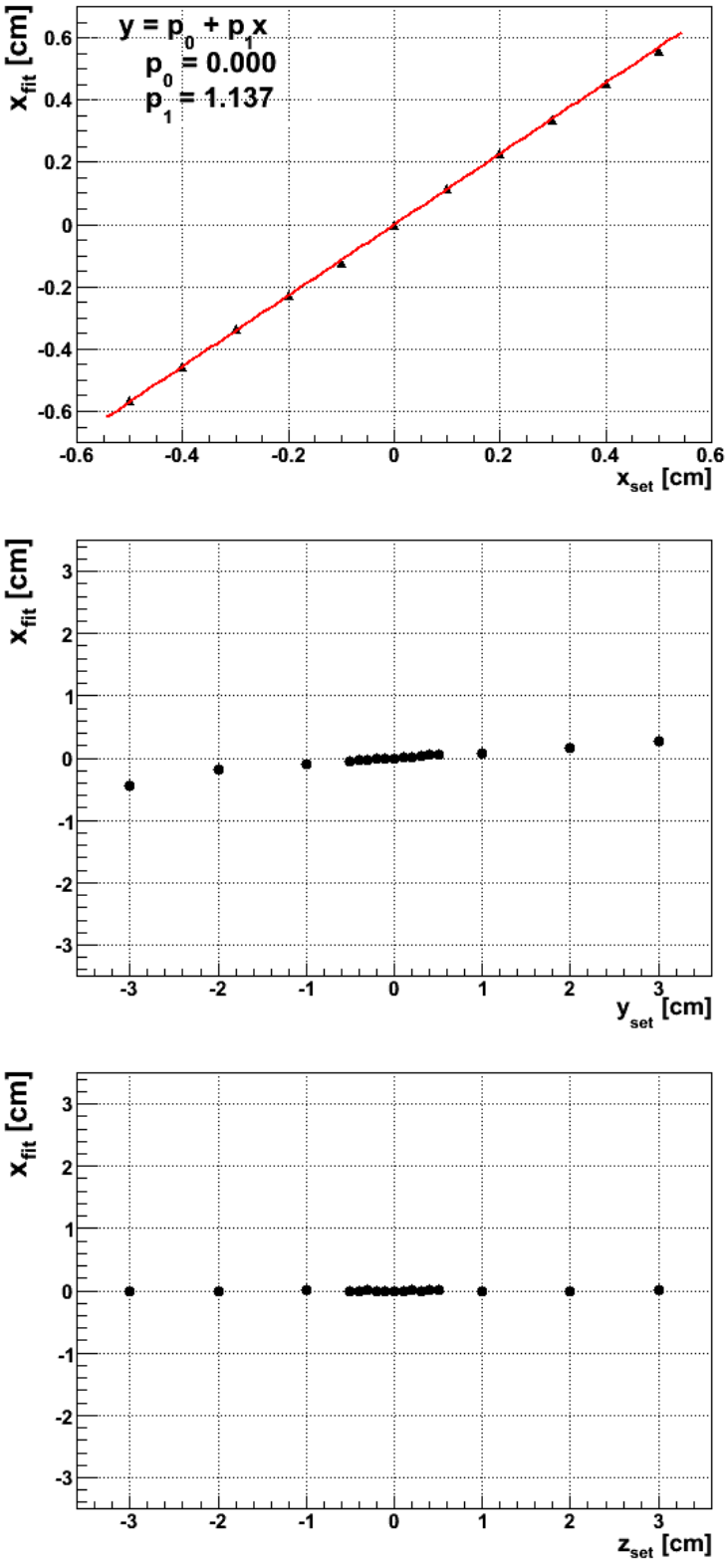

Figure 4.7: Results of reconstruction tests for the x coordinates of the reaction vertex for offsets in x, y and z.

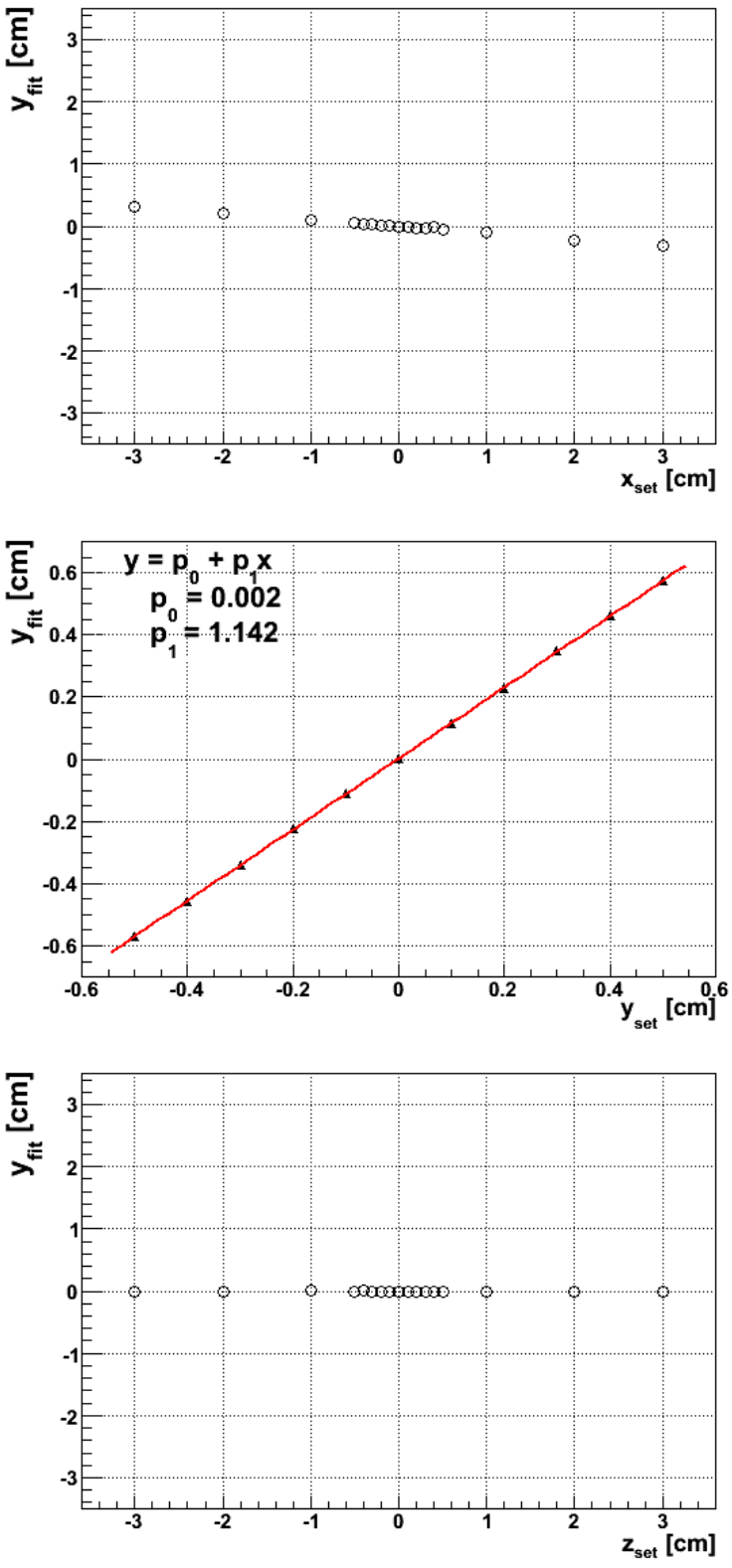

Figure 4.8: Results of reconstruction tests for the y coordinates of the reaction vertex for offsets in x, y and z.

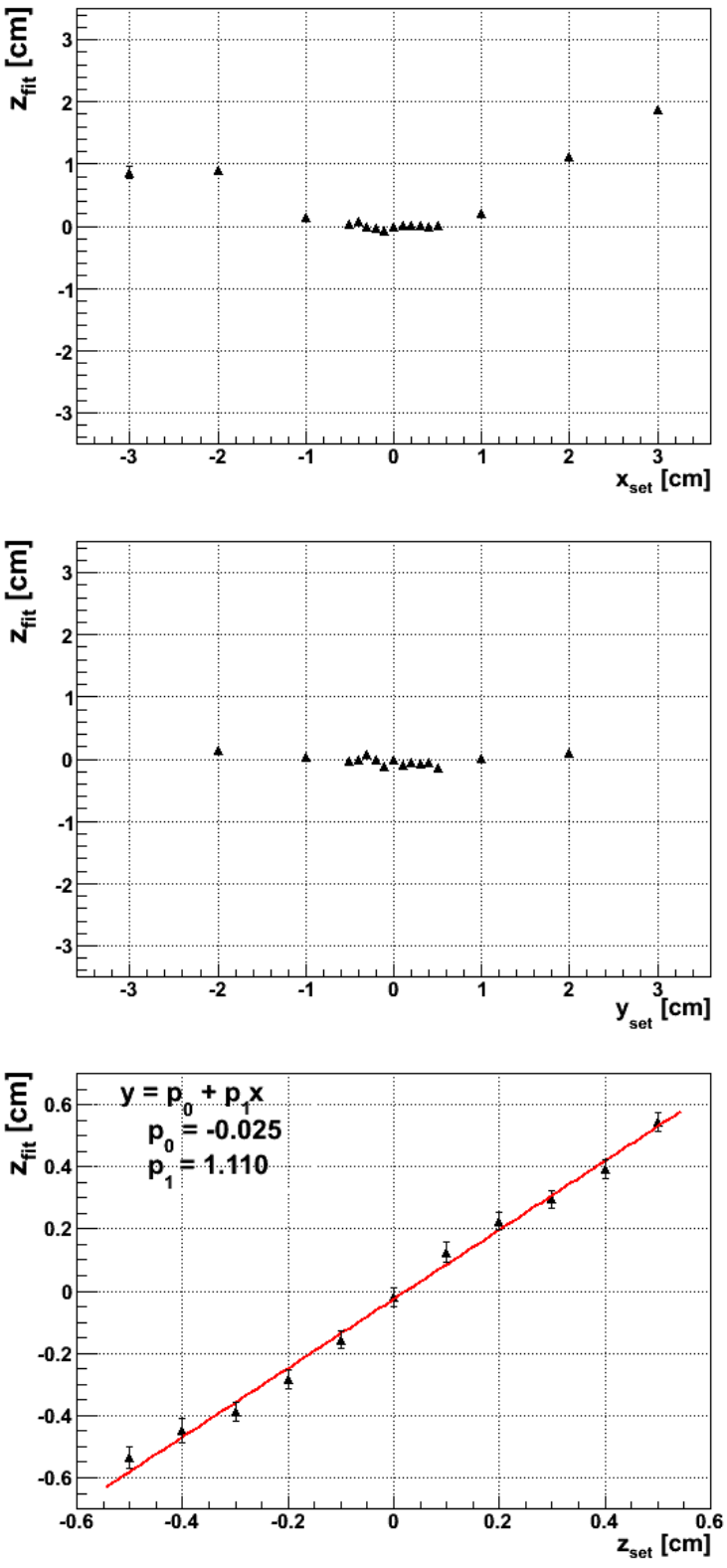

Figure 4.9: Results of reconstruction tests for the z coordinates of the reaction vertex for offsets in x, y and z.

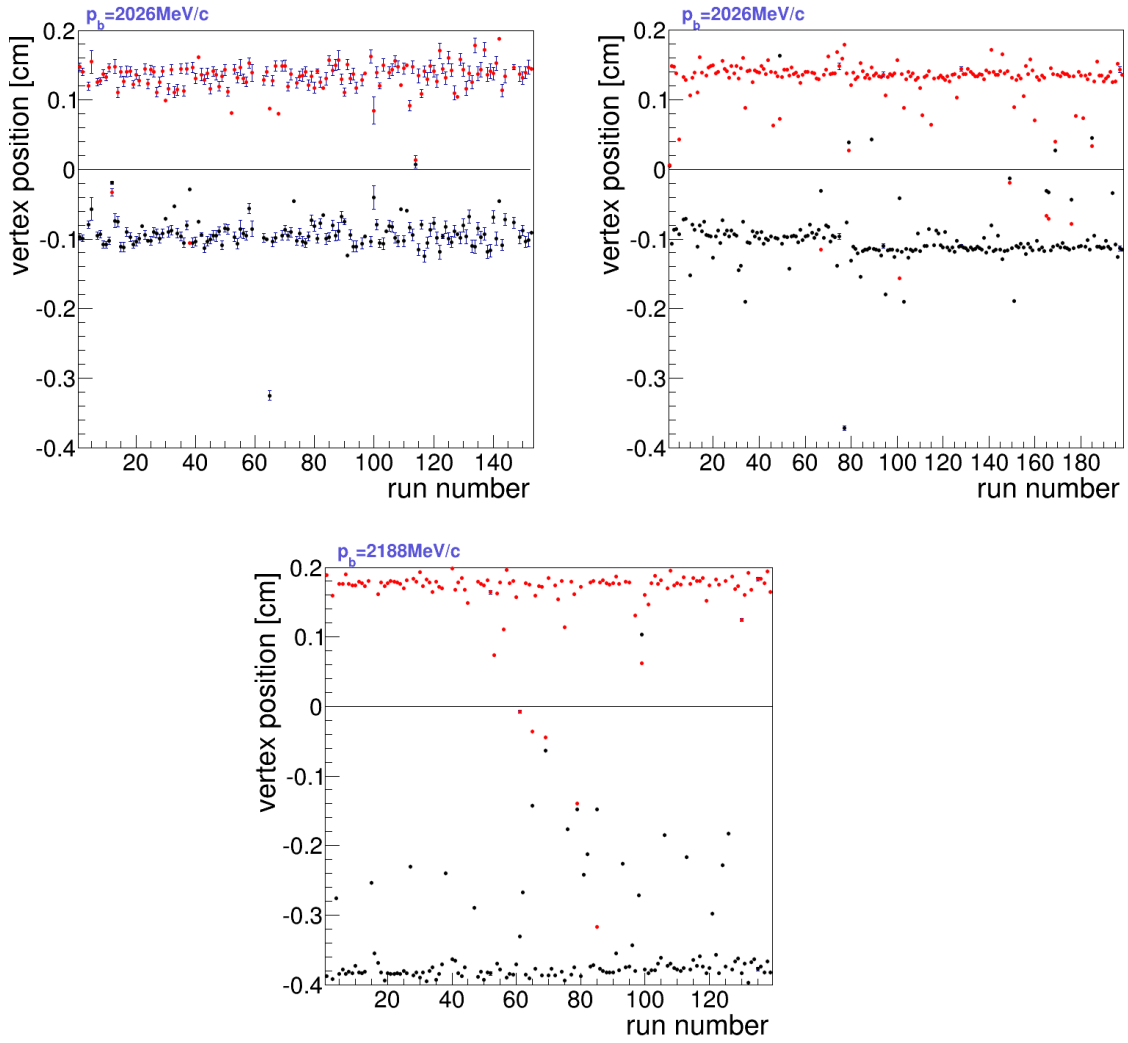

Figure 4.10: The vertex position as a function of the run number determined by mean of the distance method. The upper panel shows transversal coordinates for $p_{beam} = 2026$ MeV/c, with the unpolarized data in the left plot and the polarized data in the right plot. The lower panel shows longitudinal coordinates for $p_{beam} = 2188$ MeV/c. Black markers stand for the x coordinate, and red markers stand for the y coordinate.

vertex	$p_{beam}^{unpolarized}$=2.026 [GeV/c]	p_{beam}=2.026 [GeV/c]	p_{beam}=2.188 [GeV/c]
The coplanarity method			
x_v [cm]	-0.1164±0.0052	-0.1230±0.0011	-0.2834±0.0010
y_v [cm]	0.1119±0.0052	0.1099±0.0011	0.1551±0.0010
The distance method			
x_v [cm]	-0.0908±0.0017	-0.0968±0.0012	-0.3755±0.0019
y_v [cm]	0.1386±0.0019	0.1369±0.0011	0.1793±0.0015

Table 4.1: Result for the average mean of the vertex position obtained with both methods, achieved in the WASA-at-COSY experiment conducted in the year 2010.

Chapter 5

Determination of the polarization

5.1 Extraction of the $pp \to pp$ reaction

For the monitoring of the degree of polarization, luminosity and the detector performance, simultaneously to the $\vec{p}p \to pp\eta$ reaction, the proton-proton elastic scattering has been measured. In the case of the $\vec{p}p \to pp$ reaction, one proton is registered in the Forward Detector and the other in the Central Detector. The geometrical acceptance of the Forward Detector allows to measure protons in the range of 3° - 18°, and the Central Detector covers proton scattering angles from 60° to 84°. In the center of mass system this corresponds in total to the scattering angle in the range of 30° to 46°. To control the asymmetry of the detector, and to avoid some false asymmetry the spin of the protons was flipped from cycle to cycle.

Elastic scattered events were identified based on the energy deposited by protons in the FRH. The plot of deposited energy in the first layer of FRH vs all layers is shown in Fig. 5.1. The elastically scattered protons correspond to the most energetic protons of this distribution seen inside the red square.

In order to suppress the background events the coplanarity distribution, as was shown before in Fig. 4.1, was applied.

Examples of θ^*_{FD} vs θ^*_{CD} distributions for one run can be seen in Fig. 5.2. In order to estimate the background, for each bin in θ^*_{FD}, the θ^*_{CD} distribution was fitted separately with a fifth-order polynomial, excluding in the fit the range from 130° to 160°. Example of such distribution can be seen in Fig.5.3

By utilizing the $\triangle$E -E method in the Forward Range Hodoscope, the angular correlation of the outgoing protons and coplanarity condition events corresponding to the proton-proton elastic scattering were selected.

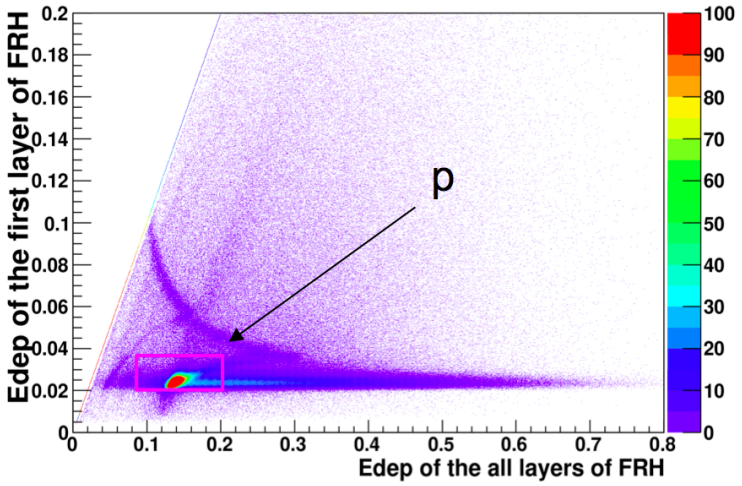

Figure 5.1: The distribution of the energy deposited by particles in the first layer FRH vs energy deposited in the whole FRH.

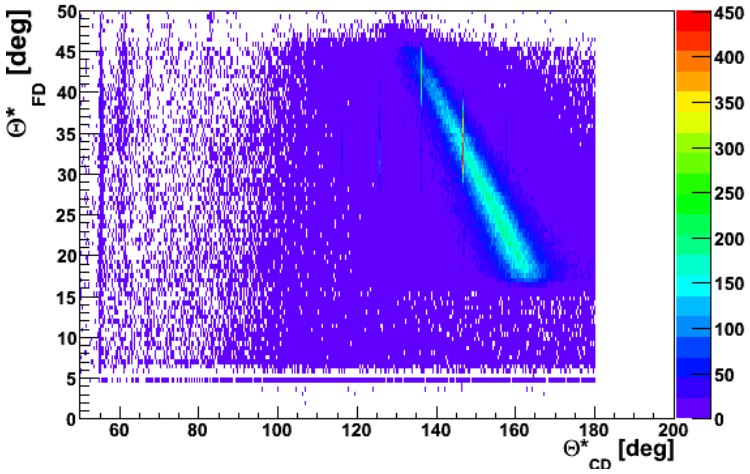

Figure 5.2: Example of the θ^*_{FD} vs θ^*_{CD} distribution.

5.2 Polarization value for both spin orientations

The number of events determined for the proton-proton elastic scattering for the different spin modes after background subtraction is plotted for the given θ^*_{FD} vs φ^*_{FD} in Fig. 5.4. For further calculations only two θ^*_{FD} ranges in the center of mass $[30° - 34°]$ and $[34° - 38°]$ were chosen, for which analyzing power is available from EDDA database [86] and the number of events was statistically sufficient. Next, asymmetry $\epsilon(\theta^*_{FD}, \varphi^*_{FD})$ was calculated using the

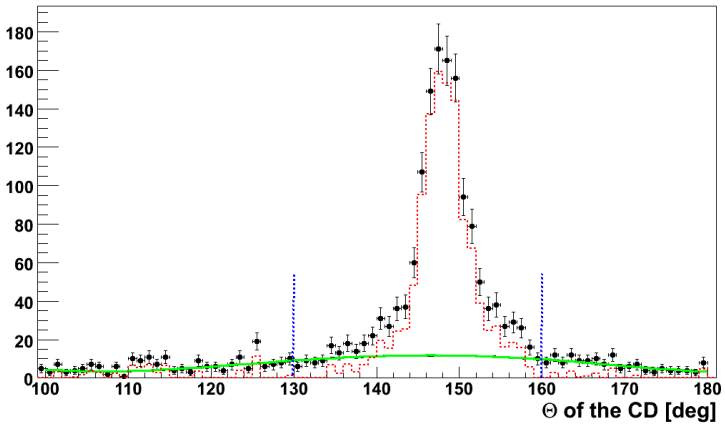

Figure 5.3: The distribution of θ^*_{CD} for $\theta^*_{FD} \in [30°, 34°]$, $\varphi \in [20°, 30°]$ and down spin mode. Points denote data. The green line corresponds to the fitted background, and the dotted red histogram shows the data after subtraction of the background.

formula:

$$\epsilon(\theta^*_{FD}, \varphi^*_{FD}) = \frac{N(\theta^*_{FD}, \varphi^*_{FD}) - N(\theta^*_{FD}, \varphi^*_{FD} + \pi)}{N(\theta^*_{FD}, \varphi^*_{FD}) + N(\theta^*_{FD}, \varphi^*_{FD} + \pi)}, \tag{5.1}$$

where $N(\theta^*_{FD}, \varphi^*_{FD})$ is the number of events around the angles $\Theta^*_{FD}, \varphi^*_{FD}$ and $N(\theta^*_{FD}, \varphi^*_{FD} + \pi)$ is the number of events on the opposite azimuthal angle. The available range θ^*_{FD} was divided into bins of 18° and φ^*_{FD} into bins of 10°. For each θ^*_{FD}, φ^*_{FD} the number of events was estimated by integrating the area under the red line as shown in Fig. 5.3.

To extract the polarization value we have plotted the asymmetry distributions as a function of ϕ^*_{FD} (Fig. 5.5).

Fitting the distribution of the asymmetry with the function $\epsilon(\theta^*_{FD}, \varphi^*_{FD}) = p_0 \cdot cos(\varphi^*_{FD})$, where $p_0 = P(\theta^*_{FD}) \cdot A_y(\theta^*_{FD})$, we can determine the polarization. Due to the configuration of the WASA detector, the φ^*_{FD} regions [-95°;-85°] and [85°;95°] were not included in the calculations.

In order to calculate the polarization one needs to know also A_y for the given value of the θ^*_{FD}. To obtain A_y at a desired beam momentum and to estimate a systematic uncertainty of this determination, two different functions are fitted to the momentum dependence of A_y measured by the EDDA collaboration [86] in these angular ranges as it is shown in Fig. 5.6. Extracted value of the A_y for the $p_{beam} = 2026$ MeV/c and $p_{beam} = 2188$ MeV/c are shown in Tab.5.1.

The degrees of proton beam polarization for each spin mode(up/down) are

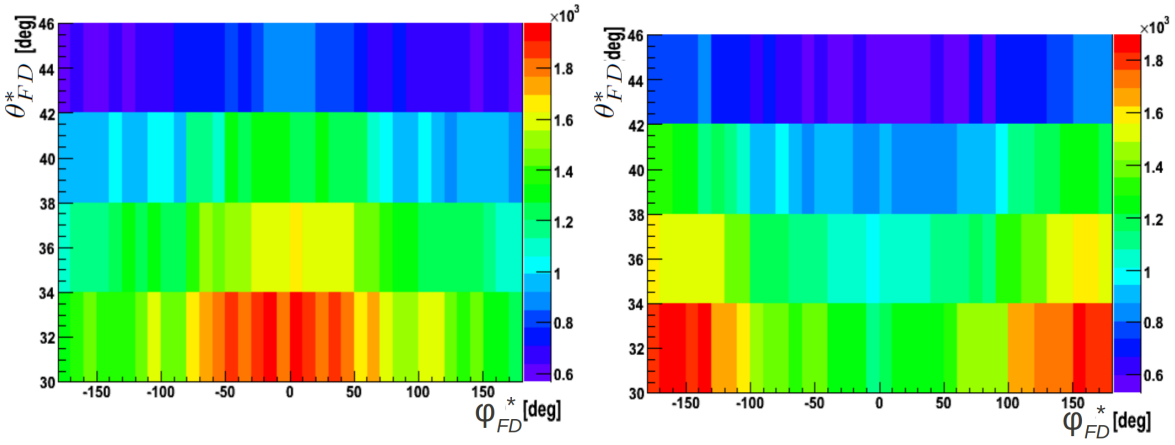

Figure 5.4: Example of the angular distribution for the elastic scattered events. Left: spin up mode. Right: spin down mode.

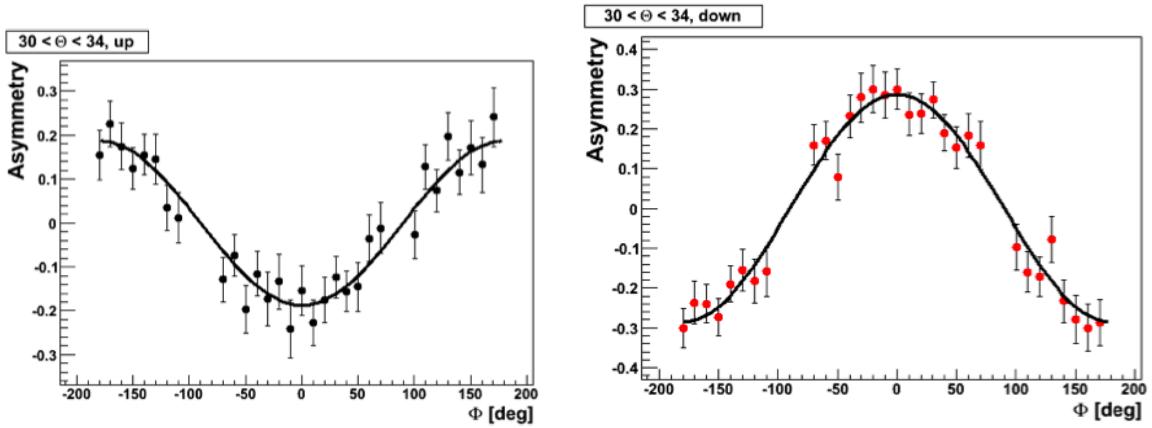

Figure 5.5: Experimental distributions of the asymmetry as a function of the proton's azimuthal angle, made for θ^*_{FD} range 30° - 34° (left) for spin down mode, and (right) for spin up mode. The black line represents the fit function given by Eq. 5.1.

extracted for the two ranges of the center-of-mass polar angle of the forward scattered proton. The final polarization for a given spin is then calculated as a weighted mean:

$$P = \frac{\sum_{i=1}^{n} P_i(\theta^*_{FD})/\sigma^2_{P_i(\theta^*_{FD})}}{\sum_{i=1}^{n} 1/\sigma^2_{P_i(\theta^*_{FD})}}, \tag{5.2}$$

where θ^*_{FD} is the scattering angle of the forward going proton, calculated in

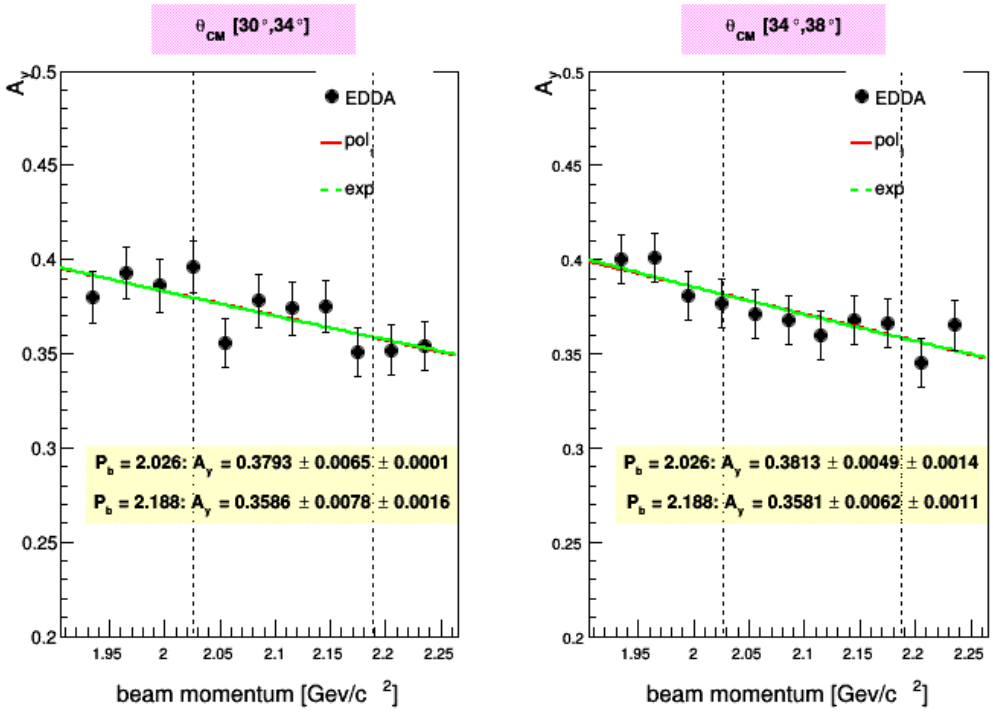

Figure 5.6: Distribution of A_y for $\vec{p}p \to pp$ reaction as a function of the beam momentum for the scattering angle ranges $\theta^* \in [30°, 34°]$ and $[34°, 38°]$ Points denote analyzing power measured from the EDDA collaboration. Green lines show exponential fit to the data points. Red line show with first order polynomials.

θ°_{cm}	$P_{beam} = 2.026$ GeV/c	$P_{beam} = 2.188$ GeV/c
$[30, 34]$	A_y=0.3793±0.0065$_{stat}$ ± 0.0001$_{syst}$	A_y=0.3586±0.0078$_{stat}$ ± 0.0016$_{syst}$
$[34, 38]$	A_y=0.3813±0.0049$_{stat}$ ± 0.0014$_{syst}$	A_y=0.3581±0.0062$_{stat}$ ± 0.0011$_{syst}$

Table 5.1: Analyzing power, A_y, extracted using EDDA data for two θ^*_{FD} angle ranges and two beam momenta.

the center-of-mass system and $\sigma^2_{P_i(\theta^*_{FD})}$ is a statistical uncertainty of the polarization.

The determined polarization value for the whole data set is shown in Fig. 5.7. The polarization was calculated for both orientations of the proton spin separately. Data points shown in Fig. 5.7 have been corrected for acceptance determined using the vertex position extracted from the experi-

mental data. For comparison, also the result assuming a nominal center of the vertex region $(v_x, v_y, v_z) = (0, 0, 0)$ is plotted. On the lower panel, the polarization obtained from data collected with an unpolarized beam is presented and, therefore, should be consistent with zero.

Value of the polarization analyzed as a one gathered sample shown in the Tab. 5.2. Please note that the values in the table are slightly different, but consistent with the values indicated in Fig. 5.7.

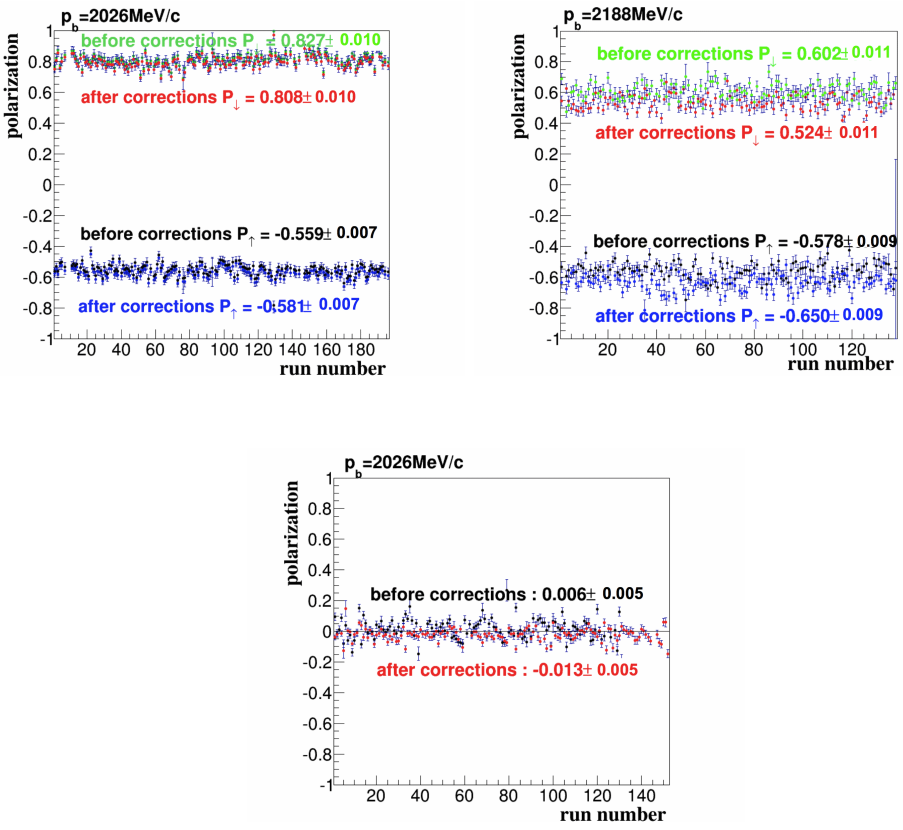

Figure 5.7: Distributions of polarization as a function of run number for polarized (upper panels) and unpolarized (lower panel) beam. Results for both polarization modes are shown. Upper panels show the data for the polarized proton beam for $p_b = 2026$ MeV/c (left) and for $p_b = 2188$ MeV/c (right). Lower panel show the polarization for the unpolarized proton beam measurements. Results in the legend denote values of the polarization as a average mean of the polarization defined for each run separately.

p_b[GeV/c]	spin mode	polarization
2026	down	0.793±0.010
	up	-0.577±0.007
2188	down	0.537±0.009
	up	-0.635±0.011
2026	unpolarized	-0.012±0.005

Table 5.2: The average polarization value extracted for two beam momenta and two beam spin modes with statistical uncertainty. Please note that the values in the table are slighly different, but consistent with the values indicated in Fig. 5.7. This is because the table show results for the polarization where the data was analyzed as one sample and not separately per run.

5.3 Systematic studies of the polarization

In order to determine a possible influence of the vertex position on the polarization, a sample of $pp \to pp$ reactions were simulated for various interaction point coordinates. The polarization was calculated individually for each data sample, where the position was changed in one direction. Then, each of the simulated data samples was analyzed with the assumption that the particle going forward originates from the nominal vertex $(x_v, y_v, z_v) = (0, 0, 0)$. Figure 5.8 shows polarization for different vertex locations as an average mean of the all runs, and the results of the polarization obtained as gathered data from all experiment shown in table 5.2.

The obtained result shows that the change of the y_v or z_v coordinate of the interaction point do not have an influence on the polarization value. However, a certain sensitivity of polarization is seen in case of changing the x_v coordinate. The value of the polarization depends linearly on the vertex x coordinate which is the result of changing the scattering angle of the proton emitted forward in the CM.

The distribution of the polarization as a function of the θ^*_{FD} can be seen in Fig.5.9. For $\theta_{CM} > 38°$ the polarization strongly deviates from the expected value when changing the x coordinate by more than 5 mm. Therefore, since the polarization for higher angles is biased by the systematic,the allowed θ_{CM} angle should be restricted to less than 38°. On the other hand, the observed dependency, if seen in experimental data, would be a clear sign of a wrong

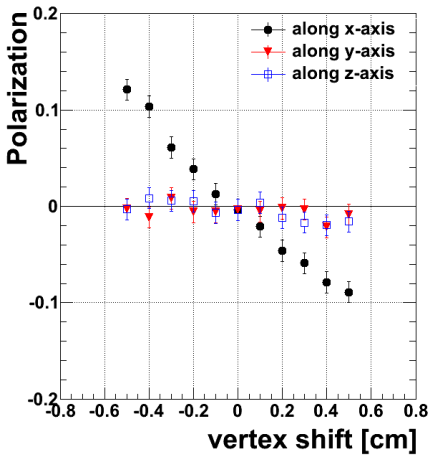

Figure 5.8: Polarization versus vertex shift along the x, y and z axis. Data were simulated for unpolarized beam (P=0) at positions as indicated in the figure and analyzed assuming vertex position at (0,0,0).

assumption of the x position of the interaction point.

In Fig. 5.10, the resulting polarization after correction of the assumed position of the interaction point is shown. Simulated data for four different vertex positions have been acceptance corrected assuming different values of the x_v coordinate, $x_{vertex}^{acceptance}$. In this case, the result is similar to the one in Fig. 5.8. It is important to notice that the results shown in Fig. 5.8 and Fig. 5.10 indicate that the uncertainties of the polarization determination due to the vertex position are smaller than 0.02 since the vertex position is determined with accuracy of $\pm$ 0.5 mm. This conclusion is independent of the 'true' position of the vertex, at least within a range of 5 mm. Furthermore, if y_v or z_v is set up to 5 mm and corrected to different $x_{vertex}^{acceptance}$, the influence on the polarization is negligible.

Another systematic change in the extraction of the polarization can be due to the tilt of the beam. The maximum allowed range of tilts of the beam at WASA-at-COSY is between -0.05 mrad and 0.05 mrad, symmetrically around the z-axis [97]. To determine how the tilt of the beam affects the polarization, the angles α_x and α_y between the beam and the z axis in the yz plane and xz plane, respectively, were varied. In Fig. 5.11, the polarization as a function of the angle α for both beam tilts is shown. One can see that within the estimated uncertainty there are no effects observed in the studied range, except that the polarization slightly differs from zero (by up to $\pm$1% [95]).

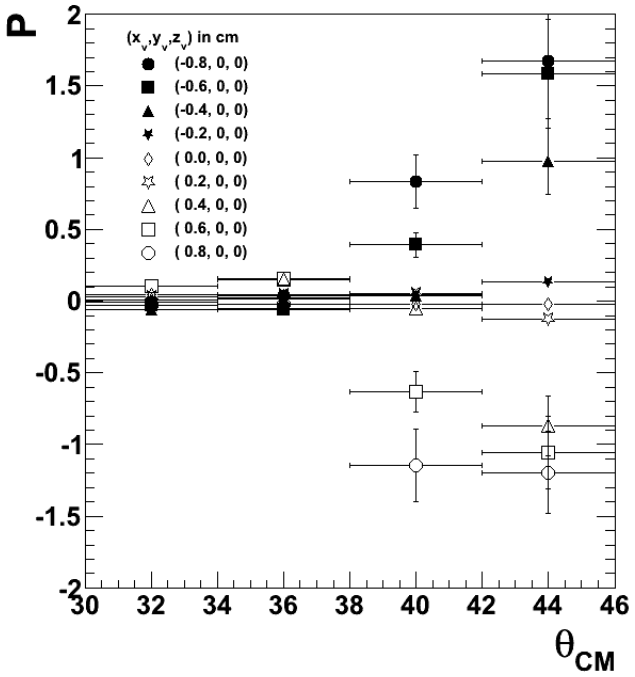

Figure 5.9: Distribution of the reconstructed polarization as a function of the scattering angle of the forward going proton (center-of-mass scattering), determined from the data simulated for unpolarized beam (P=0%) with different values of the $x-$coordinate of the interaction point (see the legend).

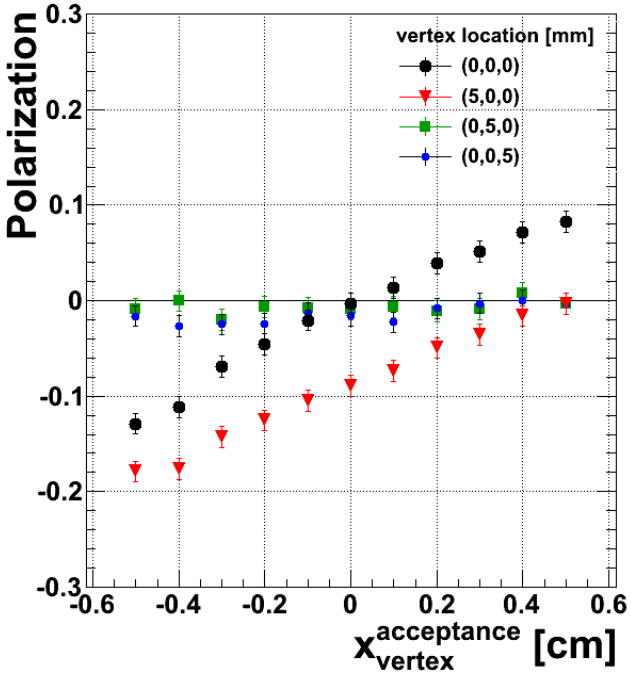

Figure 5.10: Figure shows results of the analysis of data simulated for unpolarized beam (P=0) with vertex positions as indicated in the legend.Vertical axis shows polarization as a function of x coordinate assumed in the analysis for the estimation of the acceptance. The polarization was calculated for four actual locations of the interaction point, as shown in the legend.

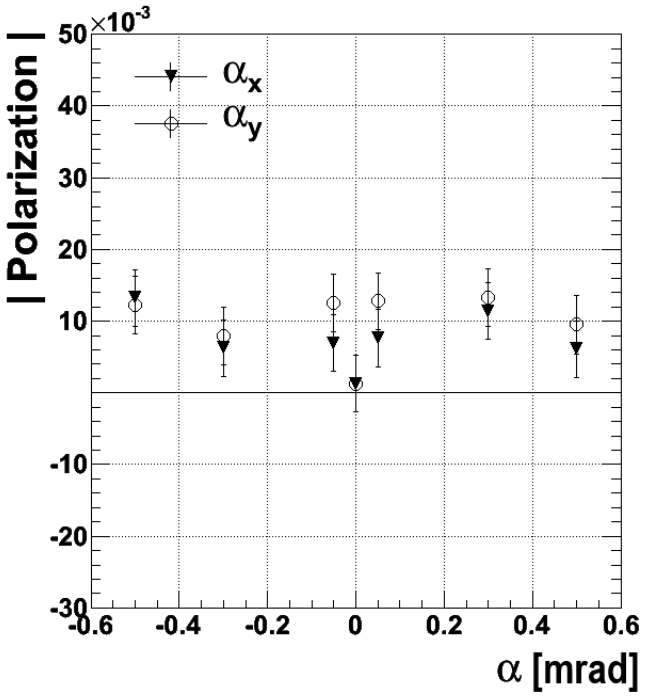

Figure 5.11: Distribution of the polarization as a function of the degree of the beam tilt (simulations). The beam is tilted both in the yz plane (filled triangles) and in the xz plane (open circles). The studied range is ten times larger than the range of the possible tilt allowed by the COSY optics [97].

Chapter 6

Determination of the $\vec{p}p \to pp\eta$ reaction

In this section, the missing mass spectra for each beam momentum (2026 MeV/c and 2188 MeV/c) and reaction ($\vec{p}p \to pp\eta \to pp\gamma\gamma$ and $\vec{p}p \to pp\eta \to pp3\pi^0 \to pp6\gamma$) are presented separately. The common approach to the determination of the main reaction is introduced.

6.1 Identification of the $\vec{p}p \to pp\eta \to pp\gamma\gamma$ reaction

The η meson is an uncharged short-living particle, thus it is direct registration is not possible. In the case of the conducted experiment there was no magnetic field which prevented the registration and further reconstruction of trajectories of charged particles. Therefore, only two neutral decays can be selected in the analysis: $\eta \to 2\gamma$ and $\eta \to 3\pi^0 \to 6\gamma$. For the purpose of extracting the number of the η mesons produced, several techniques such as missing mass and invariant mass were introduced.

As a first step of selection in the forward part of the detector two charged particles were requested, corresponding to the two scattered protons. In order to distinguish these protons from other charged particles, a selection based on the ΔE-E method was applied (described in Sec. 5.2). The plot showing the applied condition is shown in Fig 6.1. Additionally signals of two or more neutral particles were required in the central part of the detector.

For the identification of events corresponding to the reaction chain $\vec{p}p \to pp\eta \to pp\gamma\gamma$ both the missing mass and invariant mass technique were applied.

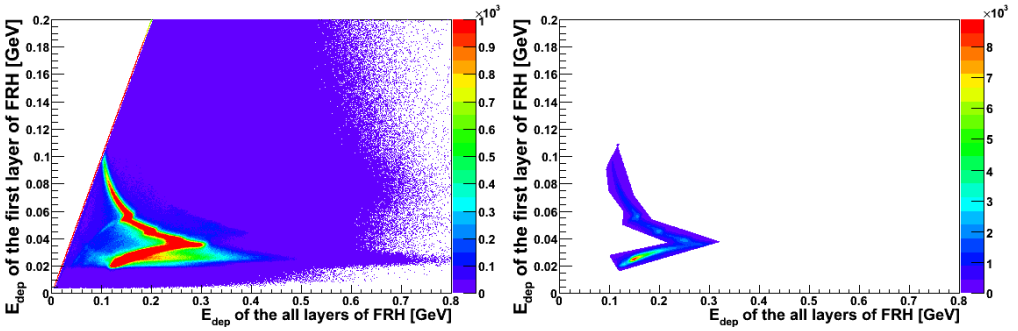

Figure 6.1: Distribution of the energy deposited in all layers of FRH vs first layer of FRH. ΔE-E method for the selection of protons for η decay channels. Left: before graphical cut. Right: after graphical cut.

The missing mass m_X of an unregistered particle X in the $\vec{p}p \to ppX$ reaction can then be calculated as:

$$m_X^2 = E_X^2 - \vec{p_X^2} = (\mathbf{P_{beam}} + \mathbf{P_{target}} - \mathbf{P_1} - \mathbf{P_2})^2 = \\ (E_{beam} + E_{target} - E_1 - E_2)^2 - (\overrightarrow{p_{beam}} + \overrightarrow{p_{target}} - \vec{p_1} - \vec{p_2})^2 \quad (6.1)$$

where $\mathbf{P_{beam}} = (E_{beam}, \overrightarrow{p_{beam}})$, $\mathbf{P_{target}} = (m_{target}, 0)$, $\mathbf{P_1} = (E_1, \vec{p_1})$ and $\mathbf{P_2} = (E_2, \vec{p_2})$ denote the four momenta of the beam, target and two detected protons, respectively.

The invariant mass technique enables to reconstruct the four momentum of the η meson, based on the four-momenta of the decay products. The general formula for the invariant mass reads:

$$m_x = \sqrt{\Big(\sum_i E_i\Big)^2 - \Big(\sum_i \vec{p_i}\Big)^2}, \quad (6.2)$$

where E_i and p_i correspond to the energies and momenta of the η meson decay products.

In the present analysis we considered $\eta \to \gamma\gamma$ and $\eta \to 3\pi^0$. Exemplary missing mass and invariant mass distributions for the reaction $\vec{p}p \to pp\eta \to pp\gamma\gamma$, collected for the beam momentum 2026 MeV/c, are shown in Fig. 6.2. Each spectrum includes events for both spin orientations. In order to select only events corresponding to the searched decay channel and improve the signal to background ratio a selection cut has been applied restricting the invariant mass to the range from 0.35 GeV/c^2 - 0.75 GeV/c^2 only.

The same selection plots of missing and invariant mass for the beam momentum p_{beam}=2188 MeV/c are presented in Fig. 6.3.

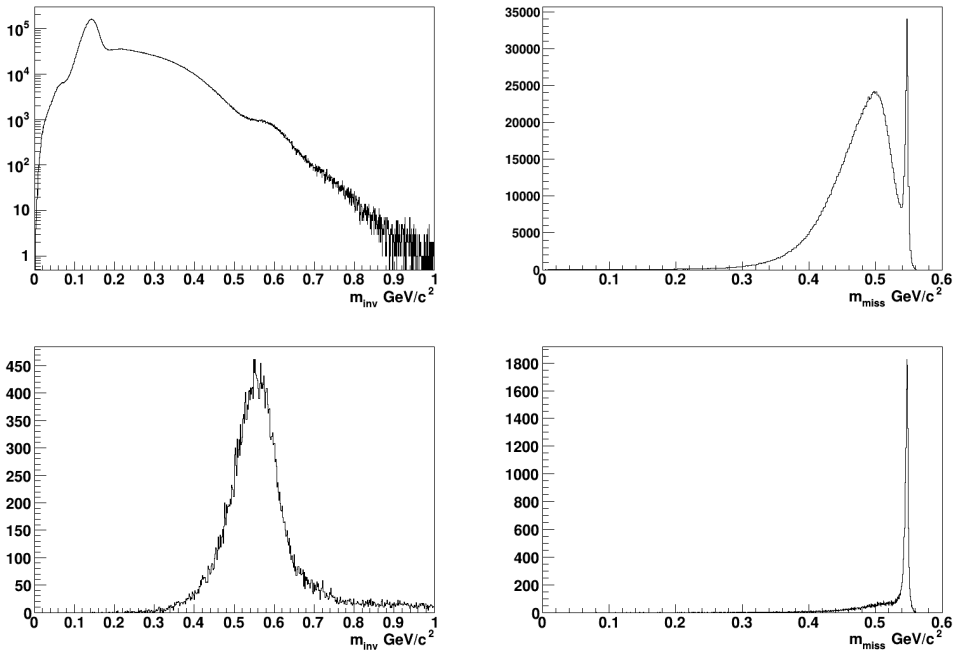

Figure 6.2: Distribution of the invariant mass (upper left) and missing mass (upper right) for $p_{beam} = 2026$ MeV/c and the decay $\eta \to \gamma\gamma$. Distribution of the invariant mass (lower left) and missing mass (lower right) for $p_{beam} = 2026$ MeV/c and for the decay $\eta \to 3\pi^0 \to 6\gamma$.

For the lower beam momentum clear signals are visible in the missing mass spectra for both decay channels (2γ and 6γ). In the case of the 6γ a clear signal is also seen in the invariant mass spectrum whereas for the 2γ case a signal from the η meson is less pronounced due to the relatively large background. For the higher momentum (Fig. 6.3) one can also see signals from the η meson. However in this case the missing mass resolution is worse with respect to the lower momentum which is due to the kinematic effects discussed e.g. in reference [24].

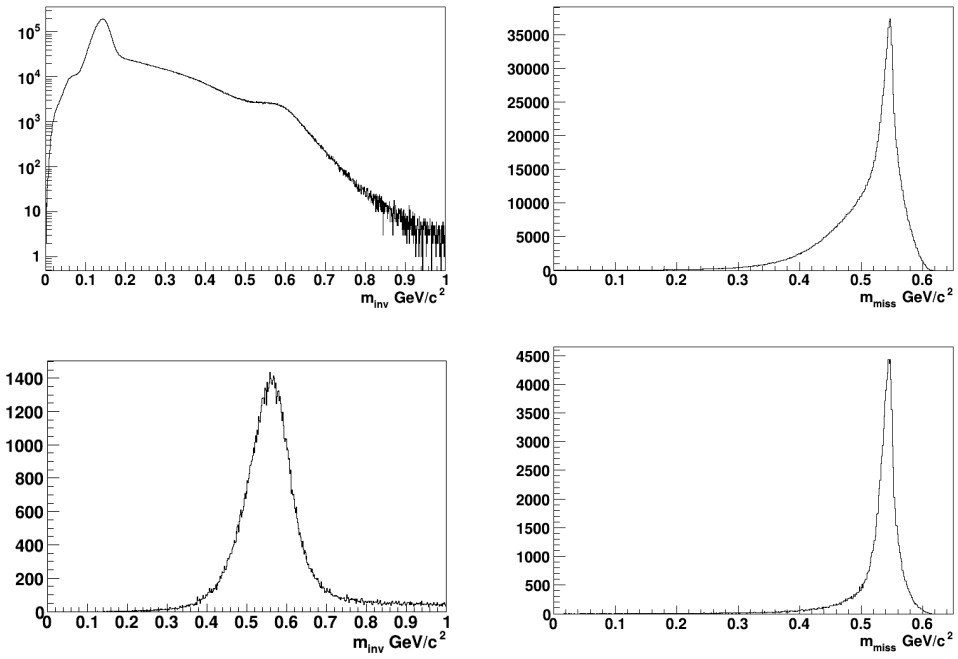

Figure 6.3: Distribution of the invariant mass (upper left) and missing mass (upper right) for $p_{beam} = 2188$ MeV/c and the reaction $\eta \to \gamma\gamma$. Distribution of the invariant mass (lower left) and missing mass (lower right) for $p_{beam} = 2188$ MeV/c and for the reaction $\eta \to 3\pi^0 \to 6\gamma$.

6.2 Identification of the $\vec{p}p \to pp\eta \to pp3\pi^0 \to pp6\gamma$ reaction

The $\eta \to 3\pi^0 \to 6\gamma$ decay has the the second highest branching ratio: $39.31 \pm 0.20\%$ from all possible η decay channels. To select this channel in the analysis two charged particles were requested in the forward detector (corresponding to two scattered protons) and more than six clusters in the electromagnetic calorimeter, corresponding to photons.

For $\eta \to 3\pi^0 \to 6\gamma$ we have six gamma quanta in the exit channel. Therefore, a routine has to be elaborated which matches each 2 gamma quanta into pairs originating from the π^0 decay. Out of a large amount of possible combinations the most probable one has to be identified. In order to do that the squared invariant mass of every possible pair of gamma quanta was calculated. Absolute values of the differences between the invariant mass of the pair and the π^0 mass values were compared and the pairs with the smallest χ^2 value

were chosen for future analysis.

Examples of invariant and missing mass spectra for the $\vec{p}p \to pp\eta \to 3\pi^0 \to pp6\gamma$ reaction, collected for both beam momenta, are shown in the lower panels of Fig. 6.2 and Fig. 6.3. Each spectrum includes events for both spin orientations.

The peak in the invariant mass distribution of the 6 photons is broad (see lower left panels in Fig. 6.2 and Fig. 6.3). For the lower beam momentum, $p_{beam} = 2026$ MeV/c, we use the same cut for the invariant mass as for the two-photon decay of the η meson. For the higher beam momentum, $p_{beam} = 2188$ MeV/c, we select events with an invariant mass between 0.3 GeV/c^2 and 0.8 GeV/c^2.

6.3 Background subtraction

In this section we will describe the methods used for the background subtraction from the missing mass spectra.

For both beam momenta we have simulated direct multipion production namely via reactions: $pp \to pp\pi^0, pp \to pp2\pi^0, pp \to pp3\pi^0$, and $pp \to pp4\pi^0$. The simulated background function was fitted to the data excluding the range of the η meson signal. The difference between the data and the simulated background corresponds to the η meson signal. The background was evaluated for each spin mode separately. Exemplary spectra for the chosen angular range are shown in Fig. 6.4 and Fig. 6.5 (red crosses). The black curve shows the spectrum of the data and the blue curve shows the sum of the Monte Carlo simulations of the background channels.

It is visible that the systematic uncertainty due to the background is small for the reaction $\vec{p}p \to pp\eta \to pp3\pi^0 \to pp6\gamma$ since the signal to background ratio is high.

Exemplary distributions used for the extractions of the η events for the ranges $\varphi_\eta \in [-180°, -170°]$ and $\theta_\eta \in [70°, 90°]$ are shown in Fig. 6.4. The procedure of η event extraction was applied to the whole range of φ_η and θ_η and corrected for the acceptance of the WASA detector. The acceptance was determined for each $(\theta_\eta, \varphi_\eta)$ bin separately as the fraction of generated events and events registered in the WASA detector. The correction for the vertex position based on elastically scattered events was taken into account for the acceptance calculation as well and the corresponding plot is shown in Fig. 6.6.

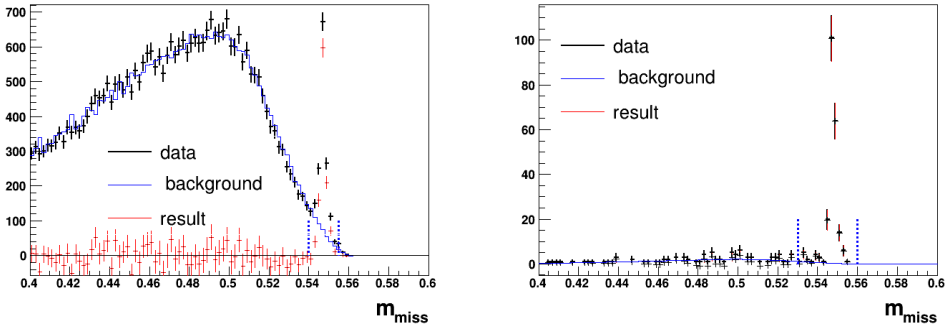

Figure 6.4: Missing mass distribution for the chosen range $70° < \theta_\eta < 90°$, $-180° < \varphi_\eta < -170°$ and spin "up" mode. Left: $\eta \to \gamma\gamma$. Right: $\eta \to 3\pi^0 \to 6\gamma$. Beam momentum: $p_{beam} = 2026$ MeV/c. Black crosses denote experimental data. Continuous blue lines show the sum of the simulated background for $\pi^0, 2\pi^0, 3\pi^0$ and $4\pi^0$ production. Red crosses show the experimental data after background subtraction. Dashed blue lines show the region of the extraction of the number of produced η mesons.

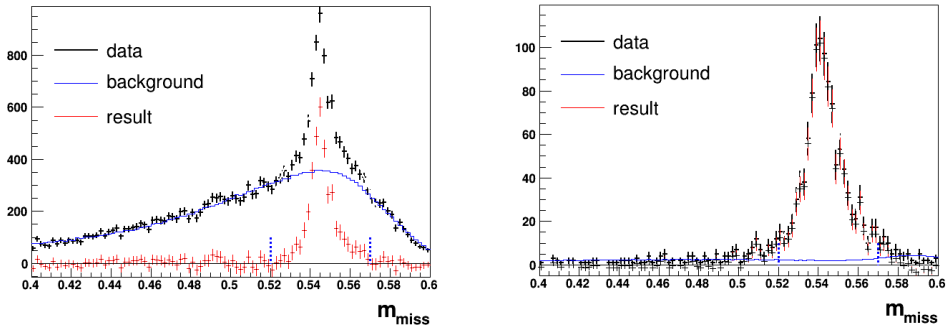

Figure 6.5: Missing mass distribution for the chosen range $70° < \theta_\eta < 90°$, $-180° < \varphi_\eta < -170°$ and spin "up" mode. Left: $\eta \to \gamma\gamma$. Right: $\eta \to 3\pi^0 \to 6\gamma$. Beam momentum: $p_{beam} = 2188$ MeV/c. Black crosses denote experimental data. Continuous blue lines show the sum of the simulated background for the $\pi^0, 2\pi^0, 3\pi^0$ and $4\pi^0$ production. Red lines show the result of difference between the experimental data and simulated background. Dashed blue lines show the region of the extraction of the number of produced η meson.

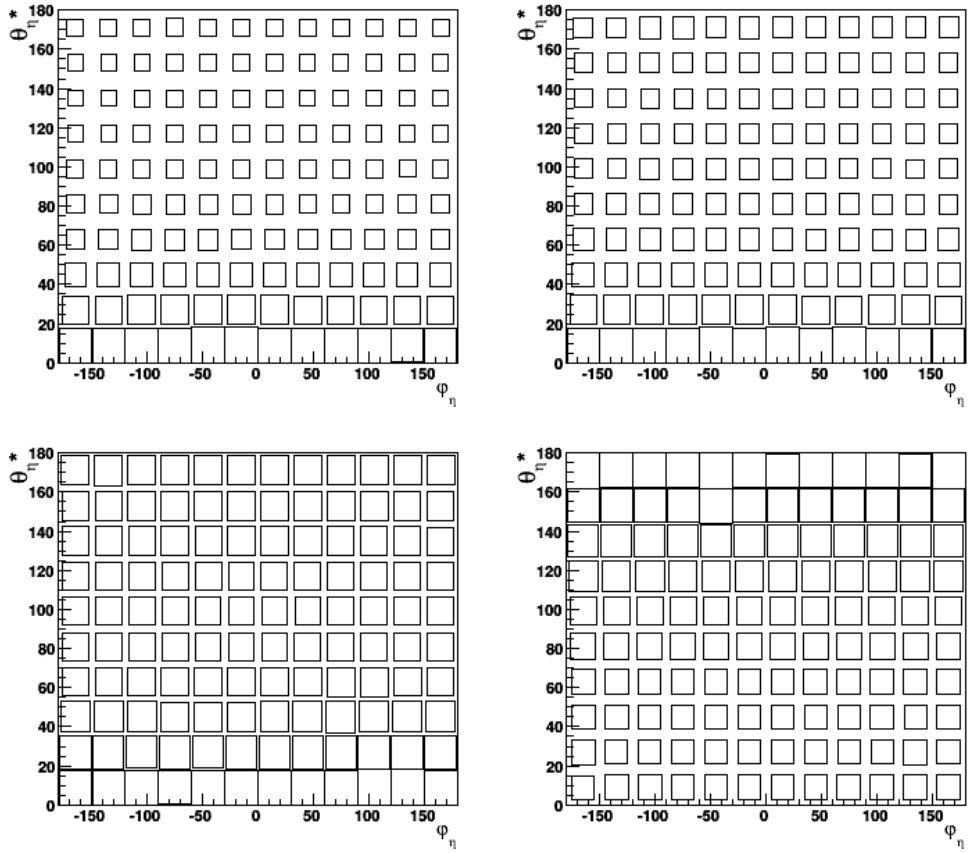

Figure 6.6: Acceptance of the WASA-at-COSY detector for the reaction $\eta \to 2\gamma$ (left) and $\eta \to 3\pi^0 \to 6\gamma$ (right). Upper panel: $p_{beam} = 2026$ MeV/c, lower panel: $p_{beam} = 2188$ MeV/c. The size of the square is proportional to the value of the acceptance. The smallest square denotes value of $0.193(\eta \to 2\gamma)$, $0.052(\eta \to 3\pi^0 \to 6\gamma)$ for 2026 MeV/c and $0.221(\eta \to 2\gamma)$, $0.033(\eta \to 3\pi^0 \to 6\gamma)$ for 2188 MeV/c. The largest square denotes value of $0.769(\eta \to 2\gamma)$, $0.152(\eta \to 3\pi^0 \to 6\gamma)$ for 2026 MeV/c and $0.316(\eta \to 2\gamma)$, $0.074(\eta \to 3\pi^0 \to 6\gamma)$ for 2188 MeV/c.

Chapter 7

Determination of the analyzing power A_y for the $pp \to pp\eta$ reaction

7.1 Madison convention

In order to calculate the analyzing power A_y for the η meson the Madison convention [98] is applied for the three-body system. Figure 7.1 presents schematically the production of the η meson in the accelerator reference frame. The z axis is parallel to the incident proton beam, while the y axis points vertically upwards. The x axis points to the left when viewed along the z axis.

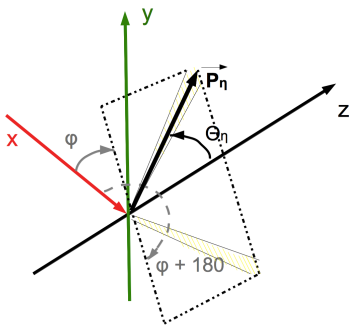

Figure 7.1: Scattering plane of the η meson. The dotted line shows the scattering plane of the η meson. θ_η describes the polar angle between the z axis and the outgoing η meson. The azimuthal angle φ_η defines the orientation of the scattering plane relative to the x axis.

The sign of an event scattered in the given φ_η and θ_η bin is determined according to the Madison convention.

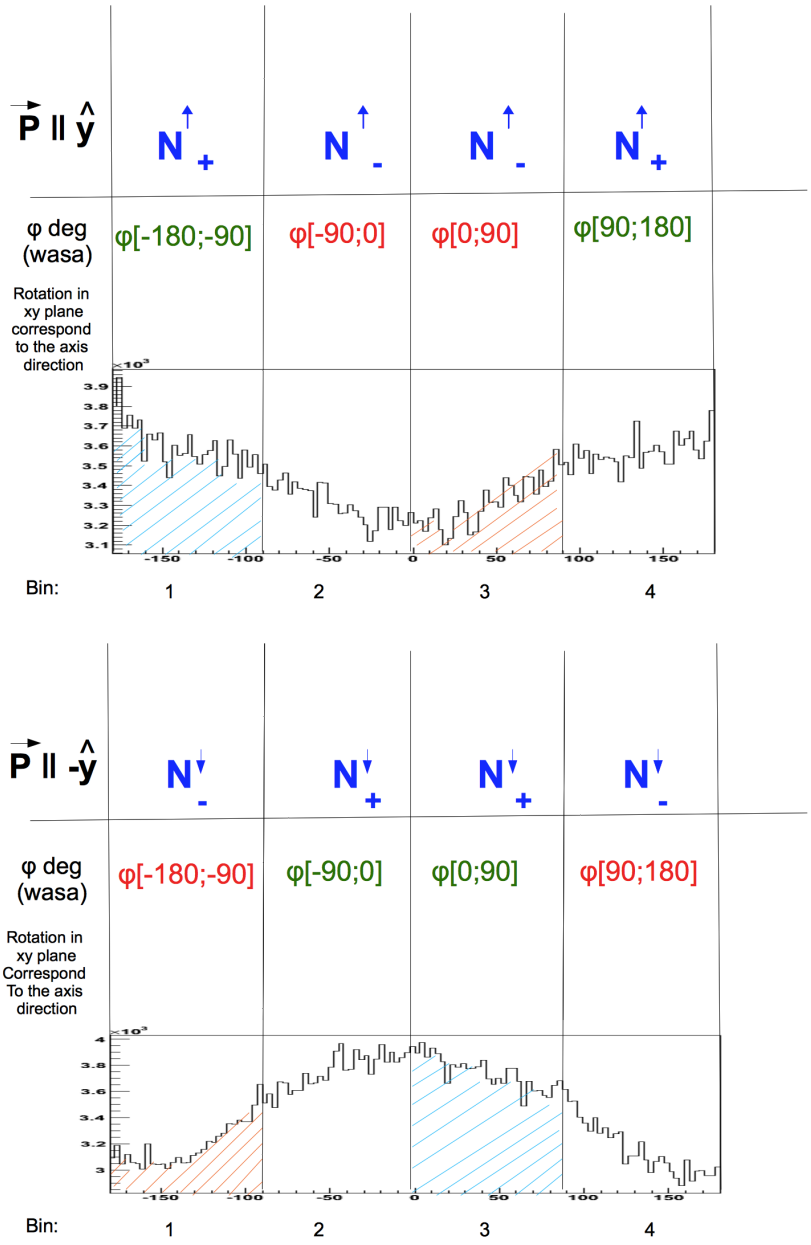

Figure 7.2: Assignment of the sign in the calculations of the analyzing power according to the Madison convention for the case (upper panel) when the polarization vector is parallel to the y axis (is pointing up) and (lower panel) when it is anti-parallel (pointing down).

The "+" sign is assigned to an event if the cross product of the vector of the beam direction z and the momentum vector of the η meson is parallel to the vector of polarization. If this cross product is anti-parallel to the polarization

vector the "-" sign is assigned to the event. This is important to know in the calculation of the asymmetry for the η meson. Figure 7.2 shows schematically the asymmetry for the φ_η distribution. This histogram shall help in understanding the Madison convention for the η meson. From Fig. 7.2 one can see that the sign assigned to the events changes every 90°.

The analyzed set of data contains about 400,000 events with an η meson for both beam energies, which allows to divide the φ_η angle into 12 bins and the θ_η angle into 10 bins. Figure 7.2 shows the division of φ_η into four bins as an example used for the explanation of the Madison convention. In the final analysis the data set is divided into 12 (φ_η) × 10 (θ_η) = 120 $(\varphi_\eta, \theta_\eta)$ bins.

7.2 Analyzing power A_y for the $pp \to pp\eta$ reaction

The calculation of $A_y(\theta_\eta)$ was performed in the center-of-mass system separately for the two decay channels $\eta \to 2\gamma$ and $\eta \to 3\pi^0$ and separately for the spin "up" and spin "down" orientation for the two beam momenta $p_{beam} = 2026$ MeV/c and $p_{beam} = 2188$ MeV/c. The number of η events were acceptance corrected according to Fig. 6.6.

The asymmetry for two different spin orientation is defined as:

$$\epsilon_\eta^\uparrow(N(\theta_\eta, \varphi_\eta), N(\theta_\eta, \varphi_\eta + \pi)) \equiv \frac{N_\eta^\uparrow(\theta_\eta, \varphi_\eta) - N_\eta^\uparrow(\theta_\eta, \varphi_\eta + \pi)}{N_\eta^\uparrow(\theta_\eta, \varphi_\eta) + N_\eta^\uparrow(\theta_\eta, \varphi_\eta + \pi)} \tag{7.1}$$

$$\epsilon_\eta^\downarrow(N(\theta_\eta, \varphi_\eta), N(\theta_\eta, \varphi_\eta + \pi)) \equiv \frac{N_\eta^\downarrow(\theta_\eta, \varphi_\eta + \pi) - N_\eta^\downarrow(\theta_\eta, \varphi_\eta)}{N_\eta^\downarrow(\theta_\eta, \varphi_\eta + \pi) + N_\eta^\downarrow(\theta_\eta, \varphi_\eta)} \tag{7.2}$$

To extract the analyzing power the experimental distributions have to be fitted with the following function:

$$\epsilon(\theta_\eta, \varphi_\eta) = P \cdot A_y(\theta_\eta) \cdot cos\phi_\eta \tag{7.3}$$

where P denotes the polarization.

The fit of the asymmetry was performed separately for each spin orientation of the polarized proton beam. An example of those fits is given in Fig. 7.3 through 7.6.

The analyzing power was calculated for each spin orientation (up and down) and was extracted for the whole range of the center-of-mass polar angle φ_η of

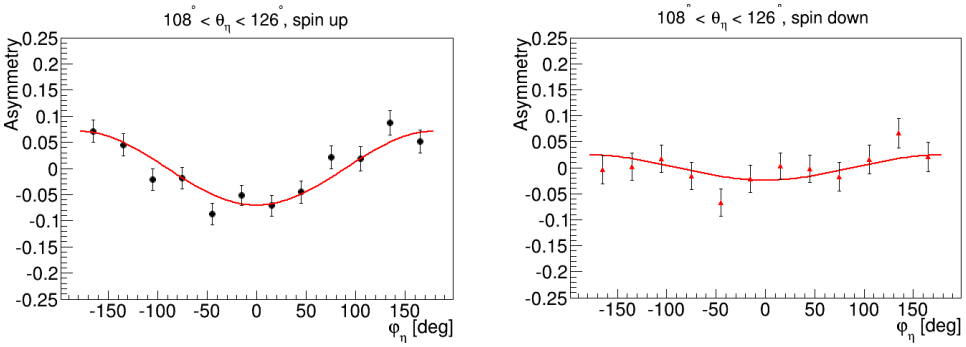

Figure 7.3: Example distributions of asymmetry vs φ_η for chosen θ_η angular intervals. In this figure the results for $p_b = 2026$ MeV/c and the decay channel $\eta \to \gamma\gamma$ are presented.

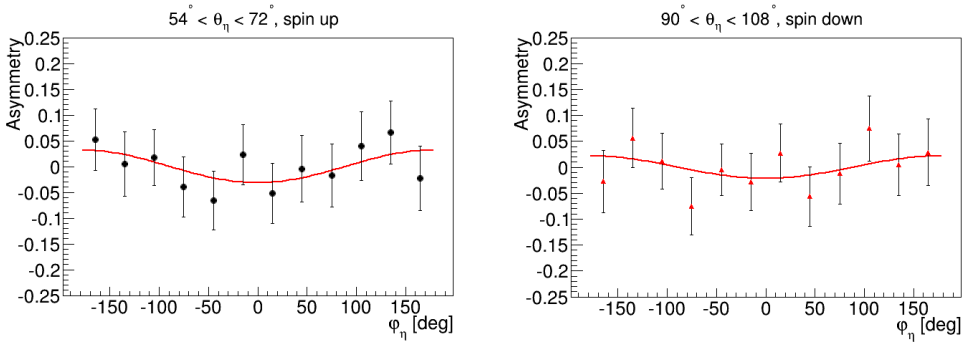

Figure 7.4: Example distributions of asymmetry vs φ_η for chosen θ_η angular intervals. In this figure the results for $p_b = 2026$ MeV/c and the decay channel $\eta \to 3\pi^0$ are presented.

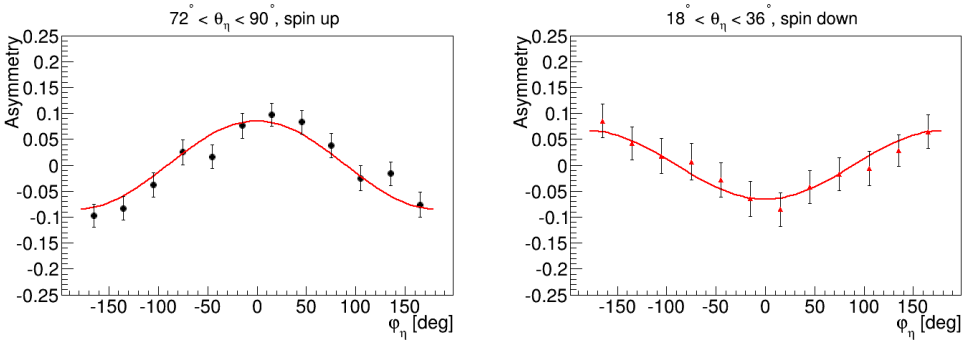

Figure 7.5: Example distributions of asymmetry vs φ_η for chosen θ_η angular intervals. In this figure the results for $p_b = 2188$ MeV/c and the decay channel $\eta \to \gamma\gamma$ are presented.

the θ_η meson. This angle was divided into 10 angular ranges, 18° degrees each. The azimuthal angle φ_η was divided into 12 angular ranges, 30° degrees each.

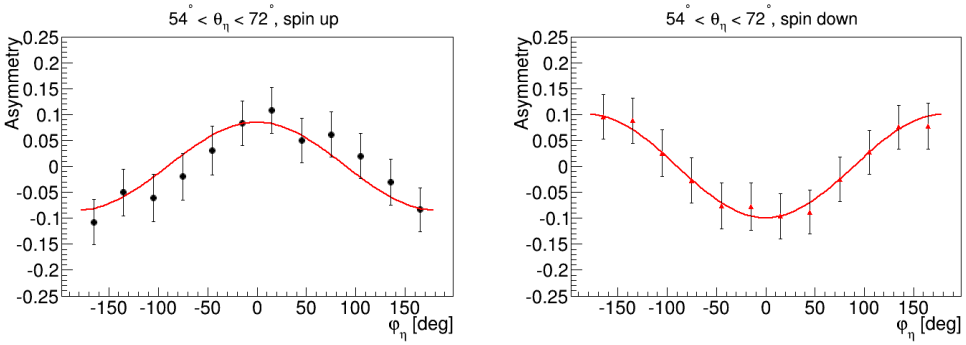

Figure 7.6: Example distributions of asymmetry vs φ_η for chosen θ_η angular intervals. In this figure the results for $p_b = 2188$ MeV/c and the decay channel $\eta \to 3\pi^0$ are presented.

In the next step for each decay mode and for each θ_η bin a weighted average of $A_y(\theta_\eta)$ was calculated from the results obtained for the two spin orientations (see Fig. 7.7). Furthermore, for each θ_η bin a final result of A_y was obtained as a weighted average of the results determined for the 2γ and 6γ decay modes. Figure 7.8 shows again the over the spin orientation average weighted value of the analyzing power.

For systematic checks the same analysis was performed using the measurements with the unpolarized beam. The asymmetry for the unpolarized measurements are consistent with zero, and the calculated analyzing power is within the uncertainties consistent with zero.

Several tests described in Chapter 7.3 have been performed for the calculation of the systematic uncertainty of the analyzing power.

Figure 7.10 and Tab. 7.1 shows to the angular distribution of the analyzing power for the η meson. For the studies on the systematic uncertainty of the background subtraction of the missing mass spectra the data were also analyzed by dividing the data into bins in $\cos\theta_\eta$. For each $\cos\theta_\eta$ range a missing mass spectra were determined for each of the 12 φ_η bins. Finally, for each missing mass spectrum the asymmetry and A_y was determined. The result is shown in Fig. 7.10 and Tab. 7.2.

The final result of the analyzing power of the η meson is presented in Fig. 7.9 and Fig. 7.10. One can see that the result of this thesis agrees with the previous results of the COSY-11 experiment. However, the precision is much improved.

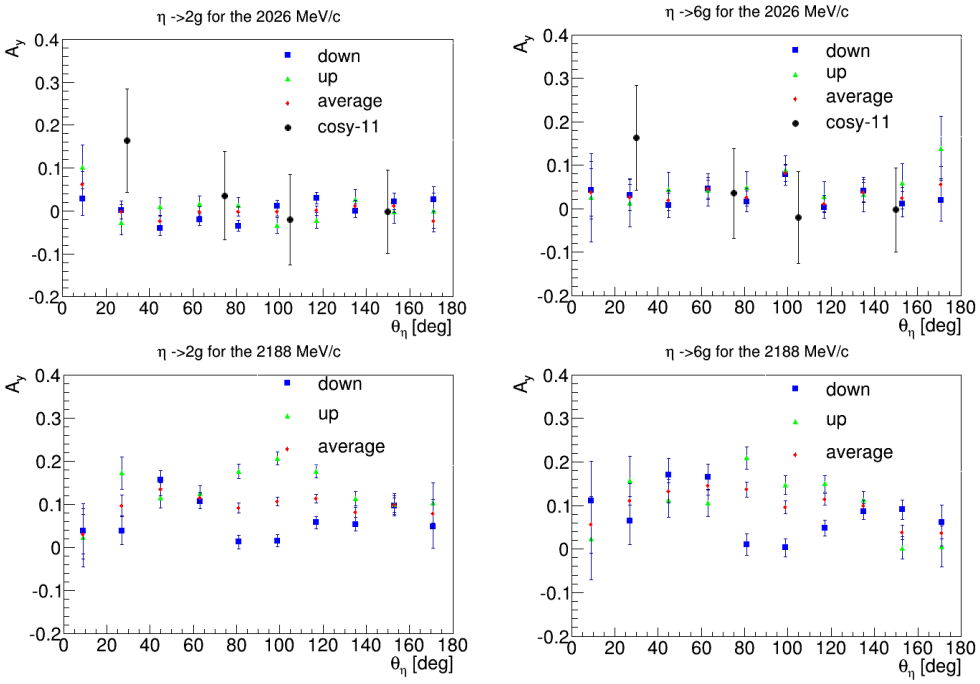

Figure 7.7: Result for the analyzing power of the η meson. Upper panel: $p_b = 2026$ MeV/c. Black circles correspond to the COSY-11 experimental points [55]. Lower panel: $p_b = 2188$ MeV/c. Left plots show results for the analysis based on the $\eta \to 2\gamma$ decay, and right plots show $\eta \to 6\gamma$.

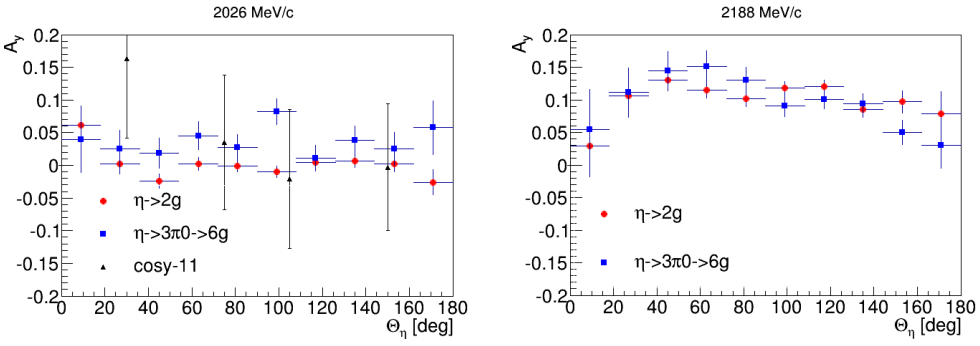

Figure 7.8: Result for the analyzing power of the η meson for different reactions. Left: $p_b = 2026$ MeV/c. Right: $p_b = 2188$ MeV/c. Black triangles correspond to the COSY-11 experimental points [55].

θ_η°	$A_y \pm stat \pm syst$ (2026 MeV/c)	$A_y \pm stat \pm syst$ (2188 MeV/c)
$[0, 18)$	0.056 ± 0.027± 0.011	0.038± 0.046± 0.045
$[18, 36)$	0.008± 0.015± 0.011	0.107± 0.024± 0.022
$[36, 54)$	-0.016± 0.011± 0.022	0.133± 0.015± 0.017
$[54, 72)$	0.009± 0.009± 0.021	0.123± 0.013± 0.014
$[72, 90)$	0.004± 0.009± 0.014	0.108± 0.011± 0.011
$[90, 108)$	0.005± 0.009± 0.046	0.110± 0.010± 0.009
$[108, 126)$	0.005± 0.009± 0.003	0.114± 0.010± 0.008
$[126, 144)$	0.013± 0.010± 0.015	0.088± 0.012± 0.013
$[144, 162)$	0.006± 0.012± 0.012	0.076± 0.017± 0.013
$[162, 180]$	-0.011± 0.019± 0.041	0.055± 0.033± 0.024

Table 7.1: Analyzing power determined for the momenta 2026 MeV/c and 2188 MeV/c as the average mean from the $\eta \to 2\gamma$ and $\eta \to 3\pi^0$ reactions for the different θ_η ranges with final selection criteria.

$cos(\theta_\eta)$	$A_y \pm stat \pm syst$ (2026 MeV/c)	$A_y \pm stat \pm syst$ (2188 MeV/c)
$[-1., -0.8)$	0.122 ± 0.030± 0.054	0.080± 0.043± 0.033
$[-0.8, -0.6)$	0.035± 0.017± 0.038	0.103± 0.023± 0.019
$[-0.6, -0.4)$	-0.002± 0.011± 0.026	0.141± 0.014± 0.013
$[-0.4, -0.2)$	-0.007± 0.009± 0.004	0.102± 0.012± 0.011
$[-0.2, 0.)$	0.005± 0.009± 0.022	0.087± 0.011± 0.009
$[0., 0.2)$	-0.009± 0.009± 0.032	0.099± 0.010± 0.008
$[0.2, 0.4)$	-0.025± 0.009± 0.027	0.131± 0.011± 0.008
$[0.4, 0.6)$	0.007± 0.010± 0.019	0.103± 0.012± 0.008
$[0.6, 0.8)$	-0.009± 0.010± 0.009	0.113± 0.019± 0.012
$[0.8, 1.]$	0.011± 0.016± 0.041	0.044± 0.049± 0.028

Table 7.2: Analyzing power determined for the momenta 2026 MeV/c and 2188 MeV/c as the average mean from the $\eta \to 2\gamma$ and $\eta \to 3\pi^0$ reactions for the different $\cos\theta_\eta$ ranges with final selection criteria.

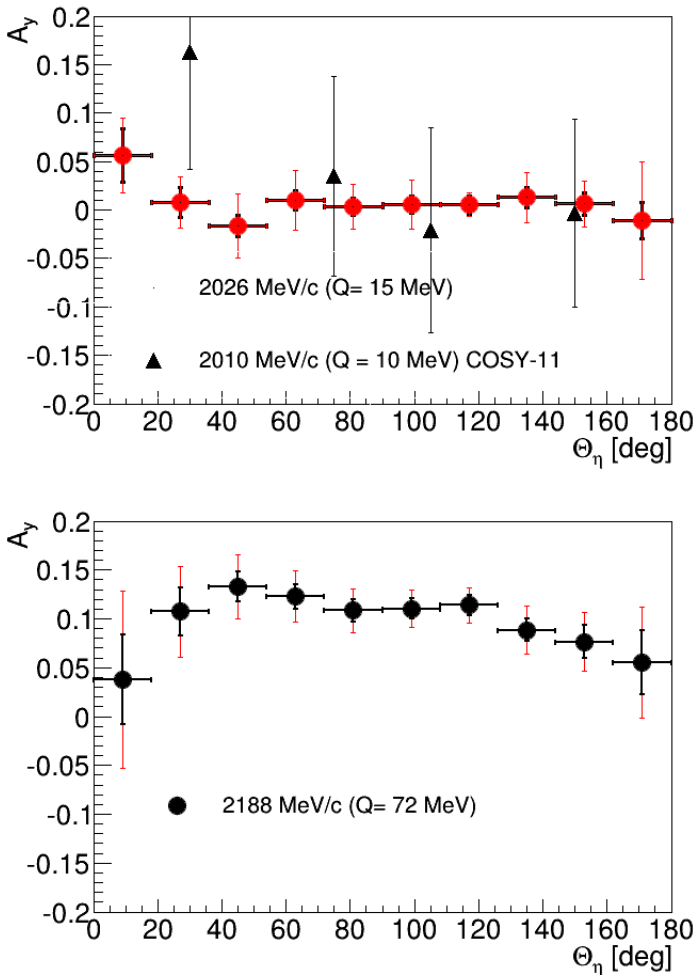

Figure 7.9: Analyzing power of the η meson as a function of θ_η for Q = 15 MeV (upper panel) and Q = 72 MeV (lower panel). Triangles show the result of the analyzing power for the COSY-11 experiment. Statistical errors are shown in black colour while the sums of the systematical errors and statistical errors are shown in red colour. Horizontal bars indicate angular bins.

7.3 Systematic checks for the η meson analyzing power A_y

The extraction of the η meson was done with several methods. Final selection criteria were used to extract the number of η mesons from the missing mass distribution which is presented in the Tab. 7.1 and Tab. 7.2. The fit ranges for the missing mass distribution are given in Tab. 7.3 and Tab. 7.4 for each

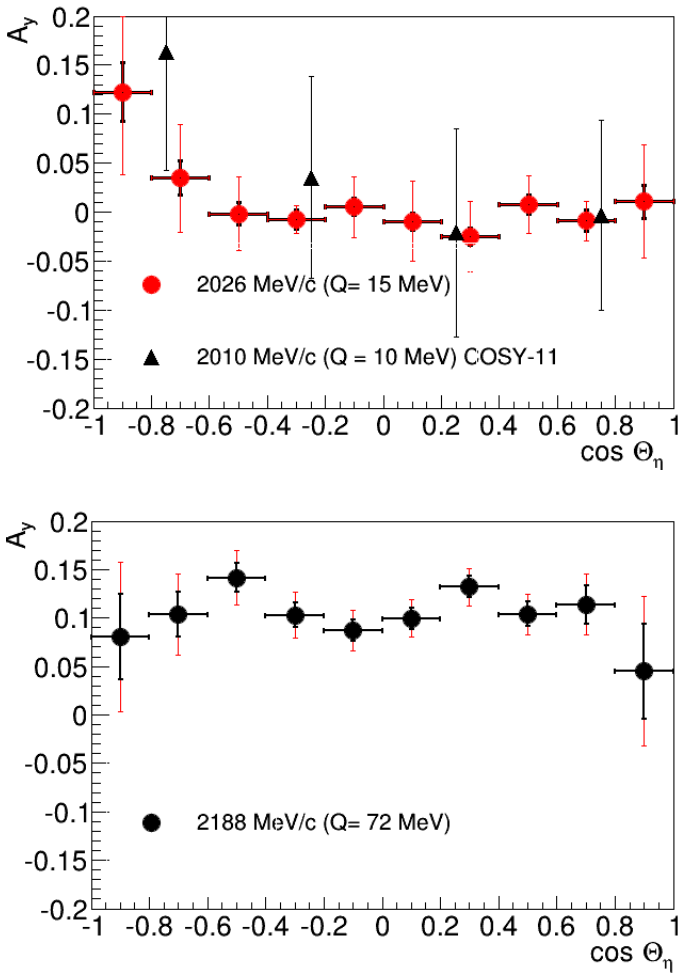

Figure 7.10: Analyzing power of the η meson as a function of the $cos\theta_\eta$ for the Q=15 MeV (upper panel) and Q=72 MeV (lower panel). Triangles show the result of the analyzing power for the COSY-11. Statistical errors are shown in black colour while the sums of the systematical errors and statistical errors are shown in red colour. Horizontal bars indicate bins of $\cos\theta_\eta$.

beam momentum.

The results of the systematic effect studies for $p_{beam} = 2026$ MeV/c can be seen in Tab. B.1 and for $p_{beam} = 2188$ MeV/c in Tab. B.2.

The first column of the Tab. B.1 and Tab. B.2 shows the θ_η region for the calculation of the $A_y(\theta)$.

Test 1 (second column) was done to test the influence of the particle identification. For this purpose the cut on the energy, $\Delta E - E$, which defines the protons detected in the FD, was increased by 100 %. The cut on the invariant

mass of gammas from η decay was also increased by 100 %.

Test 2 (third column) was done for the investigation of the influence of how the η mesons were counted. For this purpose $\pm 2\sigma$ of the width of the simulated missing mass distributions around the η mass was used in the calculations.

Test 3 (fourth column) was done using systematic uncertainty in the polarization calculation, which is mainly due to the uncertainty in the determination of the vertex position. The vertex position with a systematic precision of 0.05 cm was estimated (see Tab. 4.1). This corresponds to the uncertainty in polarization of 0.01 (see Fig. 5.8 and Tab. 5.10).

Test 4 was performed for the systematic check in the calculation of the analyzing power from reactions $\eta \to 2\gamma$ and $\eta \to 3\pi^0$. The result of this test is shown in column 5, and it is calculated as:

$$\Delta A_y test4 = \frac{A_{y(\eta\to 2\gamma)} - A_{y(\eta\to 3\pi^0)}}{2}. \tag{7.4}$$

Using the Barlow method [99] which is recommended by the WASA-at-COSY collaboration we evaluated the systematic uncertainty. The deviation between the final result of the analyzing power of the η meson and the result obtained after the change is compared to $\Delta\sigma$,which is defined as:

$$\Delta\sigma = \sqrt{\sigma_f^2 - \sigma_c^2} \tag{7.5}$$

where σ_f^2 denotes the statistical uncertainty of the final result and σ_c^2 the statistical uncertainty of the result after change of the cuts. In this work we have made four tests, so c=1,2,3,4.

The result of the Barlow method can be seen in Tab. B.1 and Tab. B.2 in columns number six, seven and eight for the corresponding tests. The same systematic checks were performed for calculations based on $\cos\theta_\eta$ and the result is shown in Tab. B.3 and Tab. B.4. $\Delta\sigma_4$ for the test four calculated as:

$$\Delta\sigma_4 = \sqrt{\sigma^2_{\eta\to 2\gamma} - \sigma^2_{\eta\to 3\pi^0}} \tag{7.6}$$

For the estimation of the systematic uncertainty the value of ΔA_y was taken for which the ratio $\frac{\Delta A_y}{\Delta\sigma}$ was larger than 1. If all tests resulted in values of $\frac{\Delta A_y}{\Delta\sigma}$ smaller than 1 then conservatively this value of ΔA_y was taken for which this parameter is the largest. This value depends on the θ_η region. However, for the higher energy the largest coefficient corresponds to the test 4, which describes the measurements based on the $\eta \to 2\gamma$ and $\eta \to 3\pi^0$ reactions.

θ_η°	$\eta \to \gamma\gamma$	$\eta \to 3\pi^0$
$[0, 18)$	[0.54; 0.555]	[0.522; 0.552]
$[18, 36)$	[0.54; 0.555]	[0.522; 0.552]
$[36, 54)$	[0.54; 0.555]	[0.53; 0.555]
$[54, 72)$	[0.54; 0.555]	[0.53; 0.555]
$[72, 90)$	[0.54; 0.555]	[0.54; 0.555]
$[90, 108)$	[0.54; 0.555]	[0.54; 0.555]
$[108, 126)$	[0.54; 0.555]	[0.54; 0.555]
$[126, 144)$	[0.54; 0.555]	[0.54; 0.555]
$[144, 162)$	[0.535; 0.555]	[0.53; 0.555]
$[162, 180]$	[0.535; 0.555]	[0.53; 0.555]

Table 7.3: Fit ranges used for the missing mass distribution for $p_{beam} = 2026$ MeV/c.

θ_η°	$\eta \to \gamma\gamma$	$\eta \to 3\pi^0$
$[0, 18)$	[0.52; 0.56]	[0.52; 0.56]
$[18, 36)$	[0.53; 0.56]	[0.53; 0.56]
$[36, 54)$	[0.53; 0.56]	[0.53; 0.56]
$[54, 72)$	[0.53; 0.56]	[0.53; 0.56]
$[72, 90)$	[0.54; 0.56]	[0.53; 0.56]
$[90, 108)$	[0.52; 0.56]	[0.53; 0.57]
$[108, 126)$	[0.52; 0.56]	[0.5; 0.57]
$[126, 144)$	[0.505; 0.56]	[0.505; 0.565]
$[144, 162)$	[0.5; 0.56]	[0.5; 0.56]
$[162, 180)$	[0.5; 0.56]	[0.5; 0.56]

Table 7.4: Fit ranges used for the missing mass distribution for $p_{beam} = 2188$ MeV/c.

Chapter 8

Interpretation of the result

The predictions of the pseudoscalar meson exchange dominance model and the vector meson exchange model are compared with the data.

8.1 Pseudoscalar meson and vector meson exchange models

Possible scenarios which can lead to η meson production are shown in Fig. 2.1. The latest experiment [25], which was discussed in the motivation, showed that production mechanisms involving a pseudoscalar meson or a vector meson are likely candidates. A pseudoscalar meson is a meson with total spin 0 and odd parity, usually denoted as $J^P = 0^-$ (e.g. π meson). A vector meson has total spin 1 and odd parity, usually denoted as $J^P = 1^-$ (e.g. ρ meson). In order to find out which theoretical model describes properly the creation of the η meson in proton-proton collisions, it is necessary to compare the angular distribution of the analyzing power of the η meson with predictions based on corresponding theories.

Figure 8.1 shows the analyzing power for the reaction $pp \rightarrow pp\eta$ as a function of the polar angle of the emitted η meson in the center-of-mass system. Statistical uncertainty for the analyzing power are shown in black. Uncertainty corresponding to the sum of the statistical and systematical uncertainty are shown in color.

The dotted lines are the predictions based on the pseudoscalar meson exchange model [16] , whereas the solid lines represent the results of the calculations based on the vector meson exchange model [17]. Those theories were previously, at least to some extent, inspired by the COSY-11 data (black tri-

angles on Fig. 8.1 and Fig. 8.2). One can see that the current theories do not explain the new results determined in this thesis. Therefore, the new theoretical descriptions of the η meson production processes are needed.

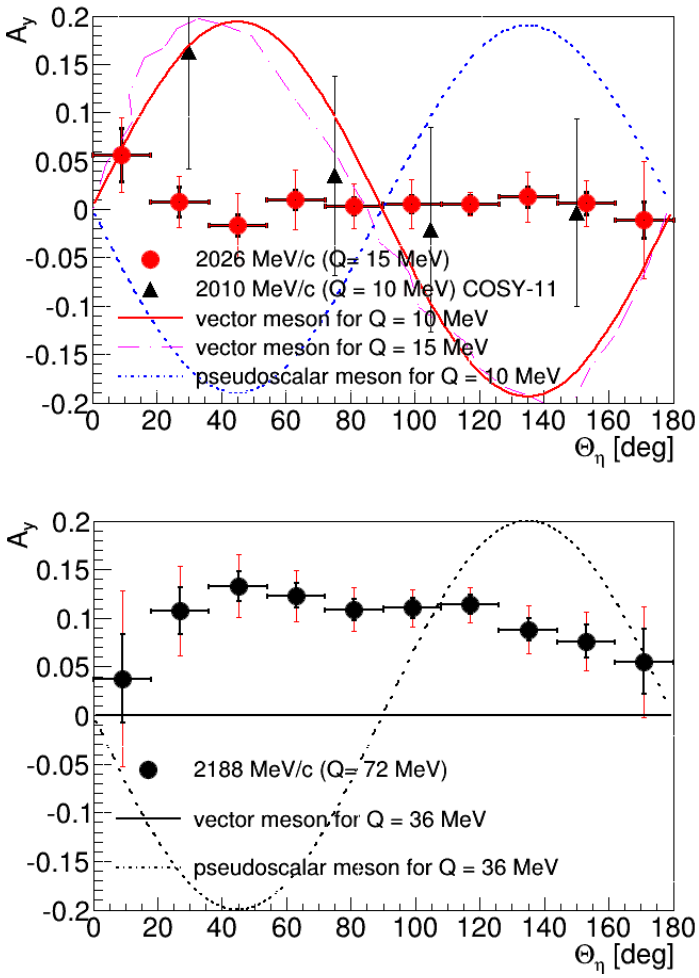

Figure 8.1: Analyzing power of the η meson as a function of θ_η. Comparison of the shape of the angular distribution with the theoretical predictions (see legend) for Q = 15 MeV (upper panel) and Q = 72 MeV (lower panel). The dashed-dotted line shows the prediction of the analyzing power as a function of the η emission angle in the center-of-mass for the vector meson dominance model [67]. The solid line shows the result for the vector meson model [17] and the dotted line shows result of the pseudoscalar model [16].

The same distribution of the analyzing power can be plotted as a function of $cos\theta_\eta$ (see Fig. 8.2).

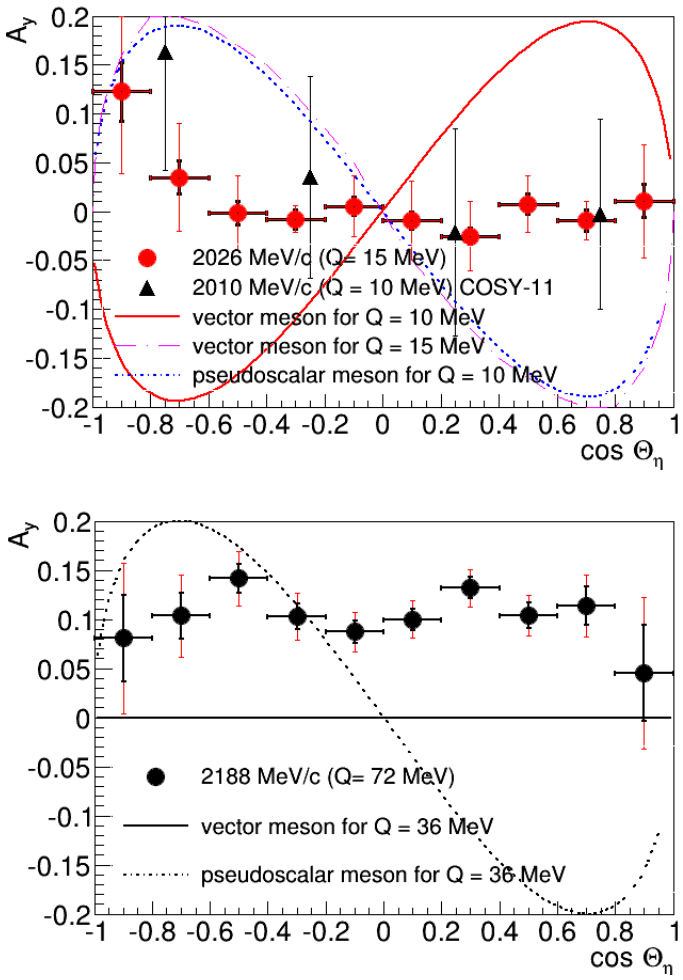

Figure 8.2: Analyzing power of the η meson as a function of $cos\theta_\eta$. Comparison of the shape of the angular distribution with the theoretical predictions (see legend) for Q = 15 MeV (upper panel) and Q = 72 MeV (lower panel).The dashed-dotted line shows the prediction of the analyzing power as a function of the η emission angle in the cener-of-mass for vector meson dominance model [67]. The solid line describe vector meson model for [17] and the doted line describe the pseudoscalar model [16].

8.2 The associated Legendre polynomial

Based on the knowledge of the angular dependence of the analyzing power one can try to figure out which partial waves take place in the reaction. The eigenfunctions of the angular momentum of the initial state for the η meson

are:

$$\psi_i = \exp(ikz) = \sum_{\ell}(2\ell+1)\cdot i^{\ell}\cdot j_{\ell}(kr)\cdot P_{\ell}(cos\theta_{\eta}), \tag{8.1}$$

where k is the wave number of the incoming wave plane, r is the radius, P^{ℓ} denotes the Legendre polynomial for angular momentum ℓ and $j_{\ell}(kr)$ defines the radial components of the wave [100].

The partial waves with increasing ℓ are assigned the letters s, p, d, f etc. In hadron-hadron interactions, the radius r can be approximated by p/(200 MeV/c) [100]. In order to generate higher-order partial waves beyond s, the momentum of the η meson should be in the order of 200 MeV/c. In the current experiment the two beam momenta were 2026 MeV/c and 2188 MeV/c which correspond to the 113.14 MeV/c and 250.57 MeV/c of the η momentum. We would expect p waves from the measurements.

Assuming that p and d waves can occur for the η meson production, its analyzing power is given by:

$$A_y = \frac{\Im(A_{Ps}A^*_{Pp})sin\theta_{\eta} + \Im(A_{Ss}A^*_{Sd})3cos\theta_{\eta}\sin\theta_{\eta}}{\frac{d\sigma}{d\Omega}}, \tag{8.2}$$

where $\Im(A_{Ps}A^*_{Pp})$ is the imaginary part of the interference term between the Ps and Pp waves, and $\Im(A_{Ss}A^*_{Sd})$ is the interference term between the Ss and Sd waves [101]. The denominator is a differential cross section $\frac{d\sigma}{d\Omega}$. The experiments COSY-11 and TOF [102] show that the differential cross section is constant up to Q = 41 MeV. For Q = 15 MeV assumption that the differential cross section is constant was used, and for the excess energy equal to 72 MeV the parametrization of the differential cross section is obtained from reference [103] as a quadratic function in $\cos\theta_{\eta}$. This result can be seen in Fig. 8.3.

In order to understand the partial wave contributions, the analyzing power of the η meson has to be fitted with the sum of the associated Legendre polynomials normalized to the differential cross section (see Eq. 8.2).

For the vector analyzing power the legendre polynomials will have the order of $m = 1$. The terms of the polynomial for this case read:

$$P^1_1(cos\theta_{\eta}) = -sin\theta_{\eta} \tag{8.3}$$

$$P^1_2(cos\theta_{\eta}) = -3cos\theta_{\eta}\sin\theta_{\eta} \tag{8.4}$$

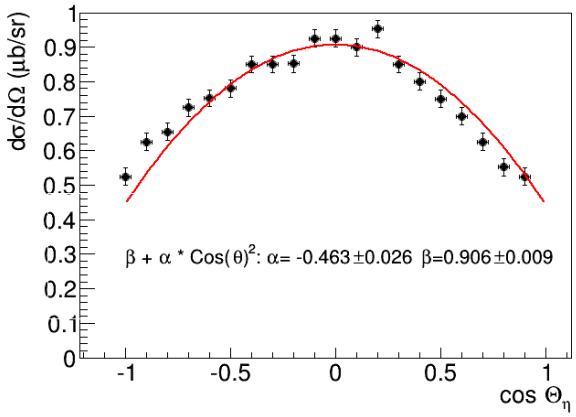

Figure 8.3: Distribution of the differential cross section as a function of $\cos\theta_\eta$ [103].

For $PsPp$ interference we expect $A_y\frac{d\sigma}{d\Omega}$ to be proportional to $\sin\theta_\eta$. For $SsSd$ interference we expect $A_y\frac{d\sigma}{d\Omega}$ proportional to $\sin 2\theta_\eta \approx cos\theta_\eta \sin\theta_\eta$.

Figure 8.4 shows result obtained in this thesis with the results of the fit with the formula

$$A_y\frac{d\sigma}{d\Omega} = C_1 \cdot sin\theta_\eta + C_2 \cdot cos\theta_\eta sin\theta_\eta \tag{8.5}$$

with C_1 and C_2 treated as free parameters of the fit. One can see in Fig. 8.4 and Fig. 8.5 that the associated Legendre polynomials of order $m = 1$ fully describe the existing data.

From the fits shown in Fig. 8.4 and Fig. 8.5 we deduce that $PsPp$ and $SsSd$ interference is negligible for Q = 15 MeV, since the contribution of the individual parts of the associated Legendre polynomials is zero within the error bars. Ss is surely different from zero, which excludes a contribution of Sd wave at this energy. Ps and Pp cannot be disentangled unambiguously, since the interference will be zero if one or both of the contributions are zero.

For the higher beam momentum 2188 MeV/c, $C_2 = -0.006 \pm 0.003$, which means a very small or maybe still negligible contribution from $SsSd$ so we may claim that even at such a large excess energy Sd is very small or negligible. On the other hand, the contribution of C_1 is equal to -0.104 ± 0.004, so $PsPp$ is large which means that both of these partial waves contribute at Q = 72 MeV (see Fig. 8.4).

For the systematic studies of the constants C_1 and C_2 the analyzing power of the η meson as a function of the $\cos\theta_\eta$ angular distribution was used. The

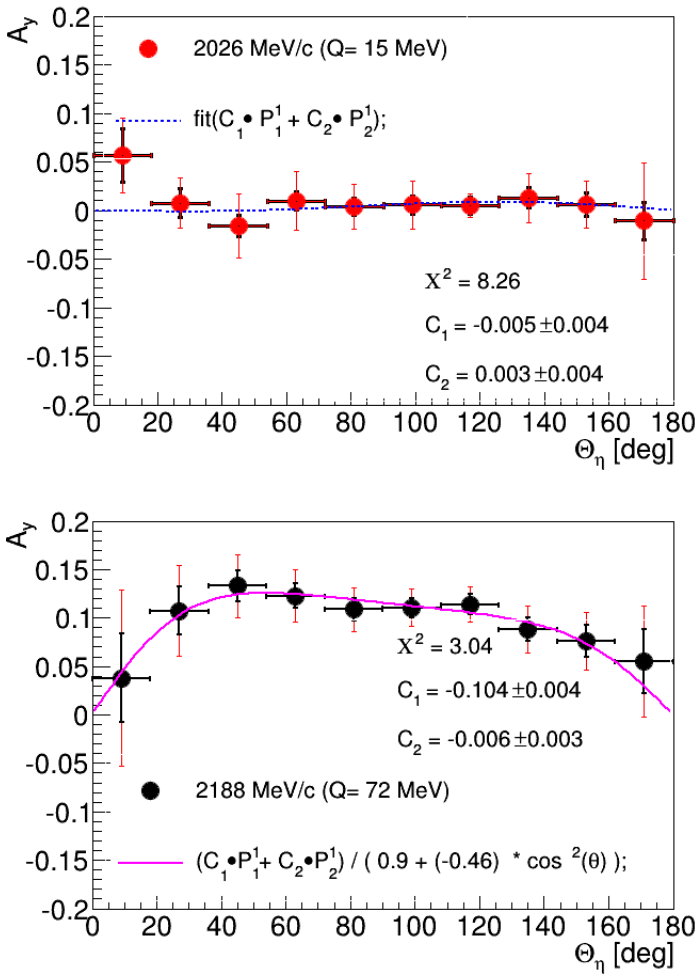

Figure 8.4: Analyzing power of the η meson as a function of θ_η. The fit of A_y with the sum of the two associated Legendre polynomials P_1^1 and P_2^1 is shown for the Q = 15 MeV (upper panel) and for Q = 72 MeV (lower panel).

final results are shown in Tab. 8.1, where coefficients C_1^{final} and C_2^{final} is average from calculations based on the θ_η and $\cos\theta_\eta$ distributions. Statistical uncertainty are calculated as:

$$C_{1,2}^{stat} = \frac{\sqrt{C_{1,2}^{stat}(\theta_\eta)^2 + C_{1,2}^{stat}(\cos\theta_\eta)^2}}{2}, \tag{8.6}$$

and the systematic uncertainty as:

$$C_{1,2}^{syst} = \frac{|C_{1,2}(\theta_\eta) - C_{1,2}(\cos\theta_\eta)|}{2}. \tag{8.7}$$

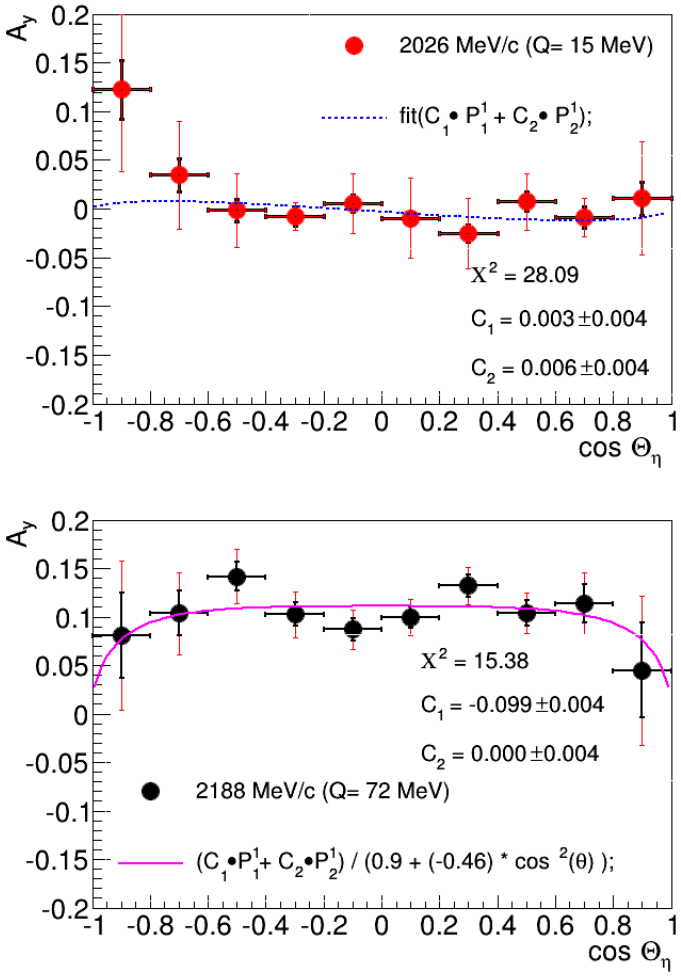

Figure 8.5: Analyzing power of the η meson as a function of $\cos\theta_\eta$. The fit of A_y with the sum of the two associated Legendre polynomials P_1^1 and P_2^1 is shown for Q = 15 MeV (upper panel) and Q = 72 MeV (lower panel).

p_{beam}	$C_1^{final} \pm stat \pm syst$	$C_2^{final} \pm stat \pm syst$
2026 MeV/c	0.004 ± 0.003± 0.001	0.004± 0.003± 0.002
2188 MeV/c	-0.102± 0.003± 0.003	-0.003± 0.003± 0.003

Table 8.1: Coefficients C_1^{final} and C_2^{final} determined for the momenta 2026 MeV/c and 2188 MeV/c for the associated Legandre polynomial fit to analyzing power of the η meson.

Chapter 9

Conclusions and outlook

During experiments conducted in 2010 at the WASA-at-COSY detector two reactions were measured: elastic proton scattering $\vec{p}p \rightarrow pp$ for measuring beam polarization and inelastic proton scattering $\vec{p}p \rightarrow pp\eta$ for calculating the analyzing power of the η meson. The measurement of the reaction $\vec{p}p \rightarrow pp\eta$ were performed for two decay channels of the η meson: $\eta \rightarrow \gamma\gamma$ and $\eta \rightarrow 3\pi^0$ where each π^0 eventually decayed into a photon pair. Since the magnetic field of the detector was switched off for the duration of the experiment, only the neutral channels of the η decay could be studied.

The vertex position was reconstructed with two independent methods. Since there was a shift of the vertex position from the nominal position, the polarization was calculated using the corrected value. The beam polarization was very stable over time but there was a considerable difference in beam polarization between the two spin modes. Therefore, the determination of the analyzing power for the $\vec{p}p \rightarrow pp\eta$ reaction was performed separately for each spin orientation.

Thanks to the large amount of collected η events, the statistical uncertainty of our result of the analyzing power for the η meson is much smaller than in the data of the previous COSY-11 experiments. This allowed the conclusion that none of the theoretical predictions for the production mechanism of the η meson agrees with the data. Therefore, new theories are required for further understanding of the η meson production.

The analyzing power is zero for the beam momentum 2026 MeV/c. This means that there is no interference between A_{Ss}, A_{Ps}, A_{Pp} and A_{Sd} amplitudes of the partial waves.

The associated Legendre polynomials of second order were fitted to the analyzing power. For the lower beam momentum 2026 MeV/c, there is a clear

evidence that there are no contributions of the Sd partial wave. However, Ps contribution is still not excluded. In contrast, for the beam momentum 2188 MeV/c there is enough excess energy available to produce not only s waves but also p waves, and indeed a strong interference between Ps and Pp partial waves was observed.

Acknowledgments

Here I would like to thank all the people who were with me during my PhD studies, since all of them have played a significant role for the development of my new personality.

First of all I wish to express my sincere thanks to my supervisor Prof. Dr. hab. Pawel Moskal. I really like to observe the way of his intelligent, diplomatic loyalty. I hope that I have learned from him not only about high energy physics, but also about the philosophic relation to life itself.

I take this opportunity to express gratitude to my junior supervisors Dr. Malgorzata Hodana and Dr. ing. Marcin Zieliński for their help and support.

I am grateful for the school of life that were my colleagues from Jülich Research Centre. Special thanks go to Volker Hejny and Frank Goldenbaum for their help and assistance.

I wish to express my sincere thanks to Prof. Kamys, head of PhD studies, for providing me with all the necessary documents for my family.

I want to thank Leonid Levchuk who introduced me to elementary particle physics.

I am specially grateful to my friend Magdalena Skurzok for answering all my 'general questions' and the great time that we have spent together. Thanks to Maryna Syrkova, Teresa Gucwa - Ryś, Farha Khan, Monika Pawlik, Wojciech Krzemień, Tomasz Bednarski, Szymon Niedźwiecki, Ewelina Kubicz, Oleksandr Rundel, Anna Wieczorek, Izabela Pytko, Tomasz Twaróg and to all others colleagues from Krakow UJ for the happy moments during these years.

Thanks very much for my friends Florian Bergmann, Kay Demmich and Florian Hauenstein for proof-reading the manuscript and great time during my stay in Jülich.

I also thank my parents Natalia Ozerianska and Oleksandr Ozeriansky for the support and attention during Skype sessions and beyond. For my uncle Vladimir on whom I can count in this life. Thanks to my sisters Aleksandra and Tatjana which make me happy all my life.

I am also grateful to my husband, Andreas Schätti, whose support was important to me. For the unceasing encouragement, support and attention. Big 'Thank You' for all the comments that greatly improved the manuscript. I ♡ You!

Appendix A

The eta meson

The Standard Model of particle physics describes the fundamental structure of matter and its interactions. Hadrons are described as color-neutral bound states of quarks, anti-quarks, and gluons. They consist of either three quarks or antiquarks with different color (baryons) or a quark and an anti-quark with opposite color (mesons). Since the quarks are fermions with half-integer spin, baryons are also fermions while mesons are classified as bosons. The three lightest quarks (up, down, and strange) exhibit approximate SU(3) flavor symmetry, which gives rise to nine possible quark-antiquark bound states, grouped into an octect and a singlet state.

The physical η meson is a combination of the η_8 (octet) and η_1 (singlet) states:

$$\eta_8 = \frac{1}{\sqrt{6}}(u\bar{u} + d\bar{b} - 2s\bar{s}) \tag{A.1}$$

$$\eta_1 = \frac{1}{\sqrt{3}}(u\bar{u} + d\bar{b} - s\bar{s}) \tag{A.2}$$

These states are related via the mixing angle θ:

$$\eta = \eta_8 \cos(\theta) - \eta_1 \sin(\theta) \tag{A.3}$$

where θ has been experimentally determined to be -15.5 $\pm$ 1.3 degrees. The mass of the η has been measured as 547.853 $\pm$ 0.024 MeV/c^2. Several attributes of the η make it a prime candidate for experimental investigation. The η has a relatively long lifetime of $(5.0 \pm 0.3) \cdot 10^{-19}$s and a correspondingly narrow width of 1.30 ± 0.07 keV. Additionally, most quantum numbers, including charge, spin, strangeness, and orbital angular momentum are zero. The η is an eigenstate of charge conjugation and parity with $J^{PC} = 0^{-+}$. Furthermore, all strong and electromagnetic decays of the η are suppressed in the first order.

Appendix B

Tables

Θ°_{cm}	$A_y\ test1$	$A_y\ test2$	$A_y test3$	$\Delta A_y test4$	$\frac{\Delta A_y}{\Delta\sigma_1}$	$\frac{\Delta A_y}{\Delta\sigma_2}$	$\frac{\Delta A_y}{\Delta\sigma_3}$	$\frac{\Delta A_y test4}{\Delta\sigma_4}$
$[0, 18]$	0.057 ± 0.029	0.058±0.027	0.082±0.029	0.011±0.028	0.025	0.052	0.656	6.067
$[18, 36]$	0.031± 0.015	0.01±0.015	0.007±0.016	-0.011±0.016	1.08	0.094	0.045	3.412
$[36, 54]$	-0.015± 0.012	-0.018±0.011	-0.014± 0.012	-0.022±0.013	0.061	0.128	0.112	0.866
$[54, 72]$	0.025± 0.010	0.01±0.009	0.013± 0.010	-0.021±0.011	3.670	0.0785	0.5	4.743
$[72, 90]$	0.001± 0.009	0.009±0.010	-0.017±0.01	-0.014±0.011	0.982	0.371	0.297	2.846
$[90, 108]$	0.013± 0.009	0.008±0.011	-0.014±0.010	-0.016±0.011	0.235	0.211	0.966	8.063
$[108, 126]$	0.005± 0.009	0.009±0.009	0.015±0.011	-0.003±0.011	0.628	0.314	0.668	1.264
$[126, 144]$	0.017± 0.010	0.015±0.011	0.017±0.013	-0.015±0.012	0.282	0.34	0.703	4.221
$[144, 162]$	0.016± 0.019	0.010±0.012	0.009±0.014	-0.012±0.014	0.282	0.067	0.243	1.401
$[162, 180]$	0.030± 0.020	-0.018±0.019	-0.043±0.023	-0.042±0.023	0.724	0.761	1.106	2.391

Table B.1: Results of the studies of systematic effects of the analyzing power as a function of θ_η for the the beam momentum $p_b = 2026$ MeV/c. For the test 1, the influence of the particle ID was checked, test 2 was done for checking the influence of the counting of the η mesons and test 3 was done for the influence of the polarization change of the final result. Test 4 show the systematic effect on analyzing power due to different η decay reactions ($\eta \to 2g$ and $\eta \to 3\pi^0$). Column 6, 7, 8 and 9 show the coefficients from the Barlow method [99] from corresponding tests(1, 2, 3, 4).

Θ°_{cm}	$A_y\ test1$	$A_y\ test2$	$A_y\ test3$	$\Delta A_y test4$	$\frac{\Delta A_y}{\Delta\sigma_1}$	$\frac{\Delta A_y}{\Delta\sigma_2}$	$\frac{\Delta A_y}{\Delta\sigma_3}$	$\frac{\Delta A_y test4}{\Delta\sigma_4}$
$[0, 18]$	0.081± 0.046	0.068±0.044	0.084±0.045	0.037±0.013	0.305	0.471	0.714	0.021
$[18, 36]$	0.101± 0.024	0.095±0.023	0.092± 0.024	0.022±0.0026	0.176	0.360	0.441	3.554
$[36, 54]$	0.12± 0.015	0.137±0.015	0.128± 0.015	0.017±0.007	0.612	0.188	0.235	8.743
$[54, 72]$	0.105± 0.012	0.101±0.013	0.104±0.012	0.014±0.018	1.07	1.196	1.073	8.755
$[72, 90]$	0.078± 0.011	0.084±0.012	0.076±0.011	0.011±0.014	1.9	1.4	2.057	11.201
$[90, 108]$	0.093± 0.010	0.103±0.011	0.085±0.011	0.009±0.014	1.202	0.470	1.681	10.308
$[108, 126]$	0.119± 0.010	0.125±0.011	0.117±0.012	0.008±0.009	0.336	0.739	0.192	24.318
$[126, 144]$	0.075± 0.011	0.103±0.013	0.076±0.012	0.095±0.005	0.798	0.847	0.707	0.6416
$[144, 162]$	0.096± 0.015	0.113±0.019	0.098±0.015	0.013±0.024	0.882	1.451	0.97	3.718
$[162, 180]$	0.098± 0.031	0.041±0.049	0.092±0.031	0.024±0.024	0.949	0.236	0.817	1.368

Table B.2: Results of the studies of systematic effects of the analyzing power as a function of θ_η for the the beam momentum $p_b = 2188$ MeV/c. For the test 1, the influence of the particle ID was checked, test 2 was done for checking the influence of the counting of the η mesons and test 3 was done for checking the influence of the polarization change on the final result. Test 4 show the systematic effect on analyzing power due to different η decay reactions ($\eta \to 2g$ and $\eta \to 3\pi^0$). Column 6, 7, 8 and 9 show the coefficients from the Barlow method [99] from corresponding tests(1, 2, 3, 4).

Θ°_{cm}	$A_y\ test1$	$A_y\ test2$	$A_y test3$	$\Delta A_y test4$	$\frac{\Delta A_y}{\Delta\sigma_1}$	$\frac{\Delta A_y}{\Delta\sigma_2}$	$\frac{\Delta A_y}{\Delta\sigma_3}$	$\frac{\Delta A_y test4}{\Delta\sigma_4}$
$[-1., -0.8]$	-0.002 ± 0.010	-0.017±0.0103	0.073±0.029	0.054±0.032	0.004	0.052	0.656	1.195
$[-0.8, -0.6]$	0.015± 0.014	-0.004±0.013	0.025±0.016	-0.004±0.017	2.073	0.094	0.045	0.583
$[-0.6, -0.4]$	0.075± 0.012	0.027±0.011	0.026± 0.011	-0.026±0.013	0.0160	0.128	0.112	-0.139
$[-0.4, -0.2]$	0.005± 0.011	-0.048±0.010	0.0061± 0.097	-0.035±0.012	1.897	0.0785	0.5	1.271
$[-0.2, 0.]$	0.021± 0.010	0.013±0.009	0.009±0.089	-0.004±0.011	3.760	0.371	0.297	0.713
$[0., 0.2]$	-0.036± 0.008	-0.049±0.009	-0.011±0.086	-0.032±0.011	0.109	0.211	0.966	2.044
$[0.2, 0.4]$	-0.011± 0.008	-0.021±0.009	-0.016±0.087	-0.027±0.011	8.731	0.314	0.668	0.409
$[0.4, 0.6]$	0.018± 0.009	0.031±0.009	0.014±0.099	-0.026±0.012	2.52	0.34	0.703	1.146
$[0.6, 0.8]$	0.001± 0.009	0.006±0.010	-0.003±0.011	-0.031±0.013	2.294	0.067	0.243	0.618
$[0.8, 1.]$	0.020± 0.009	0.024±0.009	0.039±0.016	-0.018±0.022	0.68	0.761	1.106	0.438

Table B.3: Results of the studies of systematic effects of the analyzing power as a function of $cos\theta_\eta$ for the the beam momentum $p_b = 2026$ MeV/. For the test 1, the influence of the particle ID was checked, test 2 was done for checking the influence of the counting of the η mesons and test 3 was done for checking the influence of the polarization change on the final result. Test 4 show the systematic effect on analyzing power due to different η decay reactions ($\eta \to 2g$ and $\eta \to 3\pi^0$). Column 6, 7, 8 and 9 show the coefficients from the Barlow method [99] from corresponding tests(1, 2, 3, 4).

Θ°_{cm}	$A_y\ test1$	$A_y\ test2$	$A_y\ test3$	$\Delta A_y test4$	$\frac{\Delta A_y}{\Delta\sigma_1}$	$\frac{\Delta A_y}{\Delta\sigma_2}$	$\frac{\Delta A_y}{\Delta\sigma_3}$	$\frac{\Delta A_y test4}{\Delta\sigma_4}$
$[-1., -0.8]$	0.045± 0.017	0.046±0.020	0.029±0.012	0.033±0.029	0.305	0.471	0.714	0.997
$[-0.8, -0.6]$	0.088± 0.019	0.100±0.023	0.054± 0.014	0.019±0.011	0.176	0.360	0.441	3.840
$[-0.6, -0.4]$	0.075± 0.015	0.080±0.018	0.051± 0.011	0.013±0.006	0.612	0.188	0.235	5.335
$[-0.4, -0.2]$	0.054± 0.013	0.084±0.015	0.037±0.098	0.011±0.021	1.07	1.196	1.073	6.469
$[-0.2, 0.]$	0.103± 0.011	0.107±0.014	0.077±0.091	0.009±0.025	1.9	1.4	2.057	7.272
$[0., 0.2]$	0.102± 0.011	0.105±0.013	0.072±0.085	0.008±0.009	1.202	0.470	1.681	8.447
$[0.2, 0.4]$	0.089± 0.011	0.064±0.012	0.054±0.087	0.008±0.022	0.336	0.739	0.192	10.757
$[0.4, 0.6]$	0.093± 0.011	0.073±0.012	0.063±0.083	0.008±0.016	0.798	0.847	0.707	9.392
$[0.6, 0.8]$	0.085± 0.014	0.067±0.015	0.058±0.010	0.012±0.031	0.882	1.451	0.97	8.808
$[0.8, 1.]$	0.083± 0.016	0.087±0.017	0.055±0.010	0.028±0.06	0.949	0.236	0.817	7.136

Table B.4: Results of the studies of systematic effects of the analyzing power as a function of $cos\theta_\eta$ for the the beam momentum $p_b = 2188$ MeV/c. For the test 1, the influence of the particle ID was checked, test 2 was done for checking the influence of the counting of the η mesons and test 3 was done for checking the influence of the polarization change on the final result. Test 4 show the systematic effect on analyzing power due to different η decay reactions ($\eta \to 2g$ and $\eta \to 3\pi^0$). Column 6, 7, 8 and 9 show the coefficients from the Barlow method [99] from corresponding tests(1, 2, 3, 4).

Bibliography

[1] A. Pevsner et al. *Phys. Rev. Lett.*, **7**:421, 1961.

[2] E. Chiavassa et al. *Phys. Lett.*, **B322**:270, 1994.

[3] H. Calén et al. *Phys. Lett.*, **B366**:39, 1996.

[4] H. Calén et al. *Phys. Rev. Lett.*, **79**:2642, 1997.

[5] F. Hibou et al. *Phys. Lett.*, **B438**:41, 1998.

[6] J. Smyrski et al. *Phys. Lett.*, **B474**:182, 2000.

[7] A.M. Bergdolt et al. *Phys. Rev.*, **D48**:2969, 1993.

[8] M. Abdel-Bary et al. *Eur. Phys. J.*, **A16**:127, 2003.

[9] P. Moskal et al. *Phys. Rev.*, **C69**:025203, 2004.

[10] P. Moskal et al. *Eur. Phys. J.*, **A43**:131, 2010.

[11] H. Petrén et al. *Phys. Rev.*, **C82**:055206, 2010.

[12] H. Calén et al. *Phys. Rev. Lett.*, **79**:2642, 1997.

[13] H. Calén et al. *Phys. Rev.*, **C 58**:2667, 1998.

[14] P. Moskal et al. *Phys. Rev.*, **C79**:015208, 2009.

[15] C. Wilkin. *Acta Phys. Polon.*, **B41**:2191, 2010.

[16] K. Nakayama et al. *Phys. Rev.*, **C65**:045210, 2002.

[17] G. Fäldt and C. Wilkin. *Phys. Scripta*, **64**:427, 2001.

[18] J.F. Germond et al. *Nucl. Phys.*, **A518**:308, 1990.

[19] J.M. Laget et al. *Phys. Lett.*, **B257**:254, 1991.

[20] A. Moalem et al. *Nucl. Phys.*, **A600**:445, 1996.

[21] T. Vetter et al. *Phys. Lett.*, **B263**:153, 1991.

[22] B.L. Alvaredo et al. *Phys. Lett.*, **B324**:125, 1994.

[23] M. Batinic et al. *Phys. Scripta*, **56**:321, 1997.

[24] P. Moskal. *Hadronic interaction of eta and eta-prime mesons with protons, arXiv:hep-ph/0408162*. Jagiellonian University Press, 2004.

[25] R. Czyżykiewicz et al. *Phys. Rev. Lett*, **98**:122003, 2007.

[26] A.M. Green and S. Wycech. *Nucl.Phys.*, **A663**:529–532, 2000.

[27] P. Moskal et al. *Phys. Lett.*, **B482**:356, 2000.

[28] P. Moskal et al. *Prog. Part. Nucl. Phys.*, **49**:1, 2002.

[29] P. Moskal and J. Smyrski. *Acta Phys. Pol.*, **B41**:2281, 2010.

[30] M. Skurzok, P. Moskal, W. Krzemien. *Prog. Part. Nucl. Phys.*, **67**:445, 2012.

[31] P. Adlarson et al. *Phys. Rev.*, **C87**:035204, 2013.

[32] A. Budzanowski et al. *Phys. Rev.*, **C79**:012201, 2009.

[33] M. Nanova et al. *Phys. Lett.*, **B727**:417–423, 2013.

[34] K. Itahashi. *Prog. Theor. Phys.*, **128**:601, 2012.

[35] S.V. Afanasiev. *Phys. Part. Nucl. Lett.*, **8**:1073, 2011.

[36] H. Fujioka. *Acta Phys. Polon.*, **B41**:2261, 2010.

[37] V.A. Baskov et al. *PoS Baldin-ISHEPP-XXI*, page 102, 2012.

[38] B. Krusche et al. *J. Phys. Conf. Ser.*, **349**:012003, 2012.

[39] C. Wilkin. *Phys. Lett.*, **B654**:92, 2007.

[40] S.D. Bass, A.W. Thomas. *Phys. Lett.*, **B634**:368, 2006.

[41] H. Nagahiro et al. *Phys. Rev.*, **C87**:045201, 2013.

[42] S.D. Bass. *Acta Phys. Pol.*, **B45**:2455, 2014.

[43] S. Hirenzaki et al. *Acta Phys. Polon.*, **B41**:2211, 2010.

[44] E. Friedman, A. Gal, J. Mares. *Phys. Lett.*, **B725**:334, 2013.

[45] S. Wycech and W. Krzemien. *Acta Phys. Pol.*, **B45**(3):745, 2014.

[46] N.G. Kelkar et al. *Rept. Prog. Phys.*, **76**:066301, 2013.

[47] S.D. Bass and A. W. Thomas. *Acta Phys. Polon.*, **B41**:2239, 2010.

[48] Y.N. Uzikov. *Nucl. Phys.*, **A801**:114, 2008.

[49] J.A. Niskanen. *Eur. Phys. J.*, **36**:295–301, 2008.

[50] A. Sibirtsev et al. *Phys. Rev.*, **C70**:047001, 2004.

[51] Q. Haider, L. C. Liu. *Int. Mod. Phys*, **E24**:63, Sept 2015.

[52] M. Hodana et al. *Acta Phys. Polon.*, **B45**:697, 2014.

[53] P. Klaja et al. *Phys. Lett.*, **B684**:11, 2010.

[54] P. Moskal and M. Hodana. *J. Phys. Conf. Ser*, **296**:012080, 2011.

[55] R. Czyżykiewicz. PhD thesis, Jagiellonian University of Cracow, 2006.

[56] E. Pickup et al. *Phys. Rev. Lett.*, **8**:329, 1962.

[57] G. Alexander et al. *Phys. Rev.*, **154**:1284, 1984.

[58] A.P. Colleraine et al. *Phys. Rev.*, **161**:1387, 1967.

[59] L. Bodini et al. *Nuovo Cimiento*, **A 58**:475, 1968.

[60] C. Caso et al. *Nuovo Cimiento*, **A 55**:66, 1968.

[61] S.P. Almeida et al. *Phys. Rev.*, **174**:1638, 1968.

[62] E. Colton et al. *Phys. Rev.*, **D1**:1979, 1970.

[63] P. Moskal et al. *Phys. Rev.*, **C 69**:025203, 2004.

[64] H. Calén et al. *Phys. Rev.*, **C 58**:2667, 1998.

[65] M. Abdel-Bary et al. *Eur. Phys. J.*, **A16**:127, 2003.

[66] H. Petrén et al. *Phys. Rev.*, **C 82**:055206, 2010.

[67] K. Nakayama et al. *Phys. Rev.*, **C68**:045201, 2003.

[68] K. Nakayama. In *Proc. of the 11th Intern. Conf. on Meson-Nucleon Physics and the Structure of the Nucleon*, page 154, 2007.

[69] A. Deloff. *Phys. Rev.*, **C69**:035206, 2004.

[70] H.O. Meyer et al. *Phys. ReV.*, **C 63**:064002, 2001.

[71] G.G. Ohlsen and P.W. Keaton Jr. *Nucl. Instr. Meth.*, **7**:41–59, 15 May 1973.

[72] F. Balestra et al. *Phys. Rev.*, **C69**:064003, 2004.

[73] R. Maier. *Nucl. Instr. Meth.*, **A390**:1, 1997.

[74] D. Prasuhn et al. *Nucl. Instr. Meth.*, **A441**:167–174, 2000.

[75] WASA-at-COSY Collaboration: H.-H. Adam et al. *arXiv:nucl-ex/0411038*, 2004.

[76] A. Pricking. PhD thesis, 2010.

[77] M. Janusz et. al. Ikp annual report. Technical report, Forschungszentrum Jülich, Germany, 2006.

[78] M. Janusz, M. Jacewicz, L. Yurev. Ikp annual report. Technical report, Forschungszentrum Jülich, Germany, 2008.

[79] J. Dyring. PhD thesis, Uppsala University, 1997.

[80] H. Calén et. al. Ikp annual report. Technical report, Forschungszentrum Jülich, Germany, 2007.

[81] D. Coderre. PhD thesis, Ruhr Universität Bochum, 2012.

[82] E. Pérez del Rio. PhD thesis, Tübingen University, 2014.

[83] M. Zieliński. PhD thesis, Jagiellonian University of Cracow, 2013.

[84] B.R. Jany. PhD thesis, Jagiellonian University of Cracow, 2006.

[85] R. Gebel. *Private communication*, 2014.

[86] M. Altmeier et al. *Phys. Rev. Lett.*, **85**:1819, 2000.

[87] S. Lee. *Spin Dynamics and Snakes in Synchrotrons*. World Scientific, 1997.

[88] D. Barber et al. In *Sixth European Particle Accelerator Conference (EPAC'98)*, pages 1362–1364, 1998.

[89] H. Stockhorst. Ikp annual report. Technical report, Forschungszentrum Jülich, Germany, 2004.

[90] W. MacKay. *USPAS, Lecture On Spin Dynamics in Accelerators*, 27 June 2008.

[91] I. Froehlich et al. *ACAT 2007, Amsterdam*, pages 31–33, 2007.

[92] R. Brun and F. Rademakers. *Nucl. Instr. Meth.*, **A389**:81, 1997.

[93] R. Brun, F. Carminati and S. Giani. CERN Program Library Long Writeup W5013. 1993.

[94] V. Hejny, M. Hartmann, and A. Mussgiller. Rootsorter: A new analysis framework for anke. *IKP / COSY Annual Report 2002*, **Jul-4052**, 2003.

[95] M. Hodana, P. Moskal, I. Ozerianska. *J. Phys. Conf. Ser*, **6**:1041, 2013.

[96] L. Demirors. PhD thesis, Hamburg University, 2005.

[97] D. Prashun. private communication, 2013.

[98] A. Deloff. Madison convention. In W. Haeberli H.H. Barschall, editor, *Proc. 3rd Int. Symp. on Polarization Phenomena in Nucl. Reactions*, page xxv, Madison|, 1971. University of Wisconsin Press.

[99] R. Barlow. *Systematic errors: Facts and fiction, arXiv:0207026*, 2002.

[100] T. Mayer-Kuckuk. *Kernphysik: Eine Einführung*. Teubner, Stuttgart, 3 edition, 1979.

[101] Saha et al. *Phys. Rev. Letter*, **51, 9**:759, 1983.

[102] M. Abdel-Bary et al. *Eur. Phys. J.*, **A16**:127–137, 2003.

[103] H. Petrén et al. *Phys. Rev.*, **C 82**:055206, 2010.